PHD

Analysis of IDG discontinuities

Pourabadeh, J.

Award date:
1998

Awarding institution:
University of Bath

ANALYSIS OF IDG DISCONTINUITIES

Submitted by J. Pourabadeh

for the Degree of PhD

of the University of Bath

September 1998

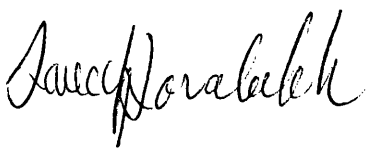

ProQuest LLC
789 East Eisenhower Parkway
P.O. Box 1346
Ann Arbor, MI 48106-1346

To my wife

Tahmineh

and our daughters

Tanya and *Shady*

Contents

Summary

The object of the present thesis is the analysis of Inset Dielectric Guide (IDG) circuit discontinuities which had not been examined prior to this work. IDG is a rectangular slot filled with dielectric material flush mounted in a ground plane.

To fulfill the analysis, the Finite Difference Time Domain (FDTD) method is selected from among many methods. This method is implemented in a rectangular waveguide to test the analysis and to develop the method of excitation. Absorbing Boundary Conditions (ABCs) in order to make the numerical computation domain finite have also been examined. From several ABCs, the 1st order Mur's was chosen as an effective and simple one for implementation, in addition the Perfectly Matched Layer (PML) was chosen as a newer method of ABC. By the excitation procedure the necessary field components for initiating the FDTD method are supplied through the inverse Fourier transform as a function of distance. To have a desirable frequency bandwidth in the output of the FDTD analysis, the input frequency bandwidth of the inverse Fourier transform is multiplied by a factor which is the ratio of the phase to group velocity of the guide.

As the fundamental stage in the IDG discontinuities, the discontinuity caused by a metal obstacle normal to the guide is investigated by the FDTD method. The dominant mode of the IDG (HE_{01}) is approximated by the TE_{odd} mode of the dielectric slab waveguide. The same method of excitation as in the rectangular waveguide is used in this stage. 1st order Mur's ABC is selected because the PML ABC needs a lot of computer memory and its implementation is quite complicated. During the analysis the height of the obstacle and position of the monitor point are changed. Reflection and transmission coefficients of the guide are computed and the results are compared with measurements.

Finally, suggestions for analysing other types of IDG discontinuities are presented.

Acknowledgements

I would like to offer my appreciation to my supervisors Dr. S.R. Pennock and Dr. P.R. Shepherd for their helpful guidance and supervision.

I also thank my family for their cooperation during my studies while they are very far away from our home country.

Abbreviations

ABC	Absorbing Boundary Condition
BEM	Boundary Element Method
CMT	Conformal Mapping Technique
CPW	Coplanar Waveguide
DBC	Dispresive Boundary Condition
EM	Electro Magnetic
FDM	Finite Difference Method
FDTD	Finite Difference Time Domain Method
FEM	Finite Element Method
FT	Fourier Transform
GSMM	Generalized Scattering Matrix Method
IEM	Integral Equation Method
IDG	Inset Dielectric Guide
IP	Incident Pulse
MICs	Microwave Integrated Circuits
MMICs	Monolithic Microwave Integrated Circuits
MoM	Method of Moments

MMM	Mode Matching Method
PML	Perfectly Matched Layer
RP	Reflected Pulse
RC	Reflection Coefficient
TC	Transmission Coefficient
SDM	Spectral Domain Method
TE	Transverse Electric
TM	Transverse Magnetic
TEM	Transverse Electric and Magnetic
TLM	Transmission Line Matrix Method
TRT	Transverse Resonance Technique
TLM	Transmission Line Matrix method

List of Symbols

B	Magnetic Flux Density
E	Electric Field Intensity
f	Frequency
f_c	Cut-off Frequency
H	Magnetic Field Intensity
k_s	Stability Factor
mnt	Maximum Number of Time Steps
nl	Number of Layer
tnp	Total Number of Points
v_g	Group Velocity
v_g	Phase Velocity
Z_o	Characteristic Impedance
Z_w	Wave Impedance
β	Phase Constant
δ	Space Increment
Δt	Time Increment
ϵ_0	Free Space Permittivity

ϵ_r	Relative Permittivity
η	Intrinsic Impedance
λ	Wavelength
λ_c	Cut-off Wavelength
μ_0	Free Space Permeability
μ_r	Relative Permeability
σ	Electric Conductivity
σ^*	Magnetic Conductivity
ω	Angular Frequency

Chapter 1

Introduction

1.1 Outline

In this chapter microwave engineering frequencies and applications are introduced. Then some types of dielectric waveguide and Inset Dielectric Guide (IDG) are described. Also discontinuities in transmission lines and their importance are mentioned. Finally the purpose of the present thesis, which is analysis of the IDG discontinuities, and the structure of the thesis will be presented.

1.2 Microwave Engineering Frequencies and Applications

The description microwave engineering means generally the engineering and design of information-handling systems in the frequency range from 1 to 100 GHz corresponding to free space wavelengths from 30 cm to 3 mm [1, page 3]. However it may be considered to cover applications of electrical technology where the char-

acteristic wavelength is smaller than the dimensions of the system or circuit and yet where it is not so small that only ray optical techniques need be considered [2, page 2] and [3, page 17].

At microwave frequencies, conventional low-frequency circuit analysis based on Kirchhoff's laws no longer suffices for an adequate description of the electrical phenomena taking place. Therefore, it is necessary to carry out the analysis of the problems in terms of a description of the electric and magnetic fields based on Maxwell's equations, and lumped circuit elements are often replaced by transmission line components.

Microwave frequencies and techniques have been used for about a century and their applications are becoming more and more widely used. Most of these are mentioned below:

Communications. The microwave communication channel has a very large bandwidth and will accommodate thousands of telephone conversations or dozens of television channels at once. Microwave frequencies have to be used for satellite communications and communication with satellites, because the ionosphere is opaque to lower frequencies.

Broadcasting. A number of countries use microwave frequencies for local television stations or for satellite television broadcasting. The domestic consumer has a microwave receiver on the roof as part of an aerial system and a radio frequency signal is transmitted along the aerial cable to the television set.

Radar. This is the traditional use of microwaves. The name is derived from the initial letters of RAdio Detection And Ranging. As a simple description, a radar sends pulses and by receiving the reflection it is able to detect the location and distance of hidden objects [1] and [2].

Other applications are: microwave heating, microwave power transmision, stable

atomic clocks, industrial controls for flow or velocity measurement, motion detection, police speed radar, microwave radiometry and medical hypothermia or localized heating of tumours.

In all applications, for sending electromagnetic energy from a source to the consumer, various types of transmission lines are used.

1.3 Dielectric Waveguides and IDG

In recent years research has been done towards the use of microwave and millimetre frequencies for the transmission of information. As conventional metal waveguide become quite lossy and more difficult to fabricate as the wavelength becomes shorter, alternative dielectric waveguides have been proposed.

Dielectric waveguide, originally offering promise for a low loss transmission medium, has turned out to be disappointing with regard to integration of active devices, fabrication and tolerance to discontinuities. On the other hand it seems to offer the realisation of integrated leaky-wave antennas. Its third problem is the radiation loss at curved sections, junctions and discontinuities. This problem may be reduced by using materials with high permittivity. However, use of such materials is often prohibited due to operating frequency, size, and so on. [4].

Image Line. Figure 1.1a shows the geometry of this guide which consists of a dielectric slab backed to a conducting ground plane. Another problem of this guide is the conductor loss of the ground plane. To reduce this loss *Insulated Image Line* and *Inverted Strip Dielectric Waveguide* have been proposed (Figs. 1.1b and 1.1c). In these two guides if $\epsilon_{r1} > \epsilon_{r2}$ the major portion of the energy propagates in the upper layer (guiding layer) and therefore results in low conductor loss. In this case the ground plane has the role of heat sink and is convenient for dc biasing.

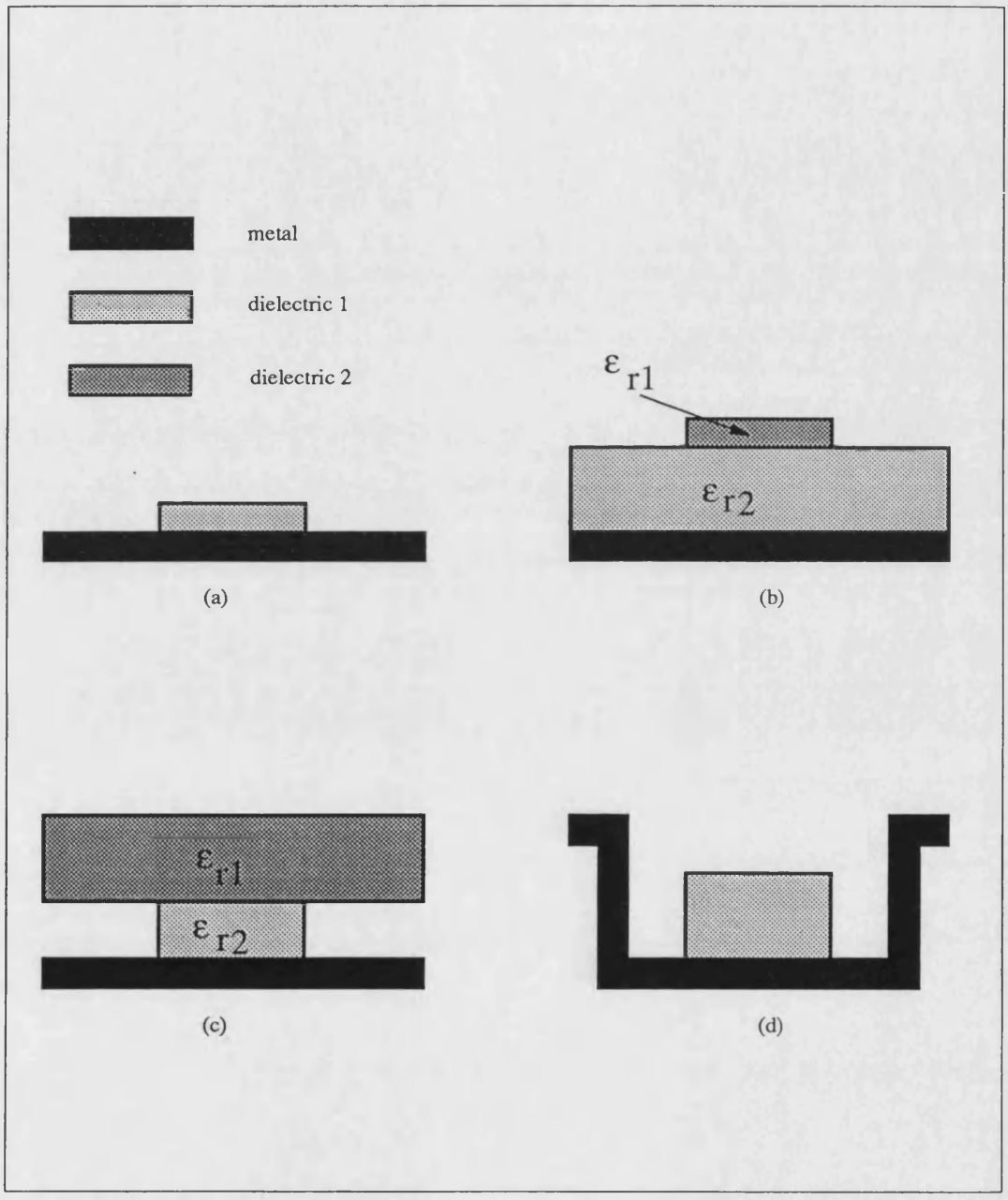

Figure 1.1: Dielectric waveguides a) image line b)insulated image line c)inverted strip dielectric waveguide d)trapped image line.

Inverted Strip Dielectric Waveguide. (Fig. 1.1c) This guide has been studied as a possible structure for reducing attenuation. This guide was proposed by T.Itoh [5]. He states that this guide is convenient for mounting solid state devices (because of the ground plane), has low loss, and is easy to fabricate. The major portion of the energy launched into this guide travels in the guiding layer (upper layer with ϵ_{r1})

Trapped Image Lines. This guide was proposed by T.Itoh and B.Adelseck [4]. A cross section of this guide is shown in Figure 1.1d. This structure is a dielectric slab deposited in a metal trough. In the image line electromagnetic energy escapes from the guiding structure at bends. In this guide, such leakage will be reflected back by the metallic walls if the depth of the trough is reasonably large.

Inset Dielectric Guide (IDG). This is simply a rectangular slot filled with dielectric material flush mounted in a ground plane (Fig 1.2a). It can be made by making a precision slot in a metal ground and then fill the groove with dielectric, or can be realized in a plastic mould that can be subsequently spray-metallized. Low melting point dielectric can be poured in the slot in liquid form, which is sufficient for many applications. High quality dielectric slab can be cut to a prescribed rectangular shape. Contacting with the metal wall is not as critical as for image line[6].

IDG is an evolution of a series of dielectric waveguides that start with image lines. Although image line is a low loss transmission medium, it has disadvantages like difficulties in manufacturing, and radiation loss from bends, practical components and discontinuities. For better confinement the fields in the guiding structure, trapped image line was proposed but manufacturing is more difficult especially for small dimensions. To overcome such manufacturing difficulties IDG was proposed. Therefore the three advantages characterize use of the IDG are: simpler manufacture, low radiation loss especially from bends, and easier connection to active devices.

Although IDG has some advantages, it may not be a competitor of some conventional guides such as microstrip and strip line. The disadvantages are mainly because of its bulky nature, difficulty in achieving (active) integrated circuitry, and inconvenience to fabricate comparing to microstrip and stripline.

During the last ten years, IDG has been investigated at the university of Bath. First of all, the rigorous analysis of this guide has been done by Hedges [7] by transverse resonance diffraction method. This method is an integral equation formulation that operates in the space domain and takes into account the singular boundary conditions to obtain a highly convergent computation procedure.

Ma [8] has analysed the IDG for applications to microwave and millimetric leaky wave antennas.

Sewell [9] has investigated the effects of radiation from the IDG, while Sewell and Rozzi [10] have developed the theory to determine the rigorous hybrid modal spectrum of open nonseparable structures such as the IDG. To validate this mode spectrum they have analysed the transition between a rectangular waveguide and the IDG by this method.

Boscovic [11] has analysed coupled IDG structures and applied the theory to practical coupler design. The problem has formulated through the transverse resonance diffraction approach using integral impedance or admittance operators, according to the polarization used.

1.4 Discontinuities in Transmission Lines

A discontinuity, which is a sudden change in dimension of the line, will appear in any practical line because of the connection of the line to the other parts like stubs, resonators, biasing networks, impedance transformers, directional couplers

and so on.

When the dimensions of the discontinuities are much smaller than the wavelength (typically one eighth of a wavelength) they can approximated by lumped element equivalent circuits [12, page 107]. A more complete characterization involves determination of the frequency dependent scattering matrix coefficients associated with the discontinuity.

Discontinuities appear in conventional microwave circuits but in MICs (Microwave Integrated Circuits), accurate characterization of discontinuities is much more important, because MIC circuits do not lend themselves to easy adjustments for tuning after the fabrication of the circuits is completed.

Changing conductor shapes is inherent in the discontinuity and causes a change in the electric and magnetic fields. Consequently there is a change in the capacitance and inductance near the discontinuity. The analysis of a discontinuity can involve the evaluation of these capacitance and inductance values. Although these variations are very small (often less than 0.1 pF and less than 0.1 nH), the reactances of these become particularly significant at microwave and millimetre wave frequencies [3, page 127].

Analysis of discontinuities can either be based on quasi-static considerations or carried out more rigorously by full wave analysis. In the quasi-static analysis, equivalent circuits for discontinuities may be derived from calculations of static capacitances and low frequency inductances associated with the discontinuities [12, page 108]. Radiation from various discontinuities gives rise to equivalent resistive elements [3, page 129]. In some cases techniques have been developed which compensate, at least over a particular range of frequencies, the existing discontinuity effects [3, page 129].

Up to now discontinuity investigations have been concerned with conventional lines mostly in quasi-static consideration and especially for microstrip lines. The

present thesis intends to investigate IDG discontinuities by a full wave analysis that have not yet been investigated. To fulfil this task, a discontinuity caused by a metal obstacle normal to the guide (Fig. 1.2) will be considered. This case is a fundamental stage in the analysis of IDG discontinuities because when this stage is achieved all problems such as finding the appropriate method for analysis and absorbing boundary condition and their implementations, approximation of the dominant mode of the guide, and excitation will be solved. By tiny changes in this stage, which are described in Conclusion (Chapter 7), other discontinuities of such guides can be analysed.

Another motivation for doing the present thesis is that the author has a particular interest in microwave and millimetric waveguide numerical computations.

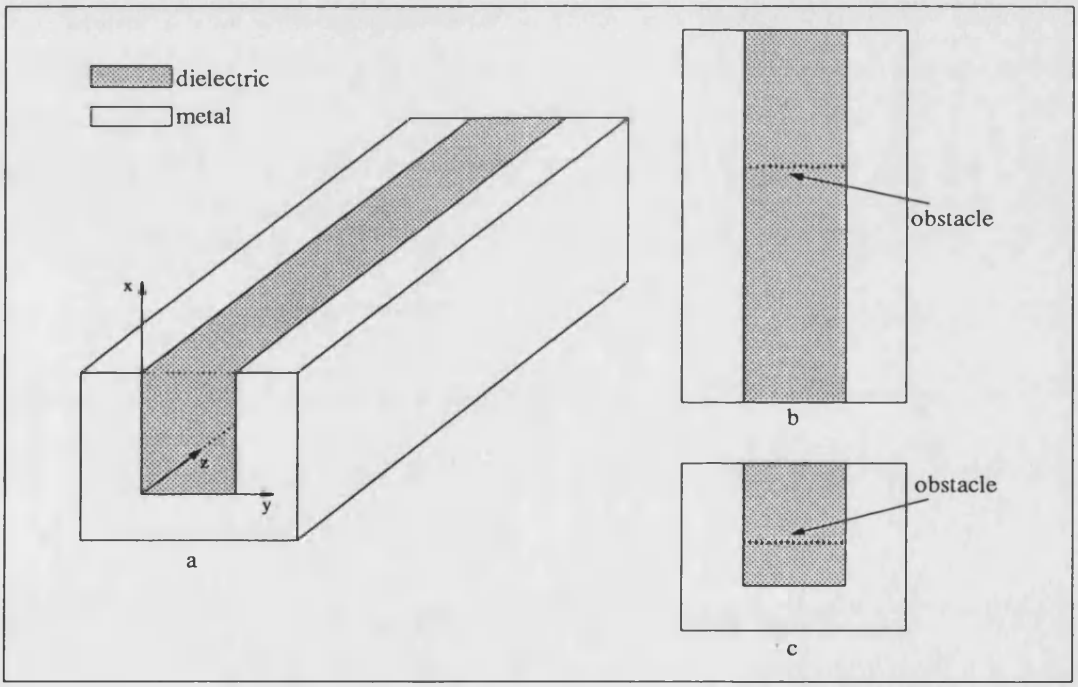

Figure 1.2: a)Inset dielectric guide (IDG) and position of the metal obstacle which is normal to the guide b)top view c)front view.

1.5 Structure of the Present Thesis

In the previous sections the usefulness of the IDG and the importance of the analysis of discontinuities in the guide have been outlined. Hence in this thesis attention is given to the analysis of IDG discontinuities. To fulfill this task, various types of discontinuities must first be recognised and appropriate methods of analysis determined. These two steps are achieved in Chapter 2 and from a number of methods, the FDTD method is selected.

For analysis of a discontinuity which causes reflection in the guide, a sine wave modulated by a Gaussian pulse is transmitted to the guide and when received by the discontinuity some part of it is reflected. The aim of the analysis is to find the reflection coefficient. In this approach this is defined from the ratio of the Fourier transforms of the reflected and incident time domain pulses. At a particular point of the line the FDTD method gives incident and reflected pulses in time and by taking Fourier transform, incident and reflected pulses in the frequency domain are obtained.

To prepare the FDTD analysis, the fundamental approach of the method, which is a discretisation of two Maxwell's curl equations in time and space together with determination of time and space step sizes, must be considered. Chapter 3 examines this case.

Because the IDG and most of the other guides are unbounded, to limit the computation domain nonphysical boundaries called Absorbing Boundary Condition (ABC) are needed for this limitation. 1st order Mur's and Perfectly Matched Layer (PML) ABCs are examined and Chapter 4 deals with their practical implementation.

To test the FDTD analysis at the IDG, to develop the excitation method, and to select the appropriate ABC, the FDTD method is implemented in a rectangular

waveguide for its dominant mode and Chapter 5 is concerning with these cases.

To analyse IDG discontinuities, the fundamental case which involves a metal obstacle is investigated in Chapter 6. The dominant mode in the IDG is HE_{10} which is approximated by the TE_{odd} mode of the dielectric slab waveguide. Based on the results as presented in Chapter 5, 1st order Mur's ABC is selected for analysis of the IDG discontinuities.

In Chapter 7 conclusions and suggestions for future work are presented.

Chapter 2

Discontinuities in Transmission Lines and Methods of Investigation

2.1 Outline

In this chapter discontinuities in transmission lines are defined, and some of the structures which traditionally have been investigated especially for microstrip and stripline and may occur in IDG are introduced. Then some relevant methods of investigation are mentioned. Finally the selected method for this research work will be presented.

2.2 Discontinuities and Their Various Types

A discontinuity in a transmission (i.e., any waveguide in general) line is caused by a sudden change in the geometry of the guide. Practical distributed circuits

made of propagating structures must inherently contain discontinuities. Many circuits, such as filters, mixers and oscillators involve several discontinuities.

The most common types of discontinuities in transmissions lines, some of which may occur in IDG, are open-ends, series gaps, bends, steps in width, T and cross junctions, as described below. There are some investigations about these discontinuities especially for microstrip and striplines and their studies may be helpful for the analysis of the IDG discontinuities.

Open-ends. Open-end discontinuities occur frequently in a number of circuits such as resonators, matching stubs and parallel coupled filters. Figure 2.1a shows an open-end discontinuity in microstrip and stripline. Fringing fields extending beyond the abrupt physical end of the metallic section may be accounted for by assuming some equivalent capacitances to be connected at the open end. When the frequency increases, the open-end tends to be a short circuit and when frequency decreases, it tends to be an open circuit. Therefore for all frequencies, its reflection coefficient magnitude is one and its phase is between 0 and 180 degree. This feature is the "end-effect".

Series gap. This discontinuity is useful in the design of dc blocks, end coupled filters, coupling elements to resonators, etc. [12, page 132]. Figure 2.1b shows a gap discontinuity in microstrip and stripline.

Bends. Bends may be formed by two lines of equal or unequal impedances. These are used for introducing flexibility in the layout of the circuit design. Figure 2.1c shows the geometry of a microstrip bend [12, page 140]. One of the common types of bends is the right-angle bend ($\alpha = 90$) or "corner" (Fig.2.1d).

Step in width. A step in width (Fig. 2.2a) is created at the junction of two lines with different widths. This discontinuity is encountered when microwave circuits need matching transformers, couplers, filters and transitions. Oliner [13] initially derived the equivalent circuits for a symmetric stripline step in width. In that

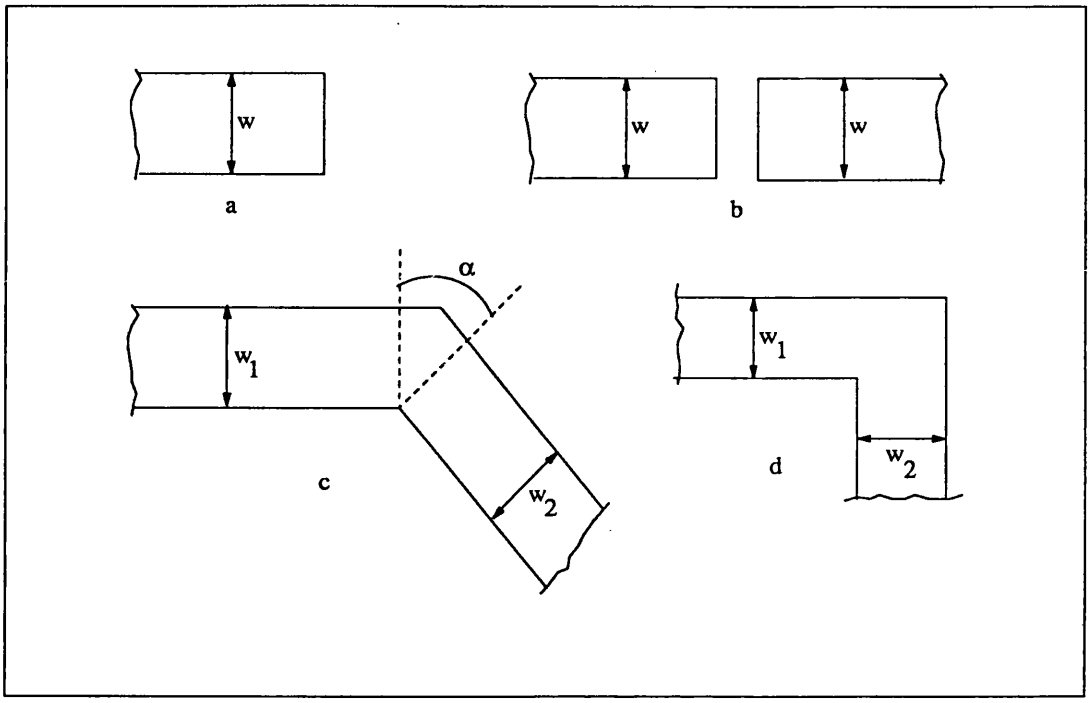

Figure 2.1: Some of the discontinuities in microstrip and striplines a)open-end b)series gap c)bend d)corner.

case the mode of propagation is TEM and the author used a conformal mapping technique to determine the field distribution. Then Spillard, Burchett, Pennock and Shepherd presented an improvement in the equivalent circuit for a symmetric stripline double step in width discontinuity. They analysed the problem by using a graded mesh FDTD algorithm [14].

T-junction. This discontinuity occurs in a wide variety of transmission lines. Examples range through stub-matching elements, stub filters, branch-line couplers and microstrip antenna element feeds, together with several other conceivable types of circuits [3, page 145]. Figure 2.2b shows a microstrip T-junction.

Cross-junction. One of the most common applications of a cross-junction is in the realization of low impedance stubs. This discontinuity has four ports. Figure 2.2c shows this discontinuity for microstrip line.

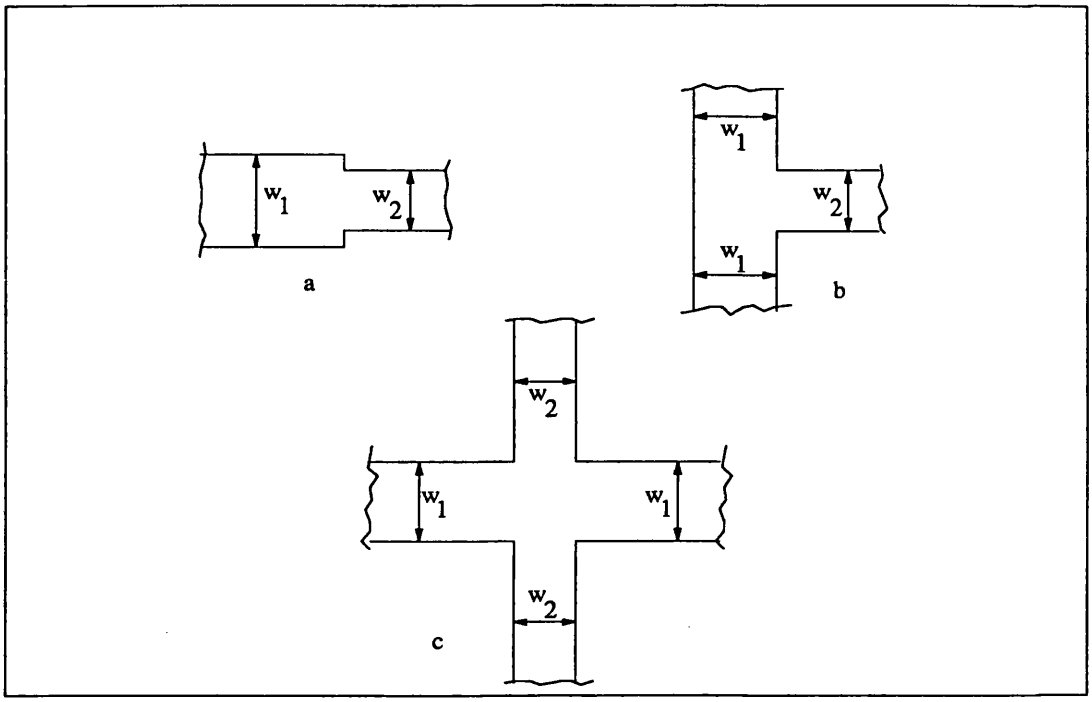

Figure 2.2: Some of the other discontinuities in microstrip and striplines step in width b)T-junction c)cross-junction.

2.3 Discontinuities in IDG

Some of the mentioned discontinuities especially the bend and step in width may occur in IDG. Additionally this guide may have some discontinuities like steps in dielectric and metal height. However none of them has been investigated yet and the present thesis is determined to do this task by an appropriate method. For this analysis, the discontinuity caused by a metal obstacle normal to the guide (Fig. 1.2), which is the fundamental case in the analysis of IDG discontinuities, will be considered.

2.4 Methods of Investigation

There are many methods to characterize and model passive microwave circuits. Some of them are used for quasi-static cases and some others for full wave analysis. For a special structure one has to choose a suitable method that should be as efficient and economical as possible in both CPU time and temporary storage computer requirements, although recent rapid advances in computers impose less severe restrictions on efficiency and economy of the method.

When we want to analyze a specific structure, we have to make a choice as to which method is best suited for the structure. Obviously, the choice is not unique. Therefore the user must make a critical assessment for each method.

2.4.1 Conformal Mapping Techniques (CMT)

Conformal mapping is widely used to determine normalized capacitance per unit length, and thus the characteristic impedance, of transmission lines by transforming a given conductor configuration into a 2-conductor, parallel-plate structure for which capacitance is easily found. As capacitance is invariant under conformal transformation, the result is the capacitance of the given structure [15].

In recent years Getsinger [15] used this technique to find the capacitances among 3 conductors. He described a technique in which conventional conformal mapping can be extended to analyze some transmission line configurations which cannot be reduced by symmetry to less than 3 separate conductors. Asymmetrical coupled stripline and 4-centre-strip CPW coupler were used as examples for the technique. Calculated values were in good agreement with results found by other techniques.

The conformal mapping of the boundary of a polygon in the first plane into the real axis in the second plane is called a Schwarz-Christoffel transformation [1,

page 888]. Cohn [16] used this mapping to calculate the characteristic impedance of odd and even modes of shielded broadside-coupled striplines. In all cases, the theory applied to strips of zero thickness, which may be approximated by metal-foil conductors sandwiched between dielectric plates filling the cross section.

In general, by applying conformal mapping techniques we can obtain C, L, and Z_0 (characteristic impedance of the line) of some transmission structures in the static and quasi-static cases [17]. This method needs a moderate CPU time and computer storage.

2.4.2 Finite Difference Method (FDM)

This technique consists basically of a method for solving the field equations by replacing the domain between the conductors by a finite set of points called mesh points and by solving the Laplace's equation (typically in electrical engineering) in finite difference form by digital computer. Certain precautions have to be taken into account when the method is used in an open-region problem in which the region is truncated to a finite size. Also, the method requires that mesh points lie on the boundary [18]. The technique can be extended, with certain restrictions, to transmission lines which are partially filled with dielectric material [19].

This method is well known to be the least analytic. The mathematical preprocessing is minimal and the method can be applied to a wide range of structures including those with odd shapes. A price one has to pay is numerical inefficiency [18, page 30]. The technique is particularly suited for the evaluation of capacitance, characteristic impedance and the attenuation of transmission line supporting TEM-mode by computer. Although this method needs a large storage and CPU time, it has a very good generality [18, page 30].

FDM is usually used together with a relaxation process. In this case an improve-

ment of speed of convergence is possible. In this method one starts with assumed values of the unknown function at the grid points. These values are modified successively as the new value for each point is equal to the old value subtracted by $a \times R$, where R is the "residual" and is equal to the old value of the point subtracted from the mean value of neighbouring points on the grid. The speed of convergence of the relaxation process is determined by the constant a [12, page 15].

2.4.3 Finite Difference Time Domain (FDTD) Method

This method uses FDM when discretising the time and space derivatives of Maxwell's equations. This method was first formulated by Yee [20] and later developed by Taflove and others [21]-[27]. the FDTD method has been shown to be a very versatile and effective method for a variety of EM problems, e.g. [20] and [28], and, more recently, it has been successfully applied to various microwave circuit problems [29]. It shows great promise in its flexibility in handling a variety of circuit configurations. Recently, FDTD methods have been used effectively to calculate the frequency-dependent characteristics of microstrip discontinuities [29] and [30]. Further efforts are being made to implement losses, variable mesh size and the nonlinearity by the FDTD procedure [29].

A benefit of the time-domain analysis is that a broad-band pulse may be used as the excitation and the frequency-domain parameters may be calculated over the entire frequency range of interest by Fourier transformation of the transient results [31].

A basic difficulty encountered in applying any method such as the FDTD to any problem is that the domain in which the field to be computed is open or unbounded. Since no computer can store an unlimited amount of data, a finite difference scheme over the whole domain is impractical. We must limit the extent

of our solution region. In other words, an artificial boundary must be enforced and suitable boundary conditions on it must be used to simulate the extension of the solution region to infinity [32, page 184]. Simplification of the method has been achieved by using the simple form of the absorbing boundary condition [33]. This simple absorbing boundary condition yields good results for the broad class of microstrip circuits.

A difference between the FDM and the FDTD methods is that the FDM usually starts from wave equation while the FDTD starts from Maxwell's equations.

As for the latest research, three examples are mentioned: first, Chia, Burkholder and Lee [34] have introduced three hybrid methods for analyzing the EM scattering from 3-D cavities. In these hybrid methods, the FDTD method is used to characterize the termination sections of cavities in terms of termination reflection matrices.

Second, Demarest, Plumb, and Huang [35] have presented an extension of FDTD technique that allows the model of scatterers that are buried in stratified grounds and illuminated by an incoming plane wave. This technique utilizes well-known expressions for the fields transmitted and reflected from stratified media to separate the outgoing fields caused by the scatterer from the total fields. This allows the standard absorbing boundary conditions (such as Mur's) to close the FDTD lattice with minimal reflections. The numerical results presented showed that this method can be used either in a total-field mode or in a scattered-field mode.

Third, Tran, Houshmand, and Itoh [36] have applied the spectral domain method (SDM) and FDTD method to the analysis of microstrip lines coupled through thick apertures. Numerical results show that the finite metallization thickness of the common ground plane affected the coupling characteristics of the structure significantly. Comparisons between the extended SDM and FDTD indicate good agreement between the two proposed methods and also imply results produced

by these two methods are valid and accurate. Both the extended SDM and FDTD are quite flexible; therefore, they can also be applied to other types of discontinuities in printed antennas and circuits.

2.4.4 Finite Element Method (FEM)

In this method the region of interest is divided into a number of subregions. The field in each element is approximated by a simple algebraic expansion, usually a low-degree polynomial, then the values of the field on a finite set of nodal points are found as the solution of a set of linear algebraic equations. In general, the FEM needs large storage requirement, moderate to large CPU time and small preprocessing but its generality is very good [18, page 30]. In some cases using this method, some false and unwanted results are produced.

Although the FDM and the method of moments (MoM) (see section 2.4.5) are conceptually simpler and easier to program than the FEM, the FEM is a more powerful and versatile numerical technique for handling problems involving complex geometries and inhomogeneous media. The systematic generality of the method makes it possible to construct general-purpose computer programs for solving a wide range of problems.

Neale and Gopinath [37] used this method to calculate the quasi-static inductance of step in width, T-junction and right-angle bend of microstrip discontinuities. Since the formulation is based on quasi-static assumptions, the data is valid up to some maximum frequency. When this data is used in conjunction with the capacitance data available elsewhere, a range of discontinuities have been characterized.

As a recent example, Alam *et al.* [38] have employed FEM to analyse the characteristics of propagating, evanescent modes, and complex modes in finline. They

developed mixed-interpolation-type triangular elements, where no spurious solutions appear and consistency with published results was obtained. The existence of the complex modes for both the even mode and odd mode in finlines is found for particular structural parameters and in a certain frequency range.

2.4.5 Method of Moments (MoM)

The method of moments or moment method is more sophisticated mathematically and in return achieves greater computational efficiency. For the potential problem, the potential is expressed as an integral of the product of the charge density and a function known as the Green's function, which is a function that expresses a relationship between a quantity at an observation point and a unity source. Much of the effort in using the MoM involves calculation of the Green's function, which frequently is determined as the sum of an infinite series. The charge density is expressed as a linear combination of a set of known functions [39, page 5].

The authors of [40] have mentioned in their publication that this method is a general one and can be used to compute the lumped capacitance of any microstrip discontinuity such as bends and T-junctions. They also used this method to calculate the capacitance per unit length of a microstrip transmission line and the characteristic impedance is then obtained by assuming TEM mode propagation [41]. The table in this publication shows that when $(\frac{w}{h})$ increases the Z_0 decreases and when ϵ_r increases the Z_0 also will decrease (where w is width of the strip, Z_0 is characteristic impedance of the line and h is thickness of the substrate).

2.4.6 Mode Matching Method (MMM)

This method is applied to the problem of scattering into waveguide structures on both sides of the discontinuity. The fields on both sides of the discontinuity are expanded in terms of the modes in the respective regions with unknown coefficients [42]. Sometimes when this method is used to find the guided mode in a waveguide it is called the field-matching method [18, page 13]. In general this method needs moderate storage requirement, small and moderate CPU time, moderate preprocessing and its generality is good [18, page 30].

Authors of [43] used this method for calculating the dynamic (frequency-dependent) properties of various microstrip discontinuities such as unsymmetrical crossings, T-junction, right-angle bends, impedance steps and filter elements. Itoh and Chu used this method to analyze the microstrip step-discontinuity problem based on the waveguide model [44].

As a recent example, a full-wave analysis based on this method was applied to analyse cascaded junction discontinuities of coplanar type transmission lines, coplanar waveguide (CPW) and finline by Huang and Itoh [45]. They also considered the influence of metallization thickness on cascaded discontinuities in circuits and by numerical results, they concluded that metallization thickness effect can be magnified by the standing wave between two cascaded junction discontinuities, especially at a quarter wavelength separation distance.

2.4.7 Transverse Resonance Technique (TRT)

This method was proposed by Sorrentino and Itoh [46] and [47] to alleviate the computational effort. This method is somewhat similar to the mode matching method and is suited for characterization of the discontinuity in planar waveguide structures and uniform finlines and finline discontinuities [18, page 14]. In gen-

eral, this method needs small to moderate storage requirement and CPU time, moderate preprocessing and has marginal generality [18, page 30].

With this technique, one looks for the resonances of a cavity containing the discontinuity under investigation. At each frequency, the dimensions of the cavity are changed until resonance is found. From the knowledge of the resonant dimensions, the scattering parameters are calculated [48].

2.4.8 Integral Equation Method (IEM)

This method is a means of casting a problem such that a known field quantity, i.e. the field at a boundary, is linked to the unknown parameter by means of an integral operator. These techniques require the use of Green's functions [49]. In general, this method needs small and moderate storage requirement and CPU time, moderate preprocessing and has good generality [18, page 30].

Benedek and Silvester calculated the excess charge density distribution near gaps and steps in microstrip line by solution of the singular equation [50]. Then they formulated the electrostatics of the excess charge distribution near microstrip right-angle bends, T junction and crossing by this method and used a projection method for their final solution [51].

2.4.9 Boundary Element Method (BEM)

In this method, the problem is formulated as an integral equation over the physical boundaries by using appropriate Green's function and applying Green's identity or the weighted residual method. The equation is then solved by a discretisation procedure similar to that used in the FEM. However, by confining the analysis to the boundaries, the BEM reduces the dimensionality of the problem

by one and, therefore, requires smaller computer memory than does the conventional FEM [52]. This method is a combination of the boundary integral equation and a discretisation technique similar to the element algorithm as applied to the boundary [53] and [54] . Essentially, the wave equation for the volume is converted to the surface integral equation by way of the Green's identity. The surface integrals are discretised into N segments (elements), and their evaluation in each element is performed after the field quantities are approximated by polynomials [18, page 6].

Eid, Mikati, and Razzak [52] applied this method to various types of transmission lines like striplines, microstrip lines with isotropic or anisotropic substrate, coupled microstrip lines, and planar stripline junctions. They believed that the method provides a great economy in memory storage requirements and running time. Their investigation shows, when the ratio of the strip width to the dielectric thickness increases, impedance of a shielded microstrip decreases and when the relative permittivity of dielectric substrate increases, the impedance decreases as well.

2.4.10 Generalized Scattering Matrix Method (GSMM)

This method can be used for analyzing complicated discontinuity problems and characterizing cascaded discontinuities. The generalized scattering matrix combines the mutual interaction of two discontinuities via dominant and higher-order modes. For characterizing a single discontinuity, this method has to be used with other techniques like MMM [18, page 19]. It should be noted that the use of GSMM is increasingly more important as the distance between two junctions is smaller [55].

Chu and Itoh [55] applied this method to the problems of cascaded step discontinuity and an offset step discontinuity. In their investigation a waveguide model

had been presumed to be applicable for analysis. Individual discontinuities were characterized first and the results used for the description of the composite discontinuity via the generalized scattering matrix technique. They showed, for the step discontinuity a small offset d (where d is the distance between the axes of two strips) significantly affected the scattering characteristic of the discontinuity. The effect of the first odd-mode cut-off is exhibited as soon as the eccentricity is non zero. Also, for d=0.5 cm, the effect of second-(even-) mode cut-off is quite small due to the fact that the centre of the smaller waveguide is located at the second-mode null and, hence, little coupling via this mode exists.

2.4.11 Spectral Domain Method (SDM)

This method allows an elegant and closed-form equation formulation for a broad class of MIC problems which reduces the analysis by one dimension compared to the original field problem [56]. SDM is a Fourier-transformed version of the integral equation method applied to microstrip or other printed line structures. It is one of the most preferred methods in recent decades. The method is known to be efficient but is restricted in general to well-shaped structures that involve infinitely thin conductors [18, page 22].

SDM results in a particularly low-order linear system of equations and provides design-relevant parameters in both the spectral and the space domain. In so far as it may require a considerable amount of analytical preprocessing to achieve the highest efficiency, it is a hybrid fields method. A preference for the SDM for MIC problems is to some extent confirmed by the fact that the majority of the rigorous frequency-dependent MIC design information has been generated using this technique [56]. In general this method needs small storage requirement and CPU time but large preprocessing and has marginal generality [18, page 30].

2.4.12 Transmission Line Matrix Method (TLM)

This method is a general numerical technique that can be applied to obtain an approximate solution to the time-dependent form of Maxwell's equations in the presence of complex environments. In general the TLM method needs moderate to large storage requirement and CPU time, small preprocessing but its generality is very good [18, page 30].

In this method the field is converted to a 3-D equivalent network problem. In the generic form of the 3-D TLM method, the space is discretised into a 3-D lattice with a period Δl and six field components are represented by a hybrid TLM cell. Boundaries corresponding to the electric wall and the magnetic wall are represented by short-circuiting shunt nodes and open-circuiting shunt nodes on the boundary. Magnetic and dielectric materials can be introduced by adding short-circuited series stubs of the length $\Delta l/2$ at the series nodes (magnetic field components) and open-circuited $\Delta l/2$ stubs at the shunt nodes (electric field components). The losses can be represented by resistive loading the shunt nodes. After the time-domain response is obtained, the frequency response is found by Fourier transform [18, page 6].

Simons and Sebak [57] have used a simulation program based on the 3-D symmetrical-condensed TLM model for the radar cross-section analysis of finite-sized conducting and dielectric objects. Reasonable agreement between the TLM results and a variety of published data has been obtained. To obtain accurate results, the spatial discretisation of the problem domain should meet two criteria. The first requires appropriate discretisation of the object in term of the number of spatial cells Δl per λ, where λ is the wavelength of the highest frequency at which accurate results are desired. The second criterion that must be met to ensure accurate characterisation is a sufficient distance from the scattering object to the exterior mesh boundary.

2.5 Conclusion

For the present research work the FDTD method has been chosen over the other methods because:

1- this method is conceptually simple, the algorithm does not require the formulation of integral equations and relatively complex scatters can be treated without the inversion of large matrices [32, page 192], which occurs in some methods such as the MoM.

2-It is simple to implement for complicated, inhomogeneous conducting or dielectric structures because constitutive parameters (σ, μ, and ϵ) can be assigned to each lattice point [32, page 192]. In addition, this is very general (in comparison with some methods such as the TRT method) and can be applied to model many other structures and microwave components.

3-Its accuracy can be made as high as desired by using a sufficiency of cells. Conversely, engineering estimates of low accuracy can be made with relatively few cells [58, page 3].

4-The frequency-domain design data are obtained from the Fourier transform of the calculated time-domain field values, therefore dispersive characteristics of the structures can be investigated by FDTD.

5-Its computer memory requirement is not prohibitive for many computer structures of interest [32, page 192]. However its time and computer requirements are larger than those methods which need less preprocessing.

6-The FDTD method is a full-wave analysis which is applicable over a wide range of frequencies while some methods (e.g. the CMT) are applicable only for static and quasi-static analysis.

7-In comparison with the TLM method, which has been widely used in the numerical solution of the electromagnetic eigenvalue problems in the time domain, some researchers believe that the FDTD method is preferred to the TLM method. For example Choi and Hoefer [29] believe that the FDTD method needs less overal CPU time and memory under identical simulation conditions. They mentioned in their publication that other advantages of FDTD over TLM method included the absence of dielectric boundary errors in the treatment of 3-D inhomogeneous planar structures, such as microstrip line. Sheen, Abouzahra and Kong [31] in their research have chosen FDTD method over the other discrete methods, because they believe that this method is extremely efficient and its implementation is quite straight forward.

Johns in [59] offers some comments on comparisons between the TLM and the finite difference methods. Finally he concluded that these two methods complement each other rather than compete with each other. Each leads to a better understanding of the other.

Chapter 3

FDTD Fundamentals

3.1 Outline

In this chapter the FDTD algorithm is introduced. Consideration is given to the cell and time step sizes, stability conditions, choice of the excitation pulse, and absorbing boundary conditions. Determination of the scattering parameters of the guiding is also described.

3.2 Yee's Finite Difference Algorithm

The FDTD method was first formulated by Yee [20]. Its original formulation is based on sampling the electromagnetic field at distinct points in a space-lattice and at successive, equally spaced, instants of time. This discretisation of Maxwell's curl equations leads to a set of algebraic equations that provides an explicit algorithm for simulating the evolution of the electromagnetic field in a domain consisting of isotropic, non-dispersive media.

3.2.1 Maxwell's Equations and the Equivalent set of Finite Difference Equations

Maxwell's equations in an isotropic medium [20]

$$\frac{\partial \vec{B}}{\partial t} + \nabla \times \vec{E} = 0 \tag{3.1}$$

$$\frac{\partial \vec{D}}{\partial t} - \nabla \times \vec{H} = -\vec{J} \tag{3.2}$$

$\vec{B} = \mu \vec{H}$

$\vec{D} = \epsilon \vec{E}$

where $\vec{B}$ is magnetic flux density (or magnetic induction), $\vec{H}$ is magnetic field intensity, $\vec{D}$ is electric flux density, and $\vec{E}$ is electric field intensity.
$\vec{J}$, μ, and ϵ are assumed to be given as a function of space and time.

Usually there is no current source in the region of the computation ($\vec{J} = 0$), and vector equations 3.1 and 3.2 represent a system of six scalar equations which can be expressed in a rectangular coordinate system (x, y, z) as:

$$\frac{\partial B_x}{\partial t} = \frac{\partial E_y}{\partial z} - \frac{\partial E_z}{\partial y} \tag{3.3}$$

$$\frac{\partial B_y}{\partial t} = \frac{\partial E_z}{\partial x} - \frac{\partial E_x}{\partial z} \tag{3.4}$$

$$\frac{\partial B_z}{\partial t} = \frac{\partial E_x}{\partial y} - \frac{\partial E_y}{\partial x} \tag{3.5}$$

$$\frac{\partial D_x}{\partial t} = \frac{\partial H_z}{\partial y} - \frac{\partial H_y}{\partial z} \tag{3.6}$$

$$\frac{\partial D_y}{\partial t} = \frac{\partial H_x}{\partial z} - \frac{\partial H_z}{\partial x} \tag{3.7}$$

$$\frac{\partial D_z}{\partial t} = \frac{\partial H_y}{\partial x} - \frac{\partial H_x}{\partial y} \tag{3.8}$$

Following Yee's notation, by definition a grid point in the solution region is given as:

$$(i,j,k) = (i\Delta x, j\Delta y, k\Delta z) \tag{3.9}$$

and any function of space and time as:

$$F^n(i,j,k,t) = F(i\Delta x, j\Delta y, k\Delta z, n\Delta t) \tag{3.10}$$

where $\delta = \Delta x = \Delta y = \Delta z$ is the space increment, Δt is the time increment, while i, j, k, and n are integers.

A set of finite difference equations for 3.3-3.8 that will be found convenient for a perfectly conducting boundary condition are as follows:

$$\begin{aligned} H_x^{n+\frac{1}{2}}(i,j,k) &= H_x^{n-\frac{1}{2}}(i,j,k) - \alpha_H(E_z^n(i,j+1,k) - \\ &\quad E_z^n(i,j,k) - E_y^n(i,j,k+1) + E_y^n(i,j,k)) \end{aligned} \tag{3.11}$$

$$\begin{aligned} H_y^{n+\frac{1}{2}}(i,j,k) &= H_y^{n-\frac{1}{2}}(i,j,k) - \alpha_H(E_x^n(i,j,k+1) - \\ &\quad E_x^n(i,j,k) - E_z^n(i+1,j,k) + E_z^n(i,j,k)) \end{aligned} \tag{3.12}$$

$$\begin{aligned} H_z^{n+\frac{1}{2}}(i,j,k) &= H_z^{n-\frac{1}{2}}(i,j,k) - \alpha_H(E_y^n(i+1,j,k) - \\ &\quad E_y^n(i,j,k) - E_x^n(i,j+1,k) + E_x^n(i,j,k)) \end{aligned} \tag{3.13}$$

$$\begin{aligned} E_x^{n+1}(i,j,k) &= E_x^n(i,j,k) + \alpha_E(H_z^{n+\frac{1}{2}}(i,j,k) - \\ &\quad H_z^{n+\frac{1}{2}}(i,j-1,k) - H_y^{n+\frac{1}{2}}(i,j,k) + H_y^{n+\frac{1}{2}}(i,j,k-1)) \end{aligned} \tag{3.14}$$

$$\begin{aligned} E_y^{n+1}(i,j,k) &= E_y^n(i,j,k) + \alpha_E(H_x^{n+\frac{1}{2}}(i,j,k) - \\ &\quad H_x^{n+\frac{1}{2}}(i,j,k-1) - H_z^{n+\frac{1}{2}}(i,j,k) + H_z^{n+\frac{1}{2}}(i-1,j,k)) \end{aligned} \tag{3.15}$$

$$\begin{aligned} E_z^{n+1}(i,j,k) &= E_z^n(i,j,k) + \alpha_E(H_y^{n+\frac{1}{2}}(i,j,k) - \\ &\quad H_y^{n+\frac{1}{2}}(i-1,j,k) - H_x^{n+\frac{1}{2}}(i,j,k) + H_x^{n+\frac{1}{2}}(i,j-1,k)) \end{aligned} \tag{3.16}$$

where:

$$\alpha_E = \frac{\Delta t}{\epsilon \delta} \tag{3.17}$$

$$\alpha_H = \frac{\Delta t}{\mu \delta} \tag{3.18}$$

For convenience, the six field locations are considered to be interleaved in space as shown in Fig. 3.1, which is a drawing of the FDTD unit cell [20].

The advantages of this field arrangement are that centered differences are realized in the calculation of each field component and that continuity of tangential field components is automatically satisfied.

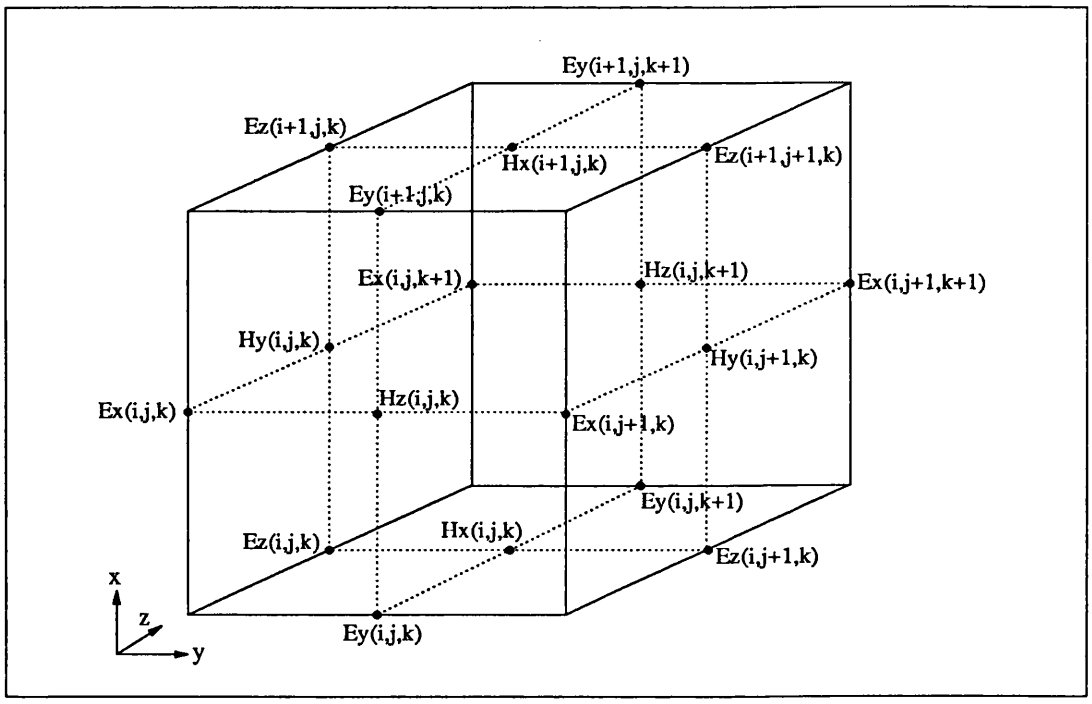

Figure 3.1: Field component placement in the FDTD unit cell.

3.3 Determining the Cell Size

The choice of the cell size is critical in applying FDTD. It must be small enough to permit accurate results at the highest frequency of interest, and yet be large

enough to keep the number of cells and time steps at reasonable values.

Cell size is directly affected by the material present. For example, at a given frequency the greater permittivity causes smaller wavelength and thus smaller cell size is required.

The fundamental constraint is that the cell size must be much less than the smallest wavelength for which accurate results are desired. For the ideal case, when rise and fall times of the pulse are zero, based on the Nyquist sampling theorem, there must be at least two samples per spatial period (wavelength) in order for the spatial information to be adequately sampled. Because our sampling is not exact, and our smallest wavelength is not precisely determined, more than two samples per wavelength are required to ensure the accuracy of the computed results, the spatial increment δ must be small compared to the wavelength (usually $\leq \frac{\lambda}{10}$) or the minimum dimension of the scatterer at the highest frequency (shortest wavelength), meaning that the side of each cell should be $\frac{1}{10}\ \lambda$ or less [58, page 31].

3.4 Time Step Size and Stability

Once the cell size is selected, the maximum size of the time step (the time increment, Δt) is determined by the Courant stability. Smaller time step sizes are permissible, but do not generally result in computational accuracy improvements. A large time step results in instability. To understand the basis for the Courant condition, consider a plane wave propagating through a FDTD grid. In one time step any point on this wave must not pass through more than one cell, because during one time step FDTD can propagate the wave only from one cell to its nearest neighbours. To determine this time step constraint a plane wave direction is picked so that the plane wave propagates most rapidly between field point locations. This direction will be prependicular to the lattice planes of the

FDTD grid. For a grid of dimension d (where d=1, 2 or 3), with all cell sides equal to Δu , it is found that with v the maximum velocity of propagation in any medium in the problem, this condition is:

$$v\Delta t \leq \frac{\Delta u}{\sqrt{d}} \tag{3.19}$$

for stability [58, page 32].

More generally for a 3-D rectangular grid [24]

$$v\Delta t \leq \frac{1}{\sqrt{\frac{1}{\Delta x^2}+\frac{1}{\Delta y^2}+\frac{1}{\Delta z^2}}} \tag{3.20}$$

where v is the maximum wave phase velocity within the model.

Since a cubic cell is used with $\Delta x = \Delta y = \Delta z = \delta$, Eq. 3.20 becomes:

$$\frac{v\Delta t}{\delta} \leq \frac{1}{\sqrt{d}} \tag{3.21}$$

and the final form is:

$$\Delta t = k_s \frac{\delta}{v} \tag{3.22}$$

k_s is stability factor and for the 3-D case is:

$$k_s \leq \frac{1}{\sqrt{3}} \tag{3.23}$$

For practical reasons, it is best to choose the ratio of time increment to spatial increment as large as possible yet satisfying Eq. 3.21 [32, page 184].

3.5 Choice of Excitation Pulse.

When using the scattered field FDTD formulation the incident field must be specified. Many varieties of waveform are possible, but experience has led to

the Gaussian pulse as the incident waveform of choice. The exception of this is when frequency-dependent materials are included, in which case a smoothed cosine pulse has advantages [58, page 29].

A Gaussian pulse has a smooth waveform in time (or distance), and its Fourier transform (spectrum) is also a Gaussian pulse centered at zero frequency. These unique properties make it a perfect choice for investigating the frequency-dependent characteristics of the discontinuities via the Fourier transform of the impulse response.

A Gaussian pulse in time has the following mathematical form:

$$f(t) = A_0 e^{-\left(\frac{t-t_f}{y_p}\right)^2} \tag{3.24}$$

It has a maximum amplitude A_0 at $t = t_f$. In section 5.4 it will be discussed that value of y_p affects the bandwidths of time and frequency.

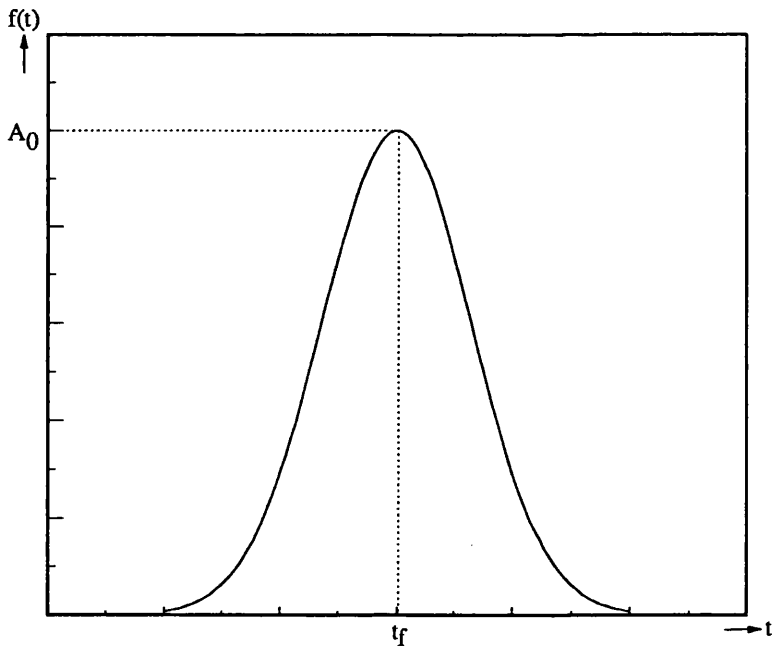

Figure 3.2: Gaussian pulse as the function of time.

3.6 Absorbing Boundary Conditions (ABCs)

As mentioned in 2.4.3, due to the limited storage space of computers, numerical computation domains have to be finite. Therefore, a certain type of boundary condition, which is called the Absorbing Boundary Condition (ABC), needs to be applied on the outer boundaries of the computation domain to simulate the unbounded physical space. Ideally absorbing boundary conditions cannot absorb the outgoing wave completely, and generate some numerical error in the solution. With better absorbing boundary conditions, not only will the numerical solutions be more accurate, but the outer boundaries can be brought closer to the modelled targets, resulting in considerable savings on computer memory space and computation time.

Over the last few decades, a number of ABCs have been proposed and several are in common use. The ABCs most often referred to in the literature are those derived by Engquist and Majda [60] with discretisation given by Mur [33]. The scheme of starting from the wave equation and deriving one-way equations from it that allow propagation in the outward direction only was proposed by them which is most popular in FDTD applications.

The first order ABC in the computing volume proposed by Mur [33] is still reasonably effective for plane wave or quasi-plane wave incidence, as in the cases of microstrip and boxed coplanar line. He also employed a second-order radiation condition to improve the accuracy of the results that can be used for both 2 and 3-Dimensional configurations.

Fang and Mei [61] introduced the superabsorbtion technique, in which they used ABCs to estimate both the E and the H field at a point on the boundary and then combine the results in such a way as to improve the overall accuracy. Bi *et al.* [62] introduced a Dispersive Boundary Condition (DBC) for microstrip component analysis using FDTD method, which allowed the dispersion characteristics of the

wave to be used as a criterion for designing absorbing boundary conditions. It included a linear combination of a range of phase velocities for the outgoing wave.

Recently, Berenger [63] published a new technique of free-space simulation for solving unbounded electromagnetic problems with the FDTD method. Referred to as Perfectly Matched Layer (PML), this new technique is based on the use of an absorbing layer especially designed to absorb the electromagnetic waves without reflection. Then Katz, Thiele, and Taflove [64] verified Berenger's strong claims for PML for 2-D FDTD grids and extended and verified PML for 3-D FDTD grids. They believe PML is greater than 40 dB more accurate than second-order Mur, and PML works just as well in 3-D as does in 2-D.

In Chapter 4, details and practical implementaions of the 1st order Mur and PML ABCs will be described. In Chapter 5, these two ABCs will be used at both ends of a rectangular waveguide during the implementation of the FDTD method in this guide and the results will be discussed.

3.7 Obtaining the Frequency Response and Scattering Parameters

The designer of microwave circuits usually needs the parameters of the structure under study as a function of frequency. Since the primary results of the FDTD algorithm are in the time domain, the frequency parameters of the structure are habitually obtained by means of a Fourier transform using the Fast Fourier Transform (FFT). The FFT is used to speed up the conversion time from the time domain to the frequency domain response [65].

When the FFT is used for processing the time sequences provided by FDTD there is an error involved in obtaining the scattering parameters, which is due

to the truncation of the time response. The number of time steps needed to reduce this error increases with the quality factor of the circuit. When dielectric discontinuities in waveguides involving high permittivity media are analysed, the simulation time can be excessively long.

After obtaining transient results by FDTD, the frequency-dependent scattering matrix coefficients are calculated:

$$[V]^r = [S][V]^i \tag{3.25}$$

where $[V]^r$ and $[V]^i$ are the reflected and incident voltage vectors, respectively, and [S] is the scattering matrix.

To calculate the frequency-dependence of for example, $S_{i,j}$ (scattering parameter between ports j, i), the ratio of Fourier transform of transient waveforms at port i, j must be obtained

$$S_{i,j}(f) = \frac{\mathcal{F}[V_i(t)]}{\mathcal{F}[V_j(t)]} \tag{3.26}$$

Chapter 4

First Order Mur's and Perfectly Matched Layer Absorbing Boundary Conditions

4.1 Outline

The purpose of the Absorbing Boundary Condition (ABC), as mentioned in section 3.4, is in simulating a boundary that permits the electromagnetic waves to propagate through it with a minimum of reflection. With this the size of the computations domain required for characterizing open structures is limited to a finite volume. In this chapter, the first order Mur's ABC is introduced as an effective ABC which is the simplest to implement and has the lowest requirement of computer memory. Then the Perfectly Matched Layer (PML) will be introduced as the newest method for a potentially perfect ABC, but requiring much more computer memory.

4.2 Absorbing Boundary Condition

Assume that the structure under investigation is unbounded along the z axis. The purpose of ABC is to truncate the computation at $z = m\Delta z$ (where m is an integer). If no ABC is considered, the values of the field at plane $(m+1)\Delta z$ are unspecified and hence, in general, there will be reflection of the field from that plane.

To prevent creating this reflection two kinds of ABC are considered: a) 1st order Mur's ABC, (Fig. 4.1a) which is located at plane $m\Delta z$. By using formulation of this ABC, the tangential fields at plane $(m+1)\Delta z$ which satisfy the wave equation are calculated. b) PML ABC, (Fig. 4.1b) which is consists of imposing a lossy layer of thickness d such that the field amplitude decays in this layer. This lossy layer is so designated as to insure the minimum reflection from the plane $m\Delta z$.

4.3 First Order Mur's ABC

Consider a 3-D wave equation in Cartesian coordinates

$$U_{xx} + U_{yy} + U_{zz} - \frac{1}{v_p^2} U_{tt} = 0 \tag{4.1}$$

where U is a scalar field component, U_{xx} is the second partial derivative with respect to x, and v_p is the wave phase velocity. If the partial differential operator is introduced as:

$$L \equiv D_x^2 + D_y^2 + D_z^2 - \frac{1}{v_p^2} D_t^2 \tag{4.2}$$

which uses the notation $D_x^2 \equiv \frac{\partial^2}{\partial x^2}$, $D_y^2 \equiv \frac{\partial^2}{\partial y^2}$, $D_z^2 \equiv \frac{\partial^2}{\partial z^2}$, and $D_t^2 \equiv \frac{\partial^2}{\partial t^2}$. Now the wave equation can be written as:

$$LU = 0 \tag{4.3}$$

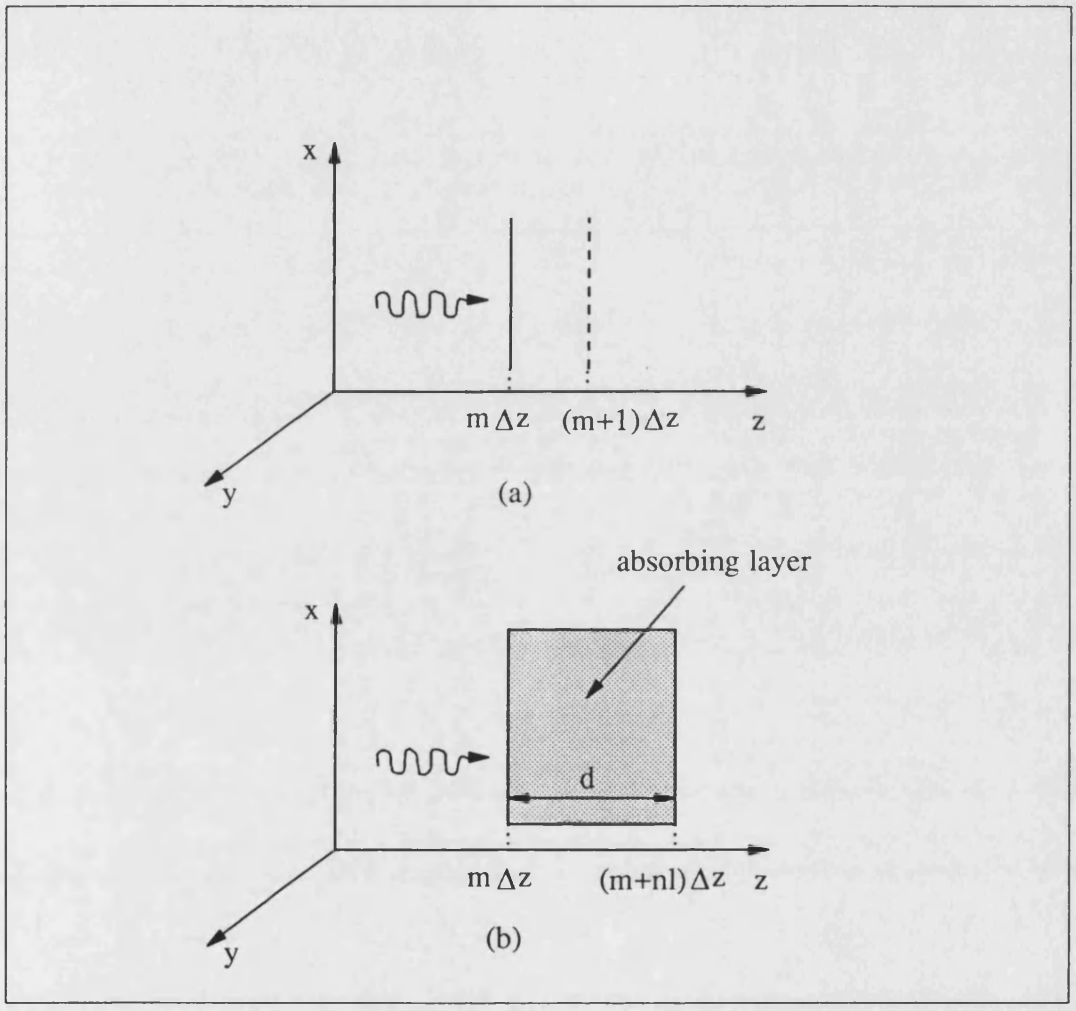

Figure 4.1: Positions of ABCs at plane $m\Delta z$ for a) 1st order Mur's ABC b) PML ABC.

L can be factorised in the following manner:

$$LU = L^+L^-U = 0 \tag{4.4}$$

where

$$L^- = D_z - \frac{D_t}{v_p}\sqrt{1-S^2} \tag{4.5}$$

$$L^+ = D_z + \frac{D_t}{v_p}\sqrt{1-S^2} \tag{4.6}$$

$$S = \left[\left(\frac{D_x}{D_t/v_p}\right)^2 + \left(\frac{D_y}{D_t/v_p}\right)^2\right]^{\frac{1}{2}} \tag{4.7}$$

Engquist and Majda [60] showed that at a boundary, for example z=0, the application of L^- to the wave component, U, will completely absorb a plane wave propagating towards the boundary at z=0 at an arbitrary angle, θ. Hence there is a perfect analytical absorbing boundary at z=0 by using:

$$L^-U = 0 \tag{4.8}$$

Similarly for the opposite boundary located at z=h by using:

$$L^+U = 0 \tag{4.9}$$

a plane wave striking this boundary will be absorbed. By using a Taylor's series approximation to the term $\sqrt{1-S^2}$, two form of the Mur's approximation may be made [33]

$$First\ Order : \sqrt{1-S^2} = 1 + O(S^2) \tag{4.10}$$

$$Second\ Order : \sqrt{1-S^2} = 1 - \frac{1}{2}S^2 + O(S^4) \tag{4.11}$$

For the simpler first order approximation, substituting $\sqrt{1-S^2}$=1 in Eq. 4.5 and 4.6, the 1st order Mur's ABC is obtained for application at z=0:

$$(D_z - \frac{D_t}{v_p})U = 0 \tag{4.12}$$

and for the boundary at z=h:

$$(D_z + \frac{D_t}{v_p})U = 0 \tag{4.13}$$

For practical implementation of this ABC consider a single frequency plane wave with velocity v_p with its plane perpendicular to the z direction, at $z = 0$ there is an outgoing wave towards $-z$ direction . This wave will be absorbed if at $z = 0$ Eq. 4.12 is applied:

$$\frac{\partial U}{\partial z} - \frac{1}{v_p}\frac{\partial U}{\partial t} = 0 \tag{4.14}$$

To discretise the above Equation, for example for the component E_x, regarding Fig. 4.2 a, at node $(i, j, 0)$ for modal time $(n + 1)\Delta t$ there is an imaginary node $(i, j, \frac{1}{2})$ at modal time $(n+0.5)\Delta t$. Using central difference and an average of adjacent points in the time domain:

$$\frac{\partial}{\partial z}(E_x^{n+\frac{1}{2}}(i,j,\tfrac{1}{2})) = \tfrac{1}{2}[\tfrac{\partial}{\partial z}E_x^{n+1}(i,j,\tfrac{1}{2}) + \tfrac{\partial}{\partial z}E_x^{n}(i,j,\tfrac{1}{2})]$$

$$= \tfrac{1}{2}[\tfrac{E_x^{n+1}(i,j,1)-E_x^{n+1}(i,j,0)}{\Delta z}] + \tfrac{1}{2}[\tfrac{E_x^{n}(i,j,1)-E_x^{n}(i,j,0)}{\Delta z}]$$

similarly:

$$\frac{\partial}{\partial t}(E_x^{n+\frac{1}{2}}(i,j,,\tfrac{1}{2})) = \tfrac{1}{2}[\tfrac{\partial}{\partial t}E_x^{n+\frac{1}{2}}(i,j,0) + \tfrac{\partial}{\partial t}E_x^{n+\frac{1}{2}}(i,j,1)]$$

$$= \tfrac{1}{2}[\tfrac{E_x^{n+1}(i,j,0)-E_x^{n}(i,j,0)}{\Delta t}] + \tfrac{1}{2}[\tfrac{E_x^{n+1}(i,j,1)-E_x^{n}(i,j,1)}{\Delta t}]$$

If the above derivatives are substituted in Eq. 4.14 the discretised form of 1st order Mur's Equation for the ABC at z=0 is obtained:

$$E_x^{n+1}(i,j,0) = E_x^{n}(i,j,1) + \frac{v\Delta t - \Delta z}{v\Delta t + \Delta z}[E_x^{n+1}(i,j,1) - E_x^{n}(i,j,0)] \tag{4.15}$$

If there is the same ABC at z=$(m$+1$)\Delta z$, for the above mentioned wave but outgoing toward the $+z$ direction, it will be absorbed if:

$$\frac{\partial U}{\partial z} + \frac{1}{v}\frac{\partial U}{\partial t} = 0 \tag{4.16}$$

For discretising the above Equation, regarding Fig. 4.2 b, consider an imaginary point at position $(i, j, m + \frac{1}{2})$ and time $(n + \frac{1}{2})\Delta t$. Then:

$$\frac{\partial}{\partial z}(E_x^{n+\frac{1}{2}}(i,j,m+\tfrac{1}{2}) = \tfrac{1}{2}[\tfrac{\partial}{\partial z}E_x^{n+1}(i,j,m+\tfrac{1}{2}) + \tfrac{\partial}{\partial z}E_x^{n}(i,j,m+\tfrac{1}{2})]$$

$$= \tfrac{1}{2}[\tfrac{E_x^{n+1}(i,j,m+1)-E_x^{n+1}(i,j,m)}{\Delta z}] + \tfrac{1}{2}[\tfrac{E_x^{n}(i,j,m+1)-E_x^{n}(i,j,m)}{\Delta z}]$$

similarly:

$$\frac{\partial}{\partial t}(E_x^{n+\frac{1}{2}}(i,j,,m+\tfrac{1}{2})) = \tfrac{1}{2}[\tfrac{\partial}{\partial t}E_x^{n+\frac{1}{2}}(i,j,m+1) + \tfrac{\partial}{\partial t}E_x^{n+\frac{1}{2}}(i,j,m)]$$

$$= \tfrac{1}{2}[\tfrac{E_x^{n+1}(i,j,m+1)-E_x^{n}(i,j,m+1)}{\Delta t}] + \tfrac{1}{2}[\tfrac{E_x^{n+1}(i,j,m)-E_x^{n}(i,j,m)}{\Delta t}]$$

Again the above two derivatives are substituted in Eq. 4.16, the discretised form of 1st order Mur's ABC at z=$(m + 1)\Delta z$ will be:

$$E_x^{n+1}(i,j,m+1) = E_x^{n}(i,j,m) + \frac{v\Delta t - \Delta z}{v\Delta t + \Delta z}[E_x^{n+1}(i,j,m) - E_x^{n}(i,j,m+1)] \tag{4.17}$$

If the wave contains a set of different frequencies where the centre frequency propagates with velocity v_p, by using this kind of ABC the wave is not completely absorbed and there will be some reflection depending on the frequency bandwidth.

In the next chapter (section 5.7) this ABC will be used in both ends of a rect-

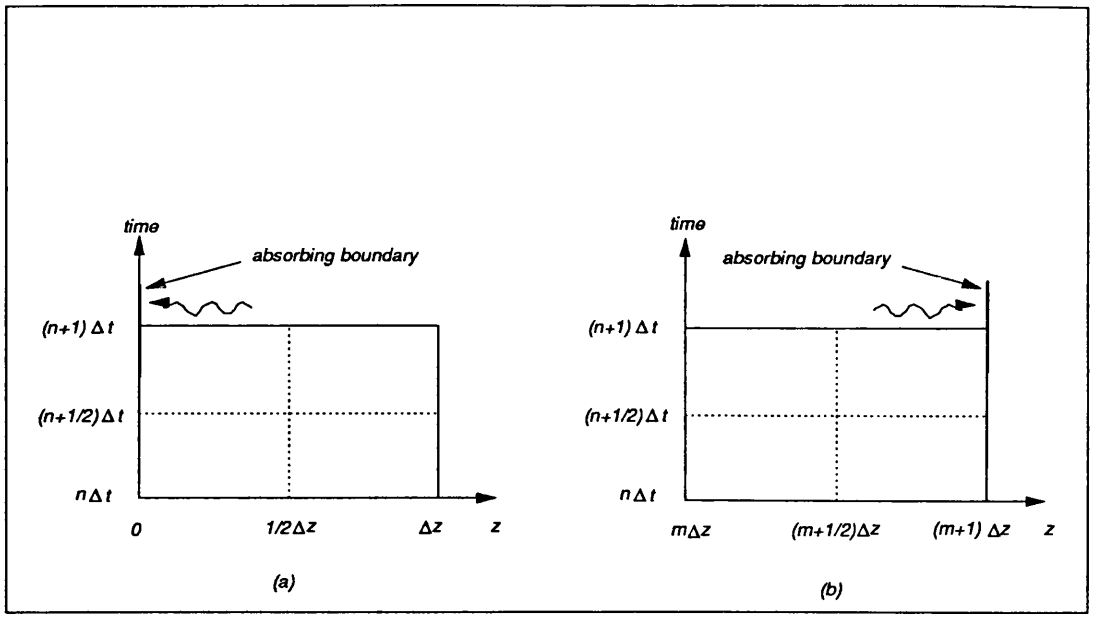

Figure 4.2: Grid mesh for discretisation 1st order Mur's ABC for boundaries located at a)$z = 0$ b)$z = (m+1)\Delta z$.

angular waveguide for TE_{10} mode and some examples of its characteristics with frequency are presented and compared with the PML ABC.

4.4 The PML Technique in FDTD

Recently, Berenger has published a novel ABC for FDTD meshes in two dimensions which he called Perfectly Matched Layer (PML)[63]. In this technique, the boundaries for truncation of the numerical computation domain which is vacuum free space, are surrounded by artificial media which are lossy electric and the magnetic conductivities (σ, σ^* respectively) and are backed by metal PEC (Perfect Electric Conductor) walls. Equation 4.18 designate magnetic conductivity (σ^*) [63]:

$$\mu_0 \frac{\partial \vec{H}}{\partial t} + \nabla \times \vec{E} + \sigma^* \vec{H} = 0 \tag{4.18}$$

For the 3-D problem, in each medium electric and magnetic components split

into two nonphysical subcomponents. The PML is capable of absorbing a plane wave reaching any interface of the media and the vacuum. This is seen for any incident angle and frequency provided that the ratio of the necessary electric and magnetic conductivities of the medium subscribed to the axis normal to the interface are inversely equal to the impedance of free space. It means that:

$$\frac{\sigma_i}{\epsilon_0} = \frac{\sigma_i^*}{\mu_0} \tag{4.19}$$

where i can be x, y or z. This condition is analogous to the matching impedance condition in a classical matched layer and also ensures that the impedance equals that of vacuum. When a medium is the overlap of two (or three) media, it has two (or three) sets of conductivities of the relevant overlapped media.

In the absorbing media of the PML technique, the six components of the electromagnetic field are split into twelve subcomponents E_{xy}, E_{xz}, E_{yx}, E_{yz}, etc, and such that $E_x = E_{xy} + E_{xz}$, $E_y = E_{yx} + E_{yz}$, $E_z = E_{zx} + E_{zy}$, etc.

Since each variable is now represented by two new variables, a second set of equations is needed to define the new variables. This second equation is obtained from Maxwell's curl equation-one example of which is as follows. Consider one component of Eq. 4.18:

$$\frac{\partial}{\partial y}E_z - \frac{\partial}{\partial z}E_y = -\mu_0\frac{\partial}{\partial t}H_x - \sigma^* H_x \tag{4.20}$$

Substituting each field component by its two corresponding subcomponents, obtain:

$$\frac{\partial}{\partial y}(E_{zx} + E_{zy}) - \frac{\partial}{\partial z}(E_{yx} + E_{yz}) = -\mu_0\frac{\partial}{\partial t}H_{xy} - \mu_0\frac{\partial}{\partial t}H_{xz} - \overset{*}{\sigma}H_{xy} - \overset{*}{\sigma}H_{xz}$$

The second set of defining equations are obtained by enforcing:

$$\frac{\partial}{\partial y}(E_{zx} + E_{zy}) = -\mu_0 \frac{\partial}{\partial t} H_{xy} - \sigma_y^* H_{xy} \tag{4.21}$$

$$\frac{\partial}{\partial z}(E_{yx} + E_{yz}) = \mu_0 \frac{\partial}{\partial t} H_{xz} + \sigma_z^* H_{xz} \tag{4.22}$$

where, note, σ^* is σ_y^* in the equation containing derivations with respect to y (Eq. 4.21), and similarly σ_z^* is used in Eq. 4.22.

By the same procedure the other algebraic Maxwell's equations will be:

$$\frac{\partial}{\partial z}(E_{xy} + E_{xz}) = -\mu_0 \frac{\partial}{\partial t} H_{yz} - \sigma_z^* H_{yz} \tag{4.23}$$

$$\frac{\partial}{\partial x}(E_{zx} + E_{zy}) = \mu_0 \frac{\partial}{\partial t} H_{yx} + \sigma_x^* H_{yx} \tag{4.24}$$

$$\frac{\partial}{\partial x}(E_{yx} + E_{yz}) = -\mu_0 \frac{\partial}{\partial t} H_{zx} - \sigma_x^* H_{zx} \tag{4.25}$$

$$\frac{\partial}{\partial y}(E_{xy} + E_{xz}) = \mu_0 \frac{\partial}{\partial t} H_{zy} + \sigma_y^* H_{zy} \tag{4.26}$$

$$\frac{\partial}{\partial y}(H_{zx} + H_{zy}) = \epsilon_0 \frac{\partial}{\partial t} E_{xy} + \sigma_y E_{xy} \tag{4.27}$$

$$\frac{\partial}{\partial z}(H_{yx} + H_{yz}) = -\epsilon_0 \frac{\partial}{\partial t} E_{xz} - \sigma_z E_{xz} \tag{4.28}$$

$$\frac{\partial}{\partial z}(H_{xy} + H_{xz}) = \epsilon_0 \frac{\partial}{\partial t} E_{yz} + \sigma_z E_{yz} \tag{4.29}$$

$$\frac{\partial}{\partial x}(H_{zx} + E_{zy}) = -\epsilon_0 \frac{\partial}{\partial t} E_{yx} - \sigma_x E_{yx} \tag{4.30}$$

$$\frac{\partial}{\partial x}(H_{yx} + H_{yz}) = \epsilon_0 \frac{\partial}{\partial t} E_{zx} + \sigma_x E_{zx} \tag{4.31}$$

$$\frac{\partial}{\partial y}(H_{xy} + H_{xz}) = -\epsilon_0 \frac{\partial}{\partial t} E_{zy} - \sigma_y E_{zy} \tag{4.32}$$

where the above conductivities must satisfy Eq. 4.19, that means $\frac{\sigma_x}{\epsilon_0} = \frac{\sigma_x^*}{\mu_0}$, $\frac{\sigma_y}{\epsilon_0} = \frac{\sigma_y^*}{\mu_0}$, and $\frac{\sigma_z}{\epsilon_0} = \frac{\sigma_z^*}{\mu_0}$.

For a better understanding, first consider a piece of a PML media in Fig. 4.3 of two or three dimensions. This PML medium allows an absorbing layer to be built in such a way that there is no reflection from the vacuum-layer interface. In other words, the reflection coefficient of a plane wave striking the vaccum-layer interface can be equal to zero at any frequency and any incident angle. Such an achievement is obtained by choosing an appropriate set of conductivities in the absorbing layer. For instance in the 2-D case [63], and at an interface normal to the x axis (Fig. 4.3), if $\sigma_y = \sigma_y^* = 0$ and if σ_x and σ_x^* satisfy the condition $\frac{\sigma_x}{\epsilon_0} = \frac{\sigma_x^*}{\mu_0}$, the reflection coefficient of a plane wave is zero, at any frequency and any incidence angle. Similarly, in the 3-D case such a lack of reflection is obtained using the PML $(\sigma_x, \sigma_x^*, 0, 0, 0, 0)$ medium in which σ_x and σ_x^* satisfy condition Eq. 4.19.

Secondly consider the 2-D cases, the previous twelve Maxwell's equations reduce to a set of four equations given in [63]. Only one component is split into two subcomponents, either the magnetic component in the TE case or the electric component in the TM case. Fig. 4.4 shows the general frame of the computational volume for the PML technique in this case. There is a source of outgoing waves, it is surrounded by an absorbing layer which is an aggregate of PML media that is finally terminated by a PEC. Both left and right side layers are matched PML

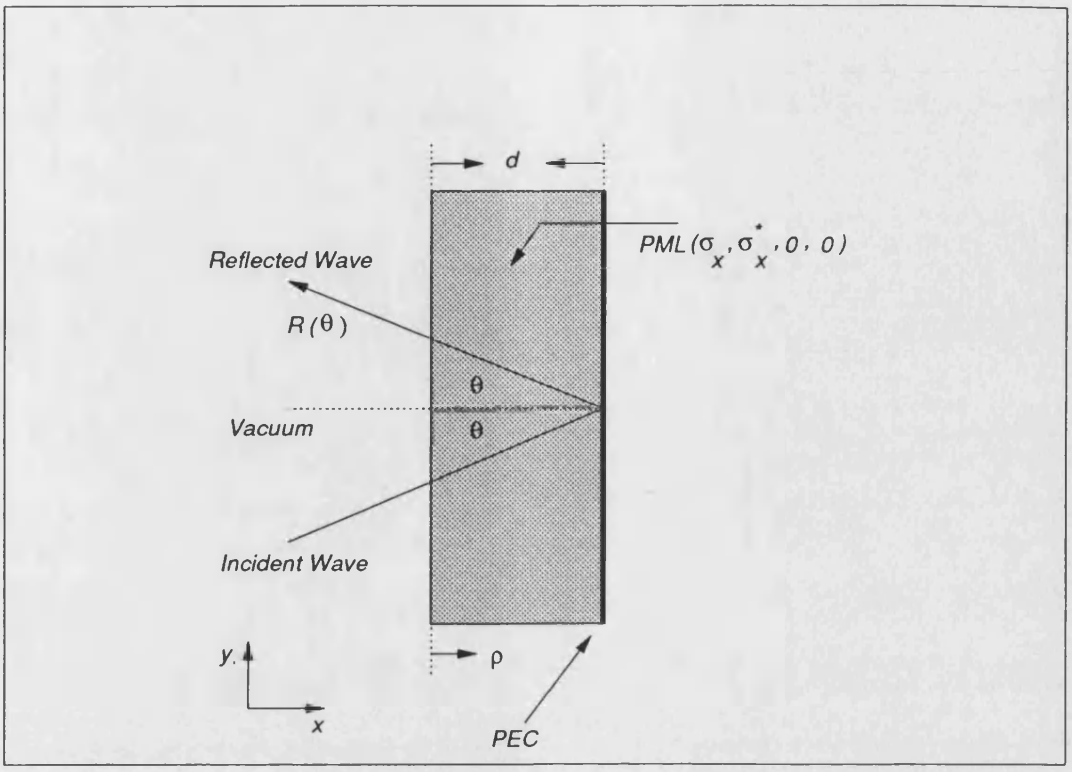

Figure 4.3: PML layer with interface normal to x.

$(\sigma_x,\ \sigma_x^*,\ 0,\ 0)$, so if the wave is incident to interface AB or CD, theoretically there is no reflection. Similarly the lower and upper side layers are matched PML $(0,\ 0,\ \sigma_y,\ \sigma_y^*)$ so that the outgoing wave can propagate without reflection if incident on the interface CB or DA. At the four corners of the domain, where there is an overlap of two PMLs, all four losses are present (σ_x, σ_x^*, σ_y, and σ_y^*) and set equal to those of the adjacent PMLs.

Based on [63], inside the layer (Fig 4.3) at a distance ρ from any interface, the magnitude of an outgoing plane wave is:

$$\psi(\rho) = \psi(0)e^{-(\frac{\sigma\cos\theta}{\epsilon_0 c})\rho} \tag{4.33}$$

where c is the velocity of light in the computation volume, θ is the angle between the incident wave and the interface. Despite the absence of reflection at the

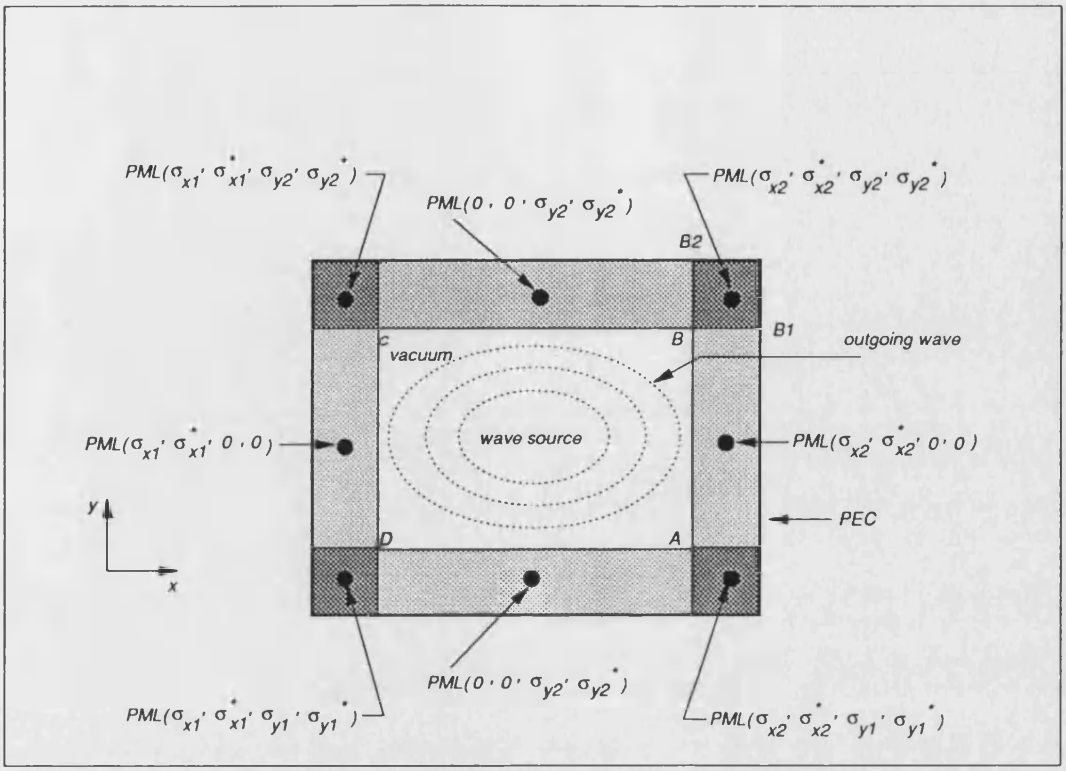

Figure 4.4: PML layers for 2-D configuration.

vacuum-layer interface, the absorbing layer is not without reflection since the outgoing waves are from the perfectly conducting conditions set on its outer boundary, so, they can return into the vacuum. The entering wave, after striking the PEC, reflect back in to the vaccum and the reflection coefficient will be:

$$R(\theta) = e^{-2(\frac{\sigma cos\theta}{\epsilon_0 c})d} \tag{4.34}$$

where d is the depth of the PML.

Additionally, sharp variation of the conductivity can create numerical reflections so the reflection can be reduced by varying the conductivities spatially:

$$R(\theta) = e^{-2(\frac{cos\theta}{\epsilon_0 c})\int_0^d \sigma(\rho)d\rho} \tag{4.35}$$

Berenger used his numerical computations based on the variation of conductivity as below:

$$\sigma(\rho) = \sigma_m(\frac{\rho}{d})^q \tag{4.36}$$

where the conductivity varies from zero at the vacuum-layer interface to a value σ_m at the outer side of the layer along the normal to each axis. q is the order of the polynomial (q=1 for linear, q=2 for parabolic) and therefore:

$$R(\theta) = e^{-\frac{2\sigma_m d}{(q+1)\epsilon_0 c}cos\theta} \tag{4.37}$$

and then:

$$\sigma_m = -\ln[R(0)]\frac{q+1}{2}\frac{\epsilon_0 c}{d} \tag{4.38}$$

where $R(0)$ is the reflection coefficient for θ=0.

For the whole computation six normal discretised Maxwell's equations in vacuum (Eqs 3.3-3.8) are used. For discretisation of the twelve Eqs. 4.21-4.32 it is considered that the exponential decay of the propagating wave in certain lossy media is so rapid that the standard Yee time stepping algorithm cannot be used. By considering solution of the first order differential equation, a discretised form of the twelve Eqs. 4.21-4.32 can be obtained. For instance consider Eq. 4.21 and assume the right hand side is equal to -A:

$$\frac{\partial}{\partial y}(E_{zx} + E_{zy}) = -\mu_0\frac{\partial}{\partial t'}H_{xy} - \sigma_y^* H_{xy} = -A \tag{4.39}$$

therefore:

$$\mu_0\frac{\partial}{\partial t'}H_{xy}(i,j,k) + \sigma_y^* H_{xy}(i,j,k) = A \tag{4.40}$$

The transient response of this equation is:

$$H_{xytr}(i,j,k) = Ce^{-\frac{\sigma_y^*}{\mu_0}t'} \tag{4.41}$$

and the particular response is:

$$H_{xypart}(i,j,k) = B = constant \tag{4.42}$$

B must satisfy Eq. 4.40. Therefore:

$B = \frac{A}{\sigma_y^*}$

and the total response is:

$$H_{xy}(i,j,k) = Ce^{-\frac{\sigma_y^*}{\mu_0}t'} + \frac{A}{\sigma_y^*} \tag{4.43}$$

At t'=0 or $t = (n - \frac{1}{2})\Delta t$:

$$H_{xy}(i,j,k) = H_{xy}^{n-\frac{1}{2}}(i,j,k) = C + \frac{A}{\sigma^*} \tag{4.44}$$

therefore $C = H_{xy}^{n-\frac{1}{2}}(i,j,k) - \frac{A}{\sigma^*}$

At $t' = \Delta t$ or $t = (n + \frac{1}{2})\Delta t$

$$H_{xy}(i,j,k) = H_{xy}^{n+\frac{1}{2}}(i,j,k) = Ce^{-\frac{\sigma^*}{\mu_0}\Delta t} + \frac{A}{\sigma_y^*} \tag{4.45}$$

By inserting the above value of C into Eq. 4.45:

$$H_{xy}^{n+\frac{1}{2}}(i,j,k) = e^{-\frac{\sigma_y^*}{\mu_0}\Delta t}H_{xy}^{n-\frac{1}{2}}(i,j,k) - \frac{A}{\sigma_y^*}(e^{-\frac{\sigma_y^*}{\mu_0}\Delta t} - 1) \tag{4.46}$$

Eq. 4.39 is a differentiation with respect to y. Therefore:

$$A = \left[E_{zx}^n(i,j+1,k) + E_{zy}^n(i,j+1,k) - E_{zx}^n(i,j,k) - E_{zy}^n(i,j,k)\right]/\Delta y \tag{4.47}$$

Finally the discretised form of the Eq. 4.19 is:

$$\begin{aligned} H_{xy}^{n+\frac{1}{2}}(i,j,k) \quad &= e^{-\frac{\sigma_y^*}{\mu_0}\Delta t}H_{xy}^{n-\frac{1}{2}}(i,j,k) - \frac{e^{-\frac{\sigma_y^*}{\mu_0}\Delta t} - 1}{\sigma_y^*\Delta y} \times \\ &\left[E_{zx}^n(i,j+1,k) + E_{zy}^n(i,j+1,k) - E_{zx}^n(i,j,k) - E_{zy}^n(i,j,k)\right] \end{aligned} \tag{4.48}$$

Following the same procedure the discretised form of Eqs. 4.22-4.32 are:

$$H_{xz}^{n+\frac{1}{2}}(i,j,k) = e^{-\frac{\sigma_z^*}{\mu_0}\Delta t} H_{xz}^{n-\frac{1}{2}}(i,j,k) - \frac{e^{-\frac{\sigma_z^*}{\mu_0}\Delta t} - 1}{\sigma_z^* \Delta z} \times \left[E_{yx}^n(i,j,k+1) + E_{yz}^n(i,j,k+1) - E_{yx}^n(i,j,k) - E_{yz}^n(i,j,k)\right] \tag{4.49}$$

$$H_{yz}^{n+\frac{1}{2}}(i,j,k) = e^{-\frac{\sigma_z^*}{\mu_0}\Delta t} H_{yz}^{n-\frac{1}{2}}(i,j,k) + \frac{e^{-\frac{\sigma_z^*}{\mu_0}\Delta t} - 1}{\sigma_z^* \Delta z} \times \left[E_{xy}^n(i,j,k+1) + E_{xz}^n(i,j,k+1) - E_{xy}^n(i,j,k) - E_{xz}^n(i,j,k)\right] \tag{4.50}$$

$$H_{yx}^{n+\frac{1}{2}}(i,j,k) = e^{-\frac{\sigma_x^*}{\mu_0}\Delta t} H_{yx}^{n-\frac{1}{2}}(i,j,k) - \frac{e^{-\frac{\sigma_x^*}{\mu_0}\Delta t} - 1}{\sigma_x^* \Delta x} \times \left[E_{zx}^n(i+1,j,k) + E_{zy}^n(i+1,j,k) - E_{zx}^n(i,j,k) - E_{zy}^n(i,j,k)\right] \tag{4.51}$$

$$H_{zx}^{n+\frac{1}{2}}(i,j,k) = e^{-\frac{\sigma_x^*}{\mu_0}\Delta t} H_{zx}^{n-\frac{1}{2}}(i,j,k) + \frac{e^{-\frac{\sigma_x^*}{\mu_0}\Delta t} - 1}{\sigma_x^* \Delta x} \times \left[E_{yx}^n(i+1,j,k) + E_{yz}^n(i+1,j,k) - E_{yx}^n(i,j,k) - E_{yz}^n(i,j,k)\right] \tag{4.52}$$

$$H_{zy}^{n+\frac{1}{2}}(i,j,k) = e^{-\frac{\sigma_y^*}{\mu_0}\Delta t} H_{zy}^{n-\frac{1}{2}}(i,j,k) - \frac{e^{-\frac{\sigma_y^*}{\mu_0}\Delta t} - 1}{\sigma_y^* \Delta y} \times \left[E_{xy}^n(i,j+1,k) + E_{xz}^n(i,j+1,k) - E_{xy}^n(i,j,k) - E_{xz}^n(i,j,k)\right] \tag{4.53}$$

$$E_{xy}^{n+1}(i,j,k) = e^{-\frac{\sigma_y}{\epsilon_0}\Delta t} E_{xy}^n(i,j,k) - \frac{e^{-\frac{\sigma_y}{\epsilon_0}\Delta t} - 1}{\sigma_y \Delta y} \times \left[H_{zx}^{n+\frac{1}{2}}(i,j,k) + H_{zy}^{n+\frac{1}{2}}(i,j,k) - H_{zx}^{n+\frac{1}{2}}(i,j-1,k) - H_{zy}^{n+\frac{1}{2}}(i,j-1,k)\right] \tag{4.54}$$

$$E_{xz}^{n+1}(i,j,k) = e^{-\frac{\sigma_z}{\epsilon_0}\Delta t} E_{xz}^n(i,j,k) + \frac{e^{-\frac{\sigma_z}{\epsilon_0}\Delta t} - 1}{\sigma_z \Delta z} \times \left[H_{yx}^{n+\frac{1}{2}}(i,j,k) + H_{yz}^{n+\frac{1}{2}}(i,j,k) - H_{yx}^{n+\frac{1}{2}}(i,j,k-1) - H_{yz}^{n+\frac{1}{2}}(i,j,k-1)\right] \tag{4.55}$$

$$E_{yz}^{n+1}(i,j,k) = e^{-\frac{\sigma_z}{\epsilon_0}\Delta t} E_{yz}^n(i,j,k) - \frac{e^{-\frac{\sigma_z}{\epsilon_0}\Delta t} - 1}{\sigma_z \Delta z} \times \left[H_{xy}^{n+\frac{1}{2}}(i,j,k) + H_{xz}^{n+\frac{1}{2}}(i,j,k) - H_{xy}^{n+\frac{1}{2}}(i,j,k-1) - H_{xz}^{n+\frac{1}{2}}(i,j,k-1)\right] \tag{4.56}$$

$$E_{yx}^{n+1}(i,j,k) = e^{-\frac{\sigma_x}{\epsilon_0}\Delta t} E_{yx}^{n}(i,j,k) + \frac{e^{-\frac{\sigma_x}{\epsilon_0}\Delta t} - 1}{\sigma_x \Delta x} \times \left[H_{zx}^{n+\frac{1}{2}}(i,j,k) + E_{zy}^{n+\frac{1}{2}}(i,j,k) - H_{zx}^{n+\frac{1}{2}}(i-1,j,k) - H_{zy}^{n+\frac{1}{2}}(i-1,j,k) \right] \tag{4.57}$$

$$E_{zx}^{n+1}(i,j,k) = e^{-\frac{\sigma_x}{\epsilon_0}\Delta t} E_{zx}^{n}(i,j,k) - \frac{e^{-\frac{\sigma_x}{\epsilon_0}\Delta t} - 1}{\sigma_x \Delta x} \times \left[H_{yx}^{n+\frac{1}{2}}(i,j,k) + H_{yz}^{n+\frac{1}{2}}(i,j,k) - H_{yx}^{n+\frac{1}{2}}(i-1,j,k) - H_{yz}^{n+\frac{1}{2}}(i-1,j,k) \right] \tag{4.58}$$

$$E_{zy}^{n+\frac{1}{2}}(i,j,k) = e^{-\frac{\sigma_y}{\epsilon_0}\Delta t} E_{zy}^{n}(i,j,k) + \frac{e^{-\frac{\sigma_y}{\epsilon_0}\Delta t} - 1}{\sigma_y \Delta y} \times \left[H_{xy}^{n+\frac{1}{2}}(i,j,k) + H_{xz}^{n+\frac{1}{2}}(i,j,k) - H_{xy}^{n+\frac{1}{2}}(i,j-1,k) - H_{xz}^{n+\frac{1}{2}}(i,j-1,k) \right] \tag{4.59}$$

In implementation of the PML technique at the interface of the vacuum and the PML medium, one field of any of the above formulations is in the PML medium but because of the space offset in Yee's mesh the other one may be in vacuum. If a field is in the PML medium, its subcomponents must appear in the above formulations, but if it is in the vacuum, the main form must be used in the formulation. For example in Eq. 4.48, if E_z is located in vacuum, inside the bracket $[E_z^n(i,j+1,k) - E_z^n(i,j,k)]$ must be used.

For practical implementation, q, σ_m and d (or nl, the number of layers in each medium) are needed. Up to now, there is no exact formulation for optimization of the PML parameters, however Berenger and many researchers have used q=2. In the next chapter (Section 5.7) this kind of ABC will be used at both ends of a rectangular waveguide where the choice of the essential parameters q, σ_m, and nl is discussed. Some examples of its characteristics with frequency are also compared with the 1st order Mur's ABC.

At first glance it can be concluded that implementation of the PML ABC is more complicated than the Mur's ABC. Additionally for having an ABC at one end of the line, an extra cell is needed for 1st order Mur's ABC but an adequate number of cells of the computational mesh is needed for the PML. Therefore the PML ABC needs more CPU time and computer memory than the Mur's ABC.

Chapter 5

Implementation of the FDTD Technique in Rectangular Waveguide

5.1 Outline

All the defining characteristics of metal rectangular waveguide are known analytically [66]. This is one of the reasons that in this chapter the FDTD technique is implemented in this guide for its dominant mode (TE_{10}) to give an opportunity to test the analysis. Also through the Fourier transform, the main field components of the TE_{10} mode as a function of distance for the first time step of running the FDTD analysis, as is detailed in Section 5.4, are prepared as a means of excitation. This method of excitation leads to the excitation of the IDG in the next chapter. In this chapter, at both ends of the rectangular waveguide, 1st order Mur and PML ABCs are used and compared with each other. From this the most efficient one for future IDG investigations is chosen.

5.2 Dominant Mode in Rectangular Waveguide (TE_{10})

Figure 5.1a shows the coordinate system for rectangular waveguide with cross sectional dimensions a and b. Fig. 5.1b shows a line diagram indicating the cut-off frequencies of several of the lowest order modes for two cases $\frac{b}{a} = 1$, and $\frac{b}{a} = \frac{1}{2}$ referred to the cut-off frequency of the dominant TE_{10} mode. To have a single mode of propagation, by the excitation as detailed in Section 5.4, the dominant mode TE_{10} is chosen. To have maximum frequency bandwidth for this single mode and to prevent degeneracy due to mode TE_{01} , the dimension a=2b is chosen. Cut-off frequency, f_c, for a particular mode is that frequency below which the electromagnetic wave associated with that mode can not propagate in the waveguide.

First consider a TEM wave with frequency f propagating in a homogenous medium which is the same as that filling the waveguide ($\epsilon = \epsilon_r\epsilon_0$ and $\mu = \mu_0$), so v velocity and λ wavelength of this wave are:

$$v = \frac{1}{\sqrt{\mu\epsilon}} = \frac{c}{\sqrt{\epsilon_r}} \tag{5.1}$$

$$\lambda = \frac{v}{f} \tag{5.2}$$

and η the intrinsic impedance of the area in which this wave propagates is:

$$\eta = \sqrt{\frac{\mu}{\epsilon}} = \frac{120\pi}{\sqrt{\epsilon_r}} \tag{5.3}$$

Now consider a TE_{10} mode propagating with frequency f in a rectangular wave guide, some necessary relations are [66]:

wavelength corresponding to cut-off frequency:

$$\lambda_c = 2a \tag{5.4}$$

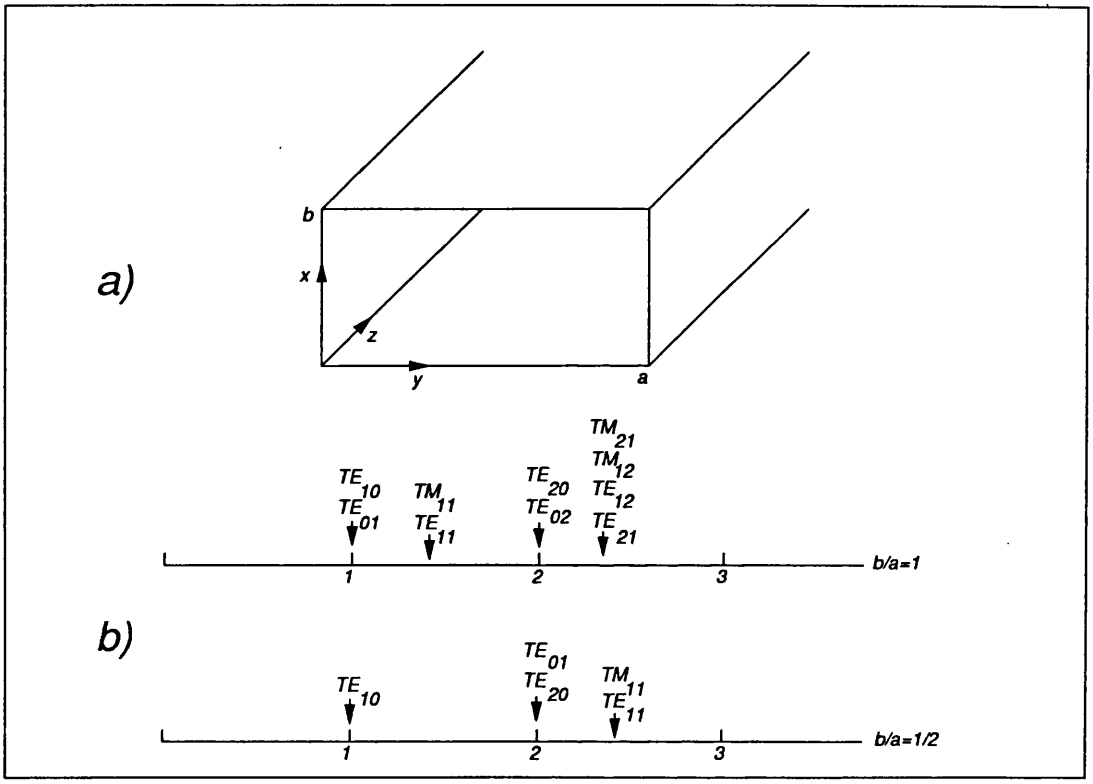

Figure 5.1: a) coordinate system for rectangular waveguide b) line diagram indicating some cut-off frequencies referred to the cut-off frequency of the TE_{01} mode.

cut-off frequency:

$$f_c = \frac{v}{\lambda_c} = \frac{1}{2a\sqrt{\mu\epsilon}} \tag{5.5}$$

phase constant:

$$\beta = \sqrt{\omega^2\mu\epsilon - (\frac{\pi}{a})^2} = \frac{\omega}{v}\sqrt{1 - (\frac{f_c}{f})^2} \tag{5.6}$$

phase velocity:

$$v_p = \frac{\omega}{\beta} = \frac{v}{\sqrt{1 - (\frac{v}{2af})^2}} \tag{5.7}$$

guide modal wavelength:

$$\lambda_g = \frac{v_p}{f} = \frac{2\pi}{\beta} = \frac{v}{\sqrt{f^2 - (\frac{v}{2a})^2}} \tag{5.8}$$

For the TE_{10} mode there are only three field components (E_x, H_y, and H_z) and the others are zero. E_x is [66]:

$$E_x = E_0 sin\frac{\pi y}{a} \tag{5.9}$$

Bearing in mind that the propagation factor is $e^{j(\omega t - \beta z)}$, therefore $\frac{\partial}{\partial z} = -j\beta$. The result of expanding Maxwell's equation $\nabla \times \vec{E} = -j\omega\mu\vec{H}$ is:

$$\nabla \times \vec{E} = \vec{a}_x(0) - \vec{a}_y(j\beta E_x) + \vec{a}_z(-\frac{\partial}{\partial y}E_x) = j\omega\mu(H_x\vec{a}_x + H_y\vec{a}_y + H_z\vec{a}_z) \tag{5.10}$$

One of the results of comparing two sides of the above equation is:

$H_y = \frac{\beta E_x}{\omega\mu}$

The wave impedance Z_w, for the TE_{10} mode is defined as :

$$Z_w = \frac{E_x}{H_y} = \frac{\omega\mu}{\beta} = \frac{\eta}{\sqrt{1 - (\frac{v}{2af})^2}} \tag{5.11}$$

By using Z_w and Eq. 5.9 :

$$H_y = \frac{E_0}{Z_w} sin\frac{\pi y}{a} \tag{5.12}$$

Another result from comparing the two sides of the Eq. 5.10 is: $-\frac{\partial}{\partial y}E_x = -j\omega\mu H_z$, after some algebraic operations :

$$H_z = \frac{-j\lambda}{2a\eta}E_0 cos\frac{\pi y}{a} \tag{5.13}$$

5.3 The FDTD Code Implementation

The FDTD analysis of the mode in the waveguide is carried out by applying a signal of the form given in Eq. 3.24 at the input of the waveguide where the Gaussian envelope may be viewed as a modulation of the carrier frequency, f_o, which in this analysis is 11.25 GHz with a frequency bandwidth of 4 GHz for the Gaussian pulse. Inside the guide is air ($\mu_r = \epsilon_r$=1).

Figure 5.2 shows the position of the Yee's cells in the computation domain of the guide. Integer and an even number of cells for both directions of x (i) and y (j) are chosen. $n2$ is the number of cells in the y direction and $n1$ is the number of cells in the x direction. An integer number of cells $k = n3$ is used along the z direction. The value of $n3$ depending on the chosen length of the line.

For simplicity all space cell sizes are determined equally ($\Delta x = \Delta y = \Delta z = \delta$). Based on what was described in Section 3.3 $\delta \leq \frac{\lambda}{10}$, where λ is the smallest wavelength of the modulated pulse. After that the relation $\Delta t = k_s\frac{\delta}{v}$ is used to determined time step size Δt where k_s is the stability factor.

On the surface of the perfect metal, tangential electric fields and normal magnetic fields are zero ($E_t = H_n$=0). The first cell in the corner $i = j = k = 0$ is placed such that the planes of the cell adjacent to the metal walls have E_t and H_n components. Therefore when running the analysis, calculation of these components for $i = j = 0$, $i = n1$, and $j = n2$ are not needed. If the 1st order Mur's ABC is used at both ends of the guide, the tangential electric fields at k=0 and k=$n3$ are calculated by the ABC. If the PML's ABC is used, there will be

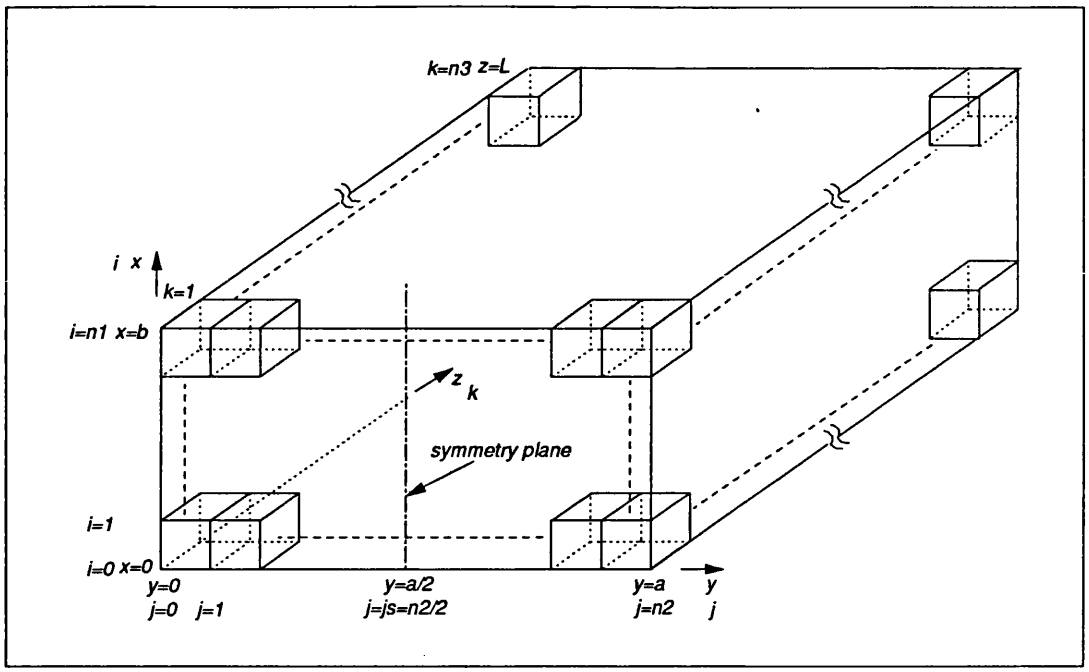

Figure 5.2: Position of the Yee's cells in the computation domain of the guide.

equal number of lossy layers (nl) at both ends of the guide. In this case k starts from $-nl$ to $n3+nl$ and at these two planes there are PECs, therefore tangential electric and normal magnetic fields on these planes need not be calculated.

5.4 Excitation

For running the analysis, regarding Eqs. 3.11-3.16, for the first time step (n=0) the value of $H_y^{-\frac{1}{2}}(i,j,k)$, $H_z^{-\frac{1}{2}}(i,j,k)$, $E_x^0(i,j,k)$, and $E_x^0(i,j,k+1)$ are needed. These components are produced as a function of distance. In other words, at n=0 the values of these components spread along the transmission line as the initial values.

In this method, first $E_x(f)$ is analytically produced from $E_x(y,t)$ which is shown in Fig. 5.3.

$$E_x(y,t) = A_0 e^{-(\frac{t-t_f}{y_p})^2} e^{j2\pi f_o t} sin\frac{\pi y}{a} \tag{5.14}$$

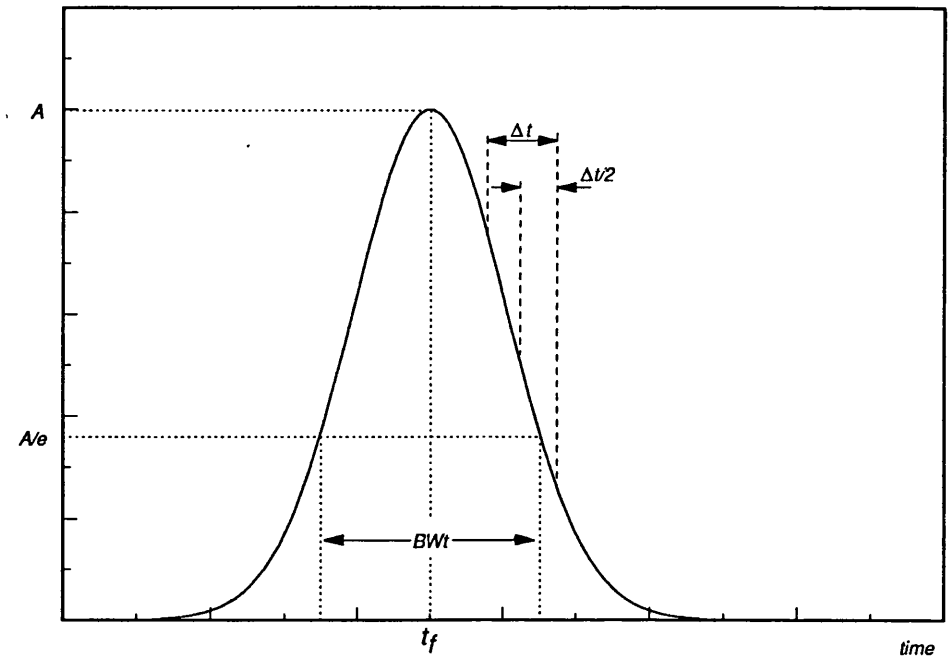

Figure 5.3: $E_x(t)$ as the function of time and definition of BW_t.

The spatial form $sin\frac{\pi y}{a}$ is chosen to enforce only the fundamental mode excitation.

The discretised form of $E_x(y,t)$ is:

$$E_x(y,n\Delta t) = A_0 e^{-(\frac{n\Delta t - t_p\Delta t}{y n\Delta t})^2} e^{j2\pi f_o n\Delta t} sin\frac{\pi y}{a} \tag{5.15}$$

where t_f is offset against time ($t_f = t_p\Delta t$). To centre the peak of the pulse at middle of the line t_p must be $\frac{n3}{2}$.

By considering a function $f(t)$ and its Fourier transform $F(f)$ as below:

$$f(t) = e^{-\alpha t^2} \quad \Leftrightarrow \quad F(f) = \sqrt{\frac{\pi}{\alpha}} e^{-\frac{\pi^2 f^2}{\alpha}} \tag{5.16}$$

by:

$$g_1(t) = f(t - t_f) \quad \Leftrightarrow \quad G_1(f) = F(f) e^{-j2\pi f t_f} \tag{5.17}$$

$$g_2(t) = f(t) e^{j2\pi f_o t} \quad \Leftrightarrow \quad G_2(f) = F(f - f_o) \tag{5.18}$$

the Fourier transform of $E_x(y,t)$ is:

$$E_x(y,f) = A_0\sqrt{\pi}y_p e^{-\pi^2 y_p^2(f-f_o)^2} e^{-j2\pi t_f(f-f_o)} sin\frac{\pi y}{a} \tag{5.19}$$

and its magnitude is:

$$|E_x(y,f)| = A_0\sqrt{\pi}y_p e^{-\pi^2 y_p^2(f-f_o)^2} sin\frac{\pi y}{a} \tag{5.20}$$

With the frequency discretised as:

$$f = ndf \tag{5.21}$$

Thus:

$$|E_x(y,ndf)| = A_0\sqrt{\pi}y_p e^{-\pi^2 y_p^2(ndf-f_o)^2} sin\frac{\pi y}{a} \tag{5.22}$$

Now by Eqs. 5.11, 5.12, and 5.13 discretised Fourier transforms $H_y(y,ndf)$ and $H_z(y,ndf)$ are produced from $E_x(y,ndf)$. At this stage the factors $sin\frac{\pi y}{a}$ and $cos\frac{\pi y}{a}$ are not considered but they will be considered finally in the FDTD code.

Referring to Eqs. 3.11-3.16 and Yee's mesh in Fig. 3.1, two kinds of offsets must be considered. First an offset in space for H_y which is $\frac{\delta}{2}$ leading in $+z$ direction in respet to E_x (the front plane of the Yee's mesh along with E_x and E_z are located at k=0 plane). This offset is imposed by a multiplication of $H_y(f)$ by $e^{-\gamma\frac{\delta}{2}}$. This factor for $E_x^0(i,j,k+1)$ is $e^{-\gamma\delta}$, where γ is propagation constant whose discretised form is:

$$\gamma = \sqrt{\frac{\pi^2}{a} - (2\pi ndf)^2\mu\epsilon} \tag{5.23}$$

For propagating frequencies and lossless condition $\gamma = j\beta$.

The second offset is a half time step ($\frac{\Delta t}{2}$) for H_y and H_z which are lagging in comparison with E_x. To cause this offset for the above magnetic fields, double sample points of $E_x(t)$ are picked up with time spacing $\frac{\Delta t}{2}$; as a result double points for all three components are supplied when they are produced by the

output of the inverse Fourier transform against distance. Now the offset in time causes a similar offset in space ($\frac{\delta}{2}$). Finally in the FDTD code if the nominated index for the first entry points of the component is one, at the first time step ($n = 0$) even integer indices of the magnetic fields and odd indices of the electric fields are picked respectively. To change the output of the inverse Fourier transform from a function of time to a function of distance, a change of variable of Δt which is:

$$\Delta t = \frac{\Delta z}{2v_p} \tag{5.24}$$

must take place, where $\Delta z = \delta$. The factor 2 in the denominator of Eq. 5.24 is because half time step offset is required.

With the total number of points=tnp, the frequency spacing which results in a $\frac{\Delta t}{2}$ in time spacing is:

$$df = \frac{1}{tnp\Delta t} \tag{5.25}$$

Bandwidth (BW) is defined as the duration of two points for any time, frequency, or space Gaussian pulses which have same magnitude equal $\frac{1}{e}$ peak of the relevant pulses. Therefore based on this definition the relations between BW_t, BW_f (as the bandwidth relevant to time and frequency respectively) can be calculated by using Eq. 5.16:

$$BW_t.BW_f = \frac{4}{\pi} \tag{5.26}$$

To calculate the relation between BW_t and BW_s (bandwidth relevant to space), consider that the Gaussian pulse (envelope of the sine wave) propagates with group velocity (v_g) which can be obtained from Eq. 5.26 [66]:

$$v_g = \frac{v^2}{v_p} \tag{5.27}$$

then:

$$BW_s = v_g.BW_t \tag{5.28}$$

The final point in this relation is that the outputs of the inverse Fourier transform have bandwidth relevant to space equal to:

$$BW'_s = v_p BW'_t = v_p \frac{4}{\pi BW'_f}$$

which is greater than the desirable BW_s by the factor of $\frac{v_p}{v_g}$. (the parameters relevant to the inverse Fourier transform are shown with a prime.)

For compensation, the factor c_f is defined as:

$$c_f = \frac{v_p}{v_g} \tag{5.29}$$

and the input frequency bandwidth of inverse Fourier transform instead of BW_f, will be $BW'_f = c_f BW_f$. By this compensation the outputs of the FDTD analysis have a desirable frequency bandwidth equal to BW_f.

By this method of excitation, which has not been seen in the literature, ideally the wave propagates only in one direction of the line for example $+z$ and there is no back projection towards the $-z$ direction. Because both E and H components are appeared in the excitation. Consequently there is no reflection from the ABC located at $z = 0$. If the sign of one of the components is changed, the direction of propagation will changed.

5.5 Boundary conditions

Boundary conditions can be implemented by considering Yee's mesh (Fig. 3.1). For the perfect metal walls which exist at j=0 and $n2$ these condition are E_x , E_z, and H_y equal to zero (Fig 5.4) and for the perfect metal walls which exist at i=0 and i=$n1$ E_y , E_z, and H_x (Fig. 5.5) are also zero. Therefore when the value of these fields are known the FDTD code does not calculate them.

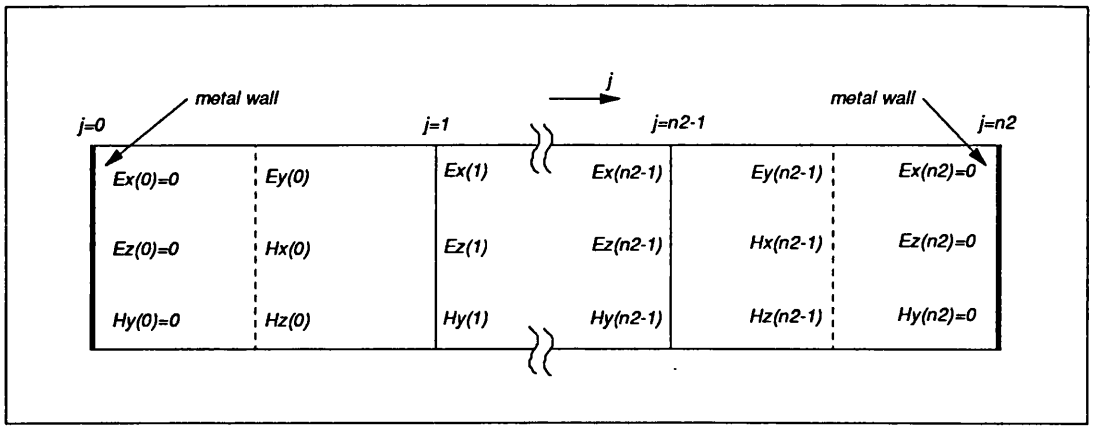

Figure 5.4: A part of the Yee's mesh along the y direction. Normal magnetic field and tangential electric fields at j=0 and j=$n2$ are zero.

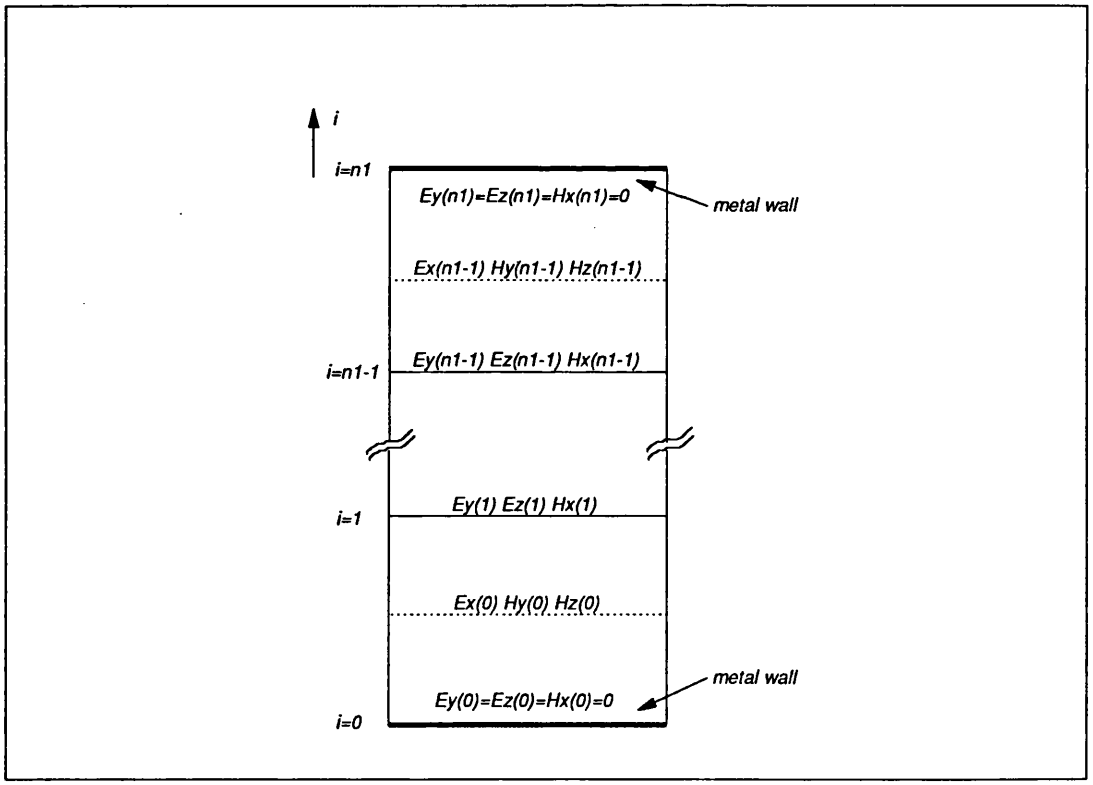

Figure 5.5: A part of the Yee's mesh along the x direction. Normal magnetic field and tangential electric fields at i=0 and i=$n1$ are zero.

5.6 Making Use of the Plane of Symmetry

When the code is run for the full structure with the excitation mentioned later, as expected for TE_{10} mode E_y, E_z, and H_x are zero. Also by such choice of the Yee's mesh explained in section 5.3 and considering Eqs. 5.9, 5.12, and 5.13 E_x and H_y are symmetrical with respect to the symmetrical plane which exists at the $j = js$ plane where $js = \frac{n2}{2}$. H_z is asymmetrical with respect to this plane and is zero on it. Thus on the symmetry plane all normal electric fields (here only E_y) and all tangential magnetic fields (H_x and H_z) are zero. As a result this plane can be considered as a Magnetic Wall (MW). Therefore for saving computer memory and CPU time, the analysis can be performed for half of the computational domain and the necessary iterations instead of starting j=0 can be started from j=js.

Now for analysing the half structure starting from $j = js$, first $E_x^{n+1}(i, js, k)$ must be calculated and it needs the value of $H_z^{n+\frac{1}{2}}(i, js-1, k)$ because:

$$E_x^{n+1}(i, js, k) = E_x^n(i, js, k) +$$
$$\alpha_E \left[H_z^{n+\frac{1}{2}}(i, js, k) - H_z^{n+\frac{1}{2}}(i, js-1, k) - H_y^{n+\frac{1}{2}}(i, js, k) + H_y^{n+\frac{1}{2}}(i, js, k-1)\right]$$

For calculating $H_z^{n+\frac{1}{2}}(i, js-1, k)$ consider:

$$H_z^{n+\frac{1}{2}}(i, js-1, k) = H_z^{n-\frac{1}{2}}(i, js-1, k) +$$
$$\alpha_H \left[E_x^n(i, js, k) - E_x^n(i, js-1, k) - E_y^n(i+1, js, k) + E_y^n(i, js, k)\right]$$

Now the values of $H_z^{n-\frac{1}{2}}(i, js-1, k)$ and $E_x^n(i, js-1, k)$ must be known. Based on what have mentioned above and considering Fig. 5.6 these values are:

$$E_x^n(i, js-1, k) = E_x^n(i, js+1, k)$$

$$H_z^{n-\frac{1}{2}}(i, js-1, k) = -H_z^{n-\frac{1}{2}}(i, js, k)$$

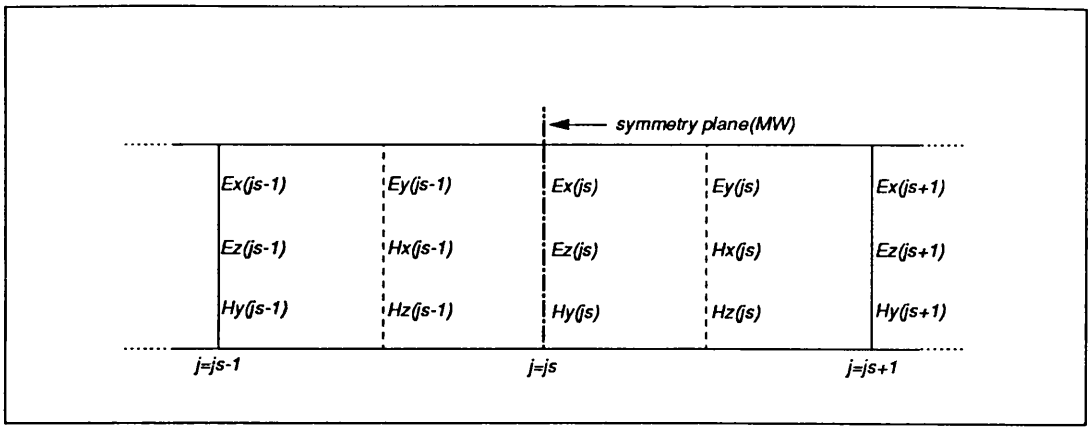

Figure 5.6: A part of the Yee's mesh and the field components around the symmetry plane.

and finally:

$$H_z^{n+\frac{1}{2}}(i, js-1, k) = -H_z^{n-\frac{1}{2}}(i, js, k) +$$
$$\alpha_H \left[E_x^n(i, js, k) - E_x^n(i, js+1, k) - E_y^n(i+1, js-1, k) + E_y^n(i, js-1, k)\right]$$

5.7 Running the FDTD Analysis

The code is run for the half structure with the input data as shown in Table 5.1. The centre frequency is 11.25 GHz and most of the BW_f values are 4 GHz. To have the TE_{10} mode the dimensions of the guide are $a = n2\delta$=2 cm and $b = n1\delta$=1 cm, therefore the cut-off wavelength from Eq. 5.4 is λ_c=4 cm and from Eq. 5.5 the cut-off frequency is f_c=7.5 GHz. Approximately, the smallest wavelength is 2 cm (regarding cut-off frequency of the second mode which is 15 GHz); therefore, based on section 3.4 ($\delta \leq \frac{\lambda}{10}$) δ (=$\Delta x = \Delta y = \Delta z$) is chosen to be equal 1 mm. Therefore $n1$=10 and $n2$=20. If the length of the guide is L=90 cm, $n3$ will be 900. For all cases $\mu_r = \epsilon_r$=1.

Table 5.1 :*Input data for specific cases considerd.*

case no.	$n1$	$n2$	$n3$	mnt	t_p	f_o (GHz)	BW_f (GHz)	*direc.of prop.*	k_s
1	10	20	900	6000	450	11.25	4	$+z$	0.5
2	,,	,,	,,	,,	,,	,,	,,	,,	0.4
3	,,	,,	,,	,,	,,	,,	,,	,,	$v/2vp$
4	,,	,,	,,	,,	,,	,,	,,	$-z$	0.5
5	,,	,,	600	4000	250	,,	,,	$+z$	,,
6	,,	,,	900	,,	,,	,,	2	,,	,,

5.7.1 Computations Derived From Input Data

Other parameters are calculated by the relevant relations (Eq. 5.7, 5.27, and 5.29). For cases 1-6 the results are in Table 5.2:

Table 5.2 :*Parameters for cases* $1-6$.

v_p (m/sec)	v_g (m/sec)	c_f
4.02492×10^8	2.23607×10^8	1.8

Parameters Relevant to the Inverse Fourier Transform

Table 5.3 shows parameters relevant to the inverse Fourier transform. In this computation tnp (total number of points of $E_x(t)$) is 3000. From Eq. 5.14 and 5.15:

$$y_p = y_n \Delta t \tag{5.30}$$

From Eq. 5.14 and definition of BW_t:

$$BW_t = 2y_p \tag{5.31}$$

therefore $y_p = \frac{BW_t}{2}$ and $y = \frac{y_p}{\Delta t}$.

Table 5.3 :*Parameters relevant to the inverse Fourier transform.*

case no.	BW'_f (GHz)	BW'_t $(psec)$	BW'_s (cm)	Δt $(psec)$	df (GHz)	y_p $(psec)$	y_n
$1-5$	7.2	176.839	7.1176	1.2423	0.2683	88.4195	71.174
6	3.6	353.678	14.2352	,,	,,	176.839	142.35

Parameters Relevant to the FDTD Code

Table 5.4 shows parameters relevant to the FDTD code. As expected $BW'_s = BW_s$ because it is the link between the FDTD and inverse Fourier transform codes.

Table 5.4 :*Parameters relevant to the FDTD code.*

case no.	BW_t *(psec)*	BW_s *(cm)*
$1-5$	318.31	7.1176
6	636.62	7.1176

Δt $(= k_s \frac{\delta}{v})$ depending on the value of k_s and Table 5.5 shows the results for all cases.

Table 5.5 :*Values of* Δt *relevant to the FDTD code.*

case no.	Δt *(psec)*
1,4,5,6	1.6666
2	1.3333
3	1.2423

It should be pointed out that in all the plots i=2 and j=10 is chosen as the monitor point.

5.7.2 Using 1st Order Mur's ABC

The analysis has been done using the above input data and 1st order Mur's ABC for both ends of the guide (k=0 and k=n3).

Case 1

Figure 5.7 shows the magnitude of Fourier transform of Ex, Hy, and Hz. This figure shows that BW_f is 7.2 GHz which is 4 GHz multiplied by c_f.

For the first three time steps (n=0,1, and 2) Figure 5.8 shows the three main components as a function of z (k). From this figure it can be seen proper propagation of these components in the $+z$ direction. Figure 5.9 shows this fact better by examining a smaller range.

Figure 5.10 shows the evolution of propagating pulse and the spread of $E_x(z)$ along the line for three time steps n=400, 800, and 1200. The small back projection pulse is because of the approximations in the excitation stage.

Figure 5.11 shows $E_x(t)$, $H_y(t)$, and $H_z(t)$ as a function of time at z=150 mm. In each case, the first pulse is the back projection of the wave which is a small portion of the main pulse and reaches to this point of line after the time equal $\frac{(450-150)mm}{vg}$=1.345 $nsec$. The second pulse is the reflection of the main pulse by the 1st order Mur's ABC. This reflection pulse reaches to this point of the line after a time $\frac{(450+(900-150))mm}{vg}$=5.367 $nsec$. Figure 5.12 shows these components at z=600 mm. This point on the line is selected because of the possibility of separating main and reflection pulses in time.

Figure 5.13 shows the Fourier Transform (F.T.) of the Incident Pulse (I.P.), and the Reflected Pulse (R.P.) at z=600 mm. It also shows Reflection Coefficient (R.C.) at this point on the line.

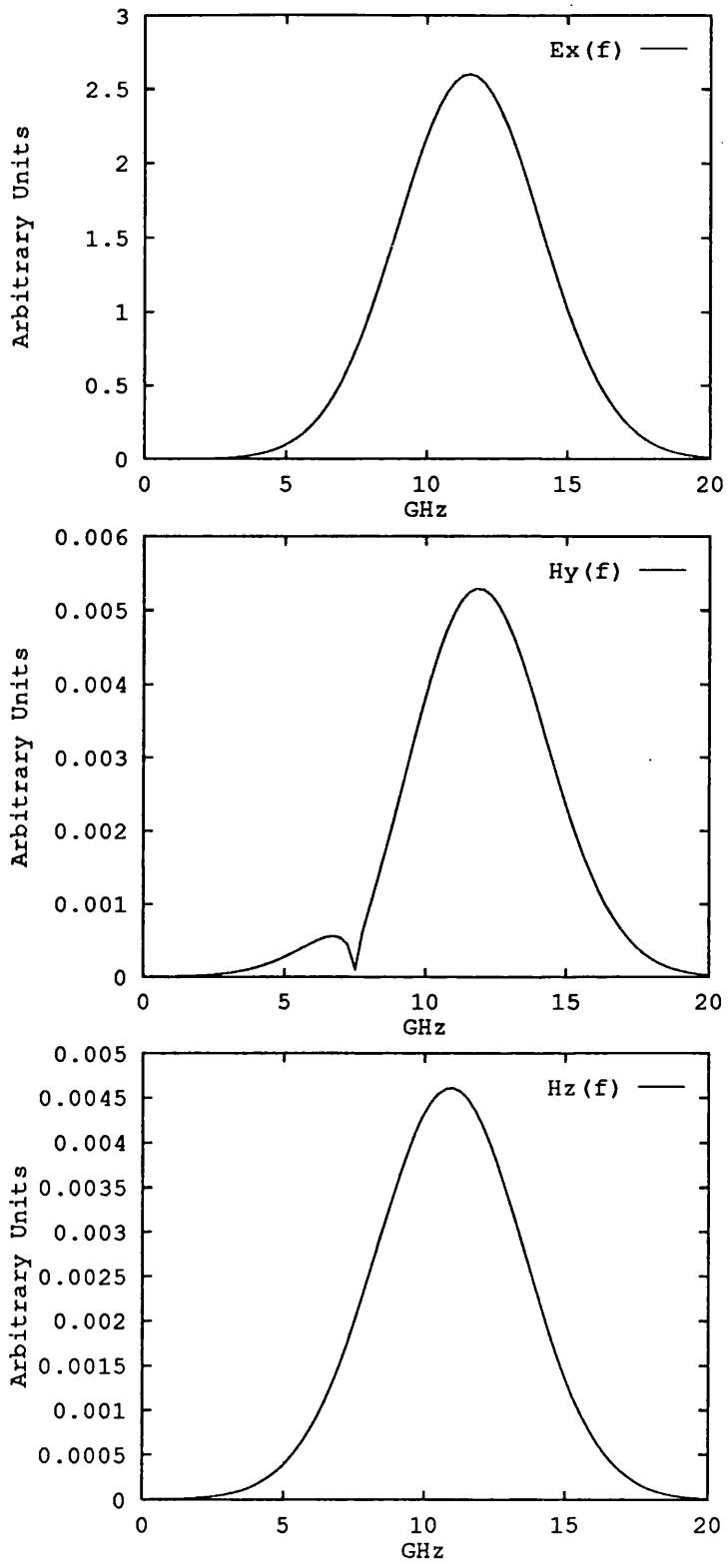

Figure 5.7: Magnitude of the Fourier transform of the E_x, H_y, H_z.

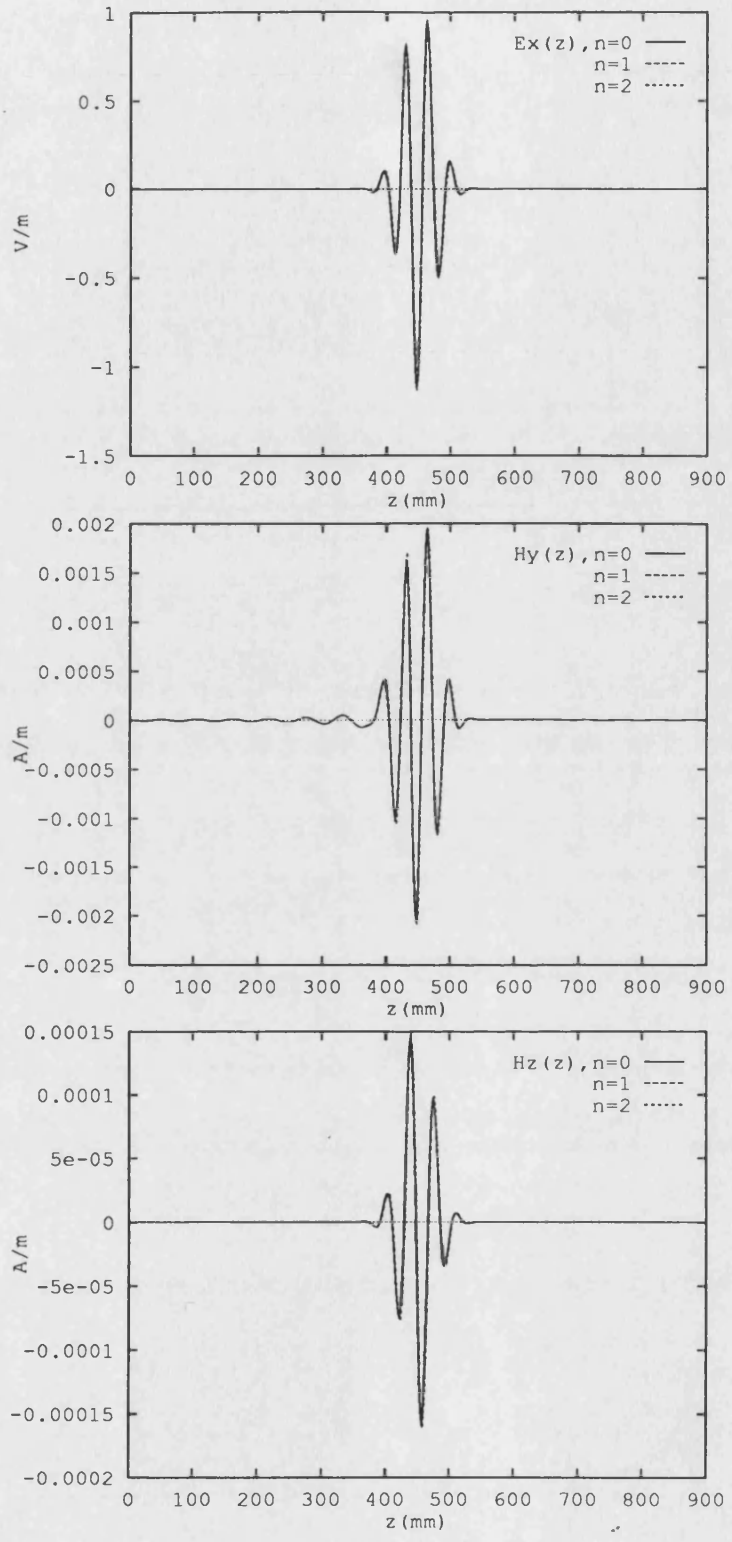

Figure 5.8: E_x, H_y, and H_z as a function of z for the first three time steps n=0,1 and 2.

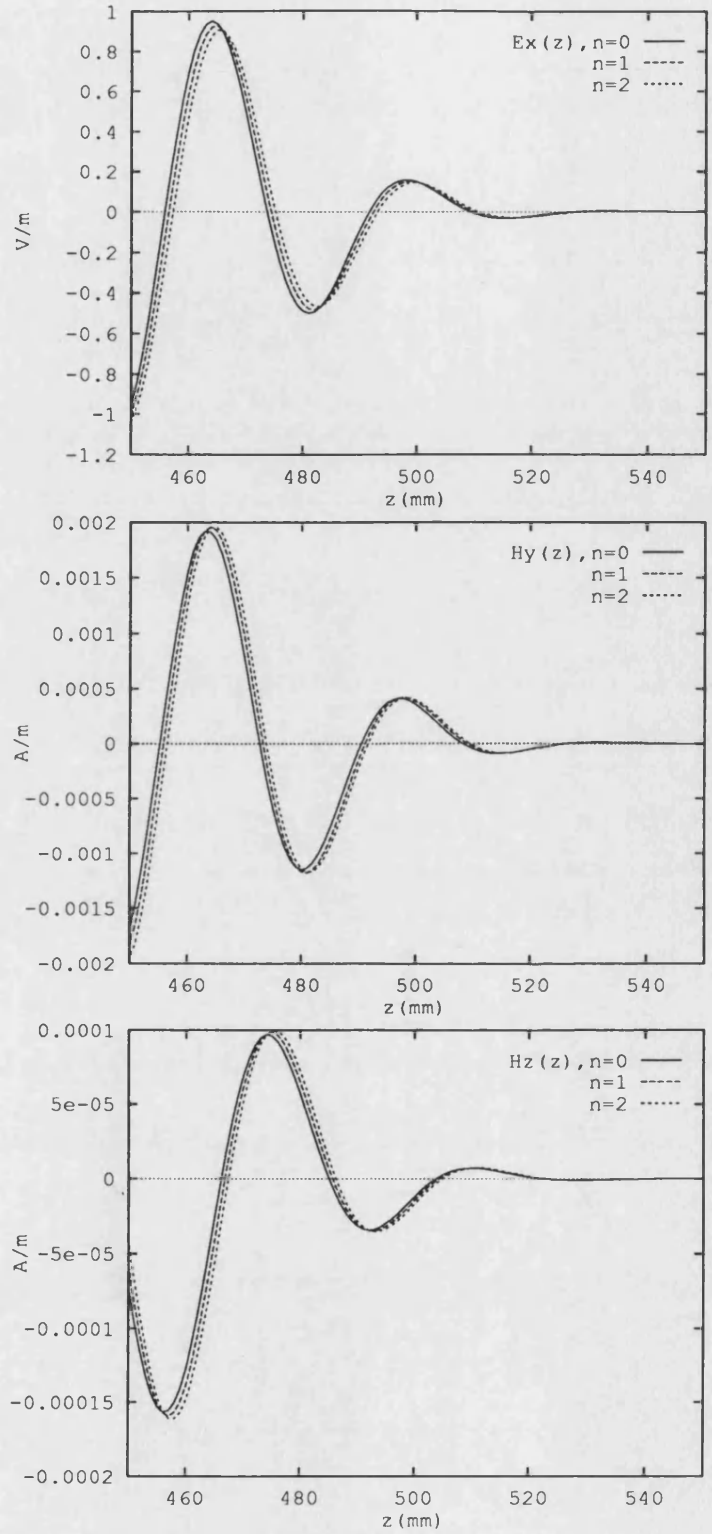

Figure 5.9: E_x, H_y, and H_z as a function of z for the first three time steps n=1,2, and 3 on the range of 450-600 mm.

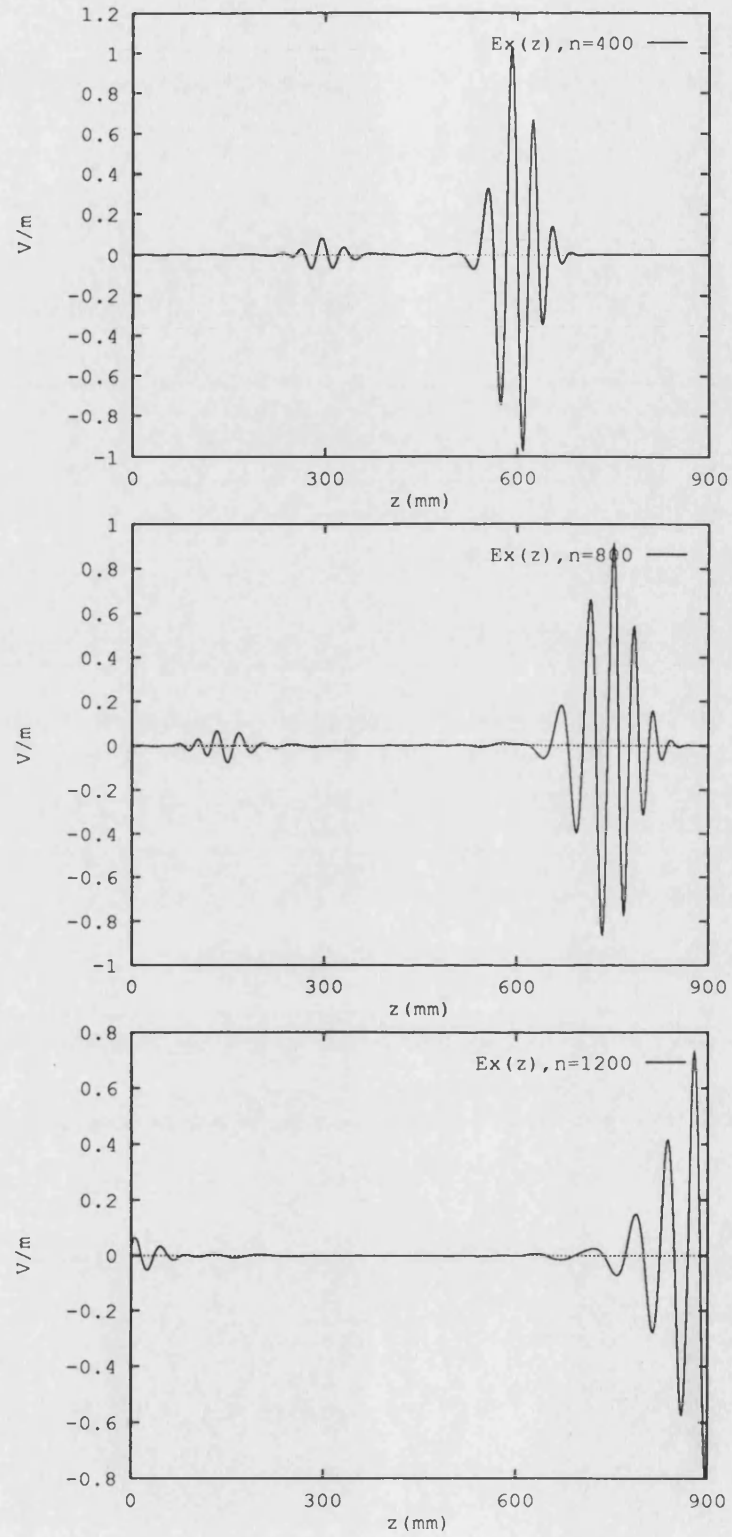

Figure 5.10: Evolution of propagation and spread of the $E_x(z)$ along the line.

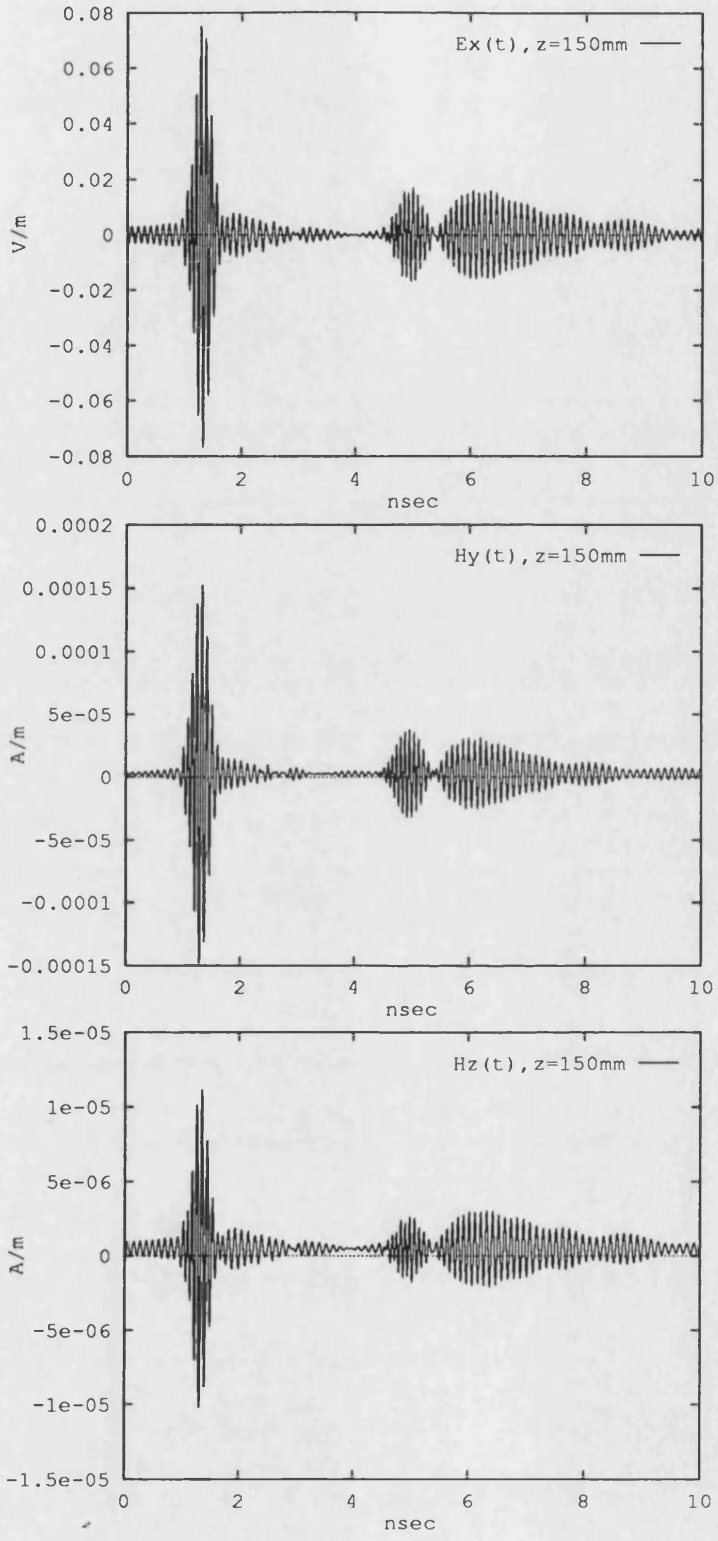

Figure 5.11: $E_x(t)$, $H_y(t)$, and $H_z(t)$ as a function of time at z=150 mm for case 1.

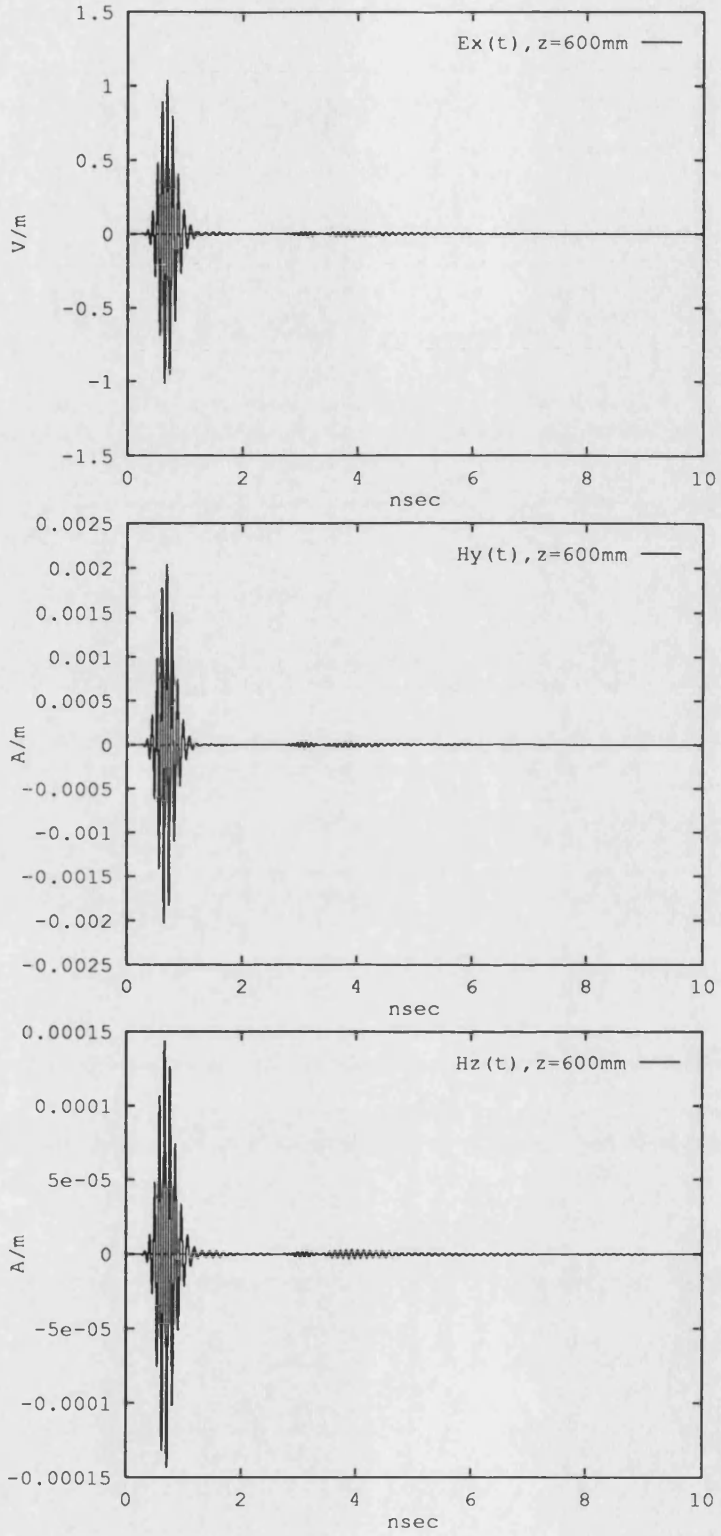

Figure 5.12: $E_x(t)$, $H_y(t)$, and $H_z(t)$ as a function of time at z=600 mm for case 1.

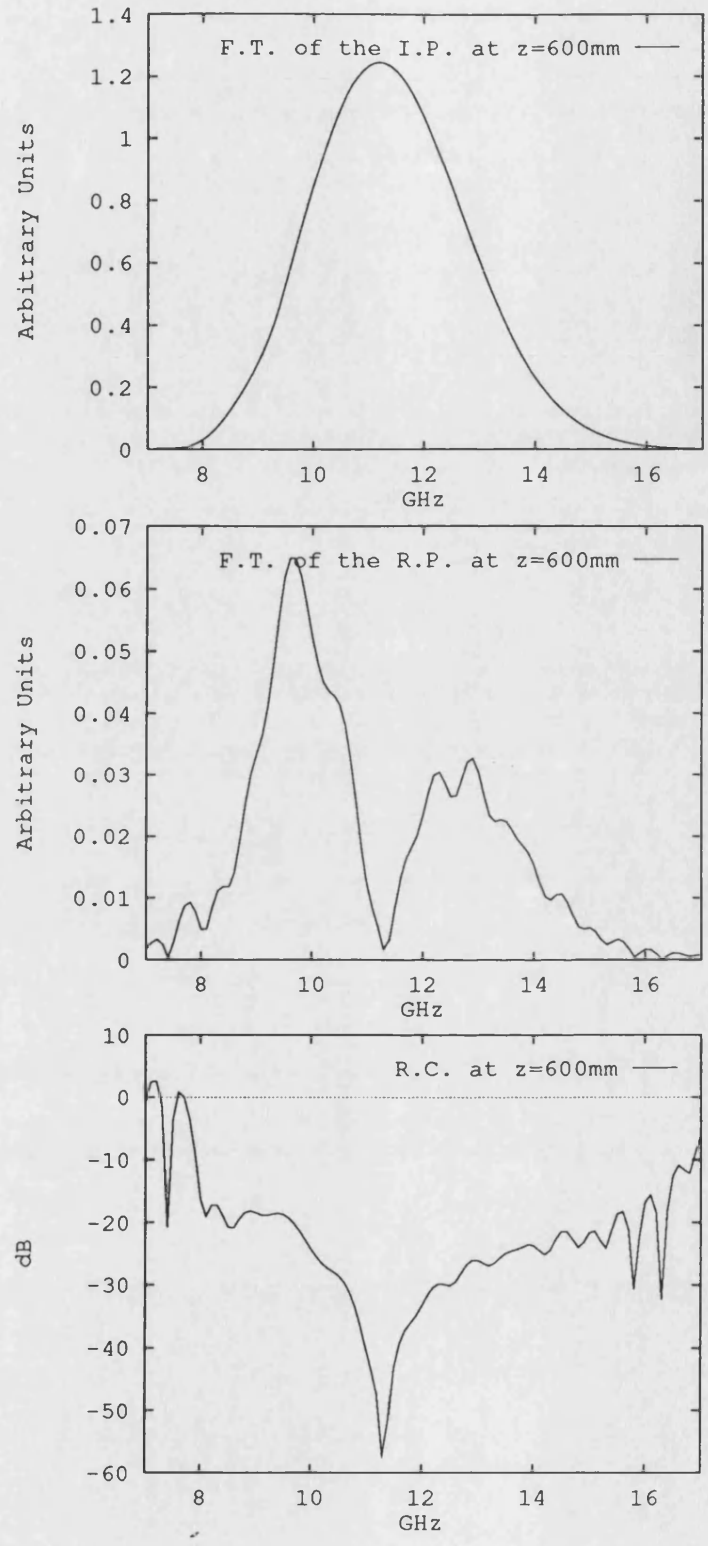

Figure 5.13: Fourier Transform (F.T.) of the Incident Pulse (I.P.), Reflected Pulse (R.P.) and Reflection Coefficient (R.C.) at z=600 mm for case 1.

Figure 5.14 shows Transmission Coefficient (T.C.) of the line for the point z=650 mm referred to the point z= 600 mm.

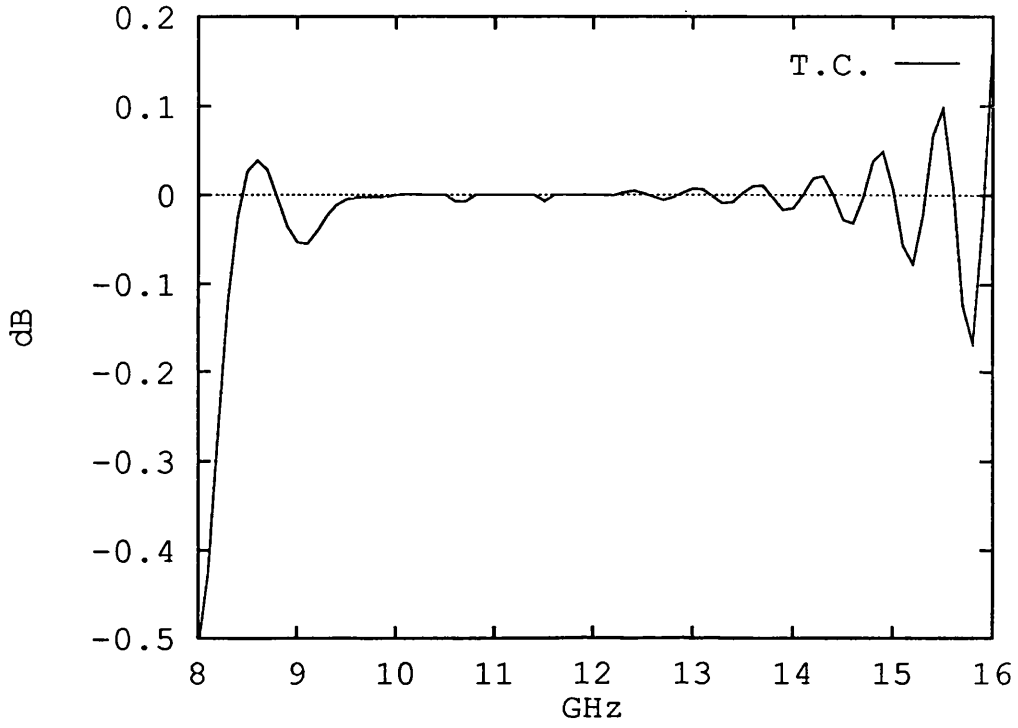

Figure 5.14: Transmission Coefficient (T.C.) of the line at the point z =650 mm with respect to the point z=600 mm for case 1.

Cases 1, 2, and 3

The purpose of this part is to show that when Δt in the FDTD code is changed and consequently k_s is changed (provided that it satisfies the Courant stability factor mentioned in Chapter 3) the results are not affected. In addition it shows that it is not necessary that Δt in the inverse Fourier transform and the FDTD codes be the same.

Figure 5.15 shows $E_x(t)$ at z=600 mm against number of time steps (nts) for the three mentioned cases. Because Δts are different in these cases, different nts are required for different pulses to reach a particular point of the lines. But if they

are plotted as a function of time they will be the same and Fig. 5.16a shows this fact.

Figure 5.16b shows reflection coefficient (R.C.) at z=600 mm for the three cases 1, 2, and 3.

Case 4

In case 4 the direction of propagation of the initial pulse is reversed (-z). The purposes of this case are a double check of the inverse Fourier transform and the FDTD code and an investigation about the similarity of the behaviour of the 1st order Mur's ABC at both ends of the line. Fig. 5.17 shows the evolution of propagation and split of $E_x(z)$ along the line for n=400, 800, and 1200. This figure can be compared with Fig. 5.10. It shows that their propagation characteristics are the same but their directions are different.

The incident pulses at two points of the line which are symmetric with respect to the centre of the line are the same for cases 1 and 4. Figure 5.18 shows $E_x(t)$ at z=300 mm for case 4 which is the same as $E_x(t)$ at z=600 mm for case 1 (Fig. 5.16 a).

Figure 5.19 shows the Fourier transforms of the incident, reflected pulses and reflection coefficient for: a)case 4 at z=300 mm and b)case 1 at z= 600 mm.

Case 5

The purpose of this case is to show that the excitation pulse can be moved to the left (for propagation toward $+z$) and the length of the line and nts can then be reduced. Therefore there is a saving in both CPU time and computer memory. Fig. 5.20a shows $E_x(z)$ for n=0 which the peak of the pulse is at z=250 mm and

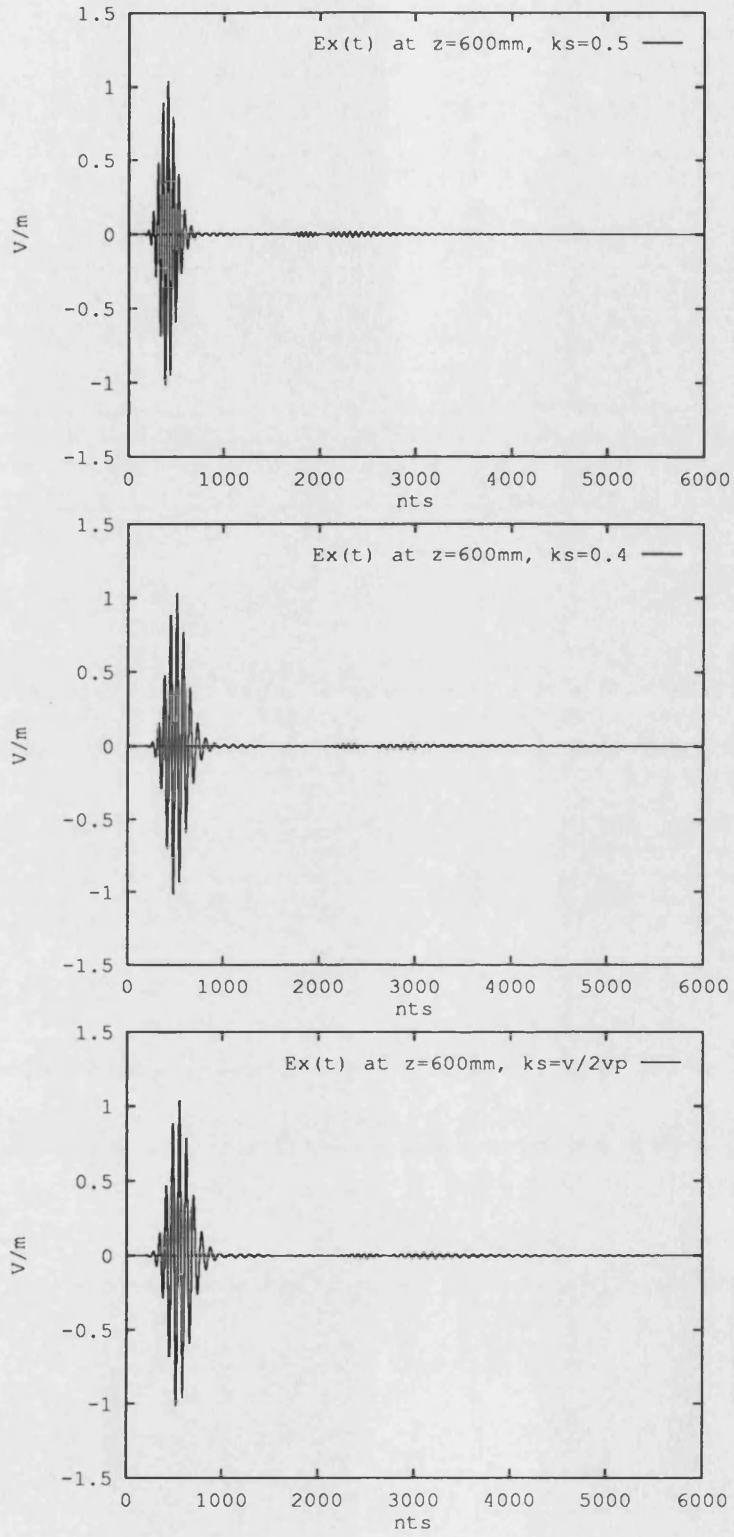

Figure 5.15: $E_x(t)$ at z=600 *mm* against *nts* (number of time steps) for cases 1, 2, and 3.

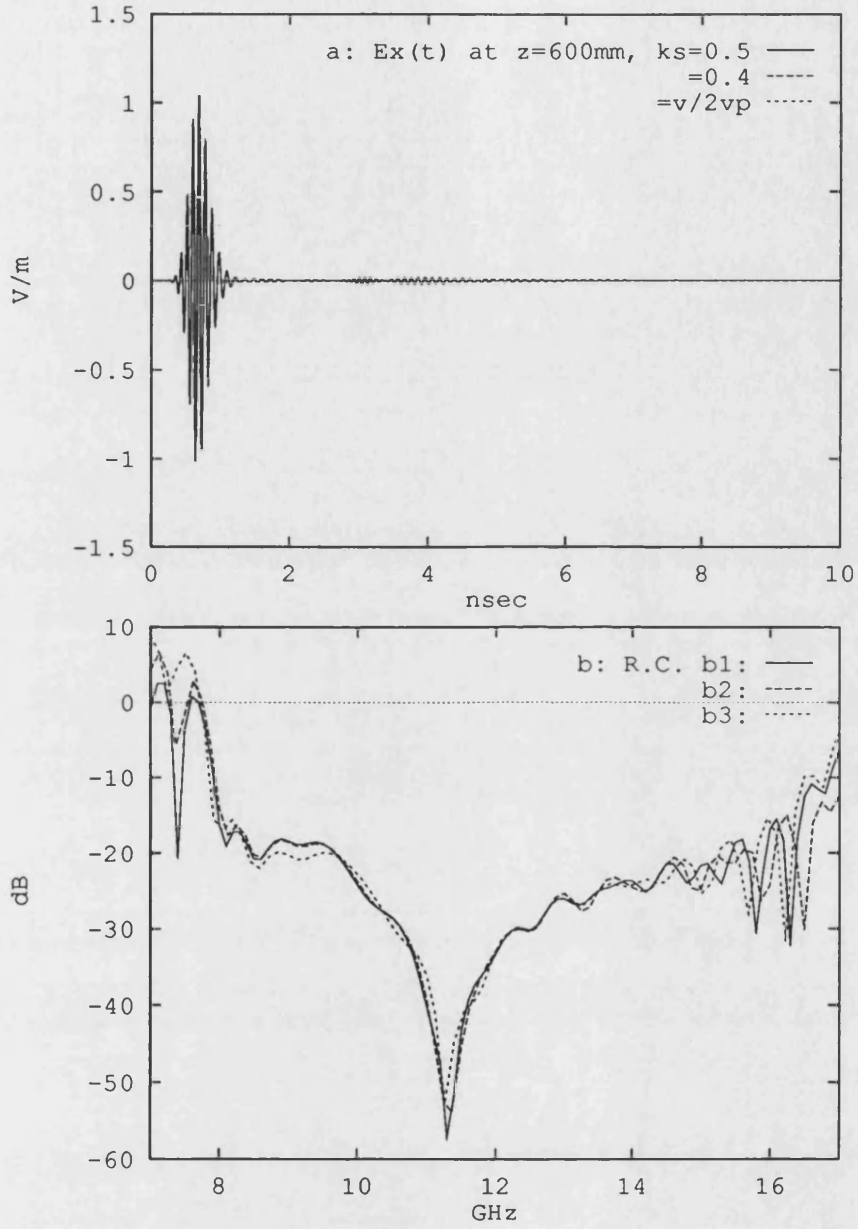

Figure 5.16: a) $E_x(t)$ at z=600 mm against time for different k_s (different Δt) for cases 1,2, and 3 b)Reflection Coefficient (R.C.) at z=600 mm for three cases b1)k_s=0.5 b2)k_s=0.4 b3)$k_s = v/2vp$.

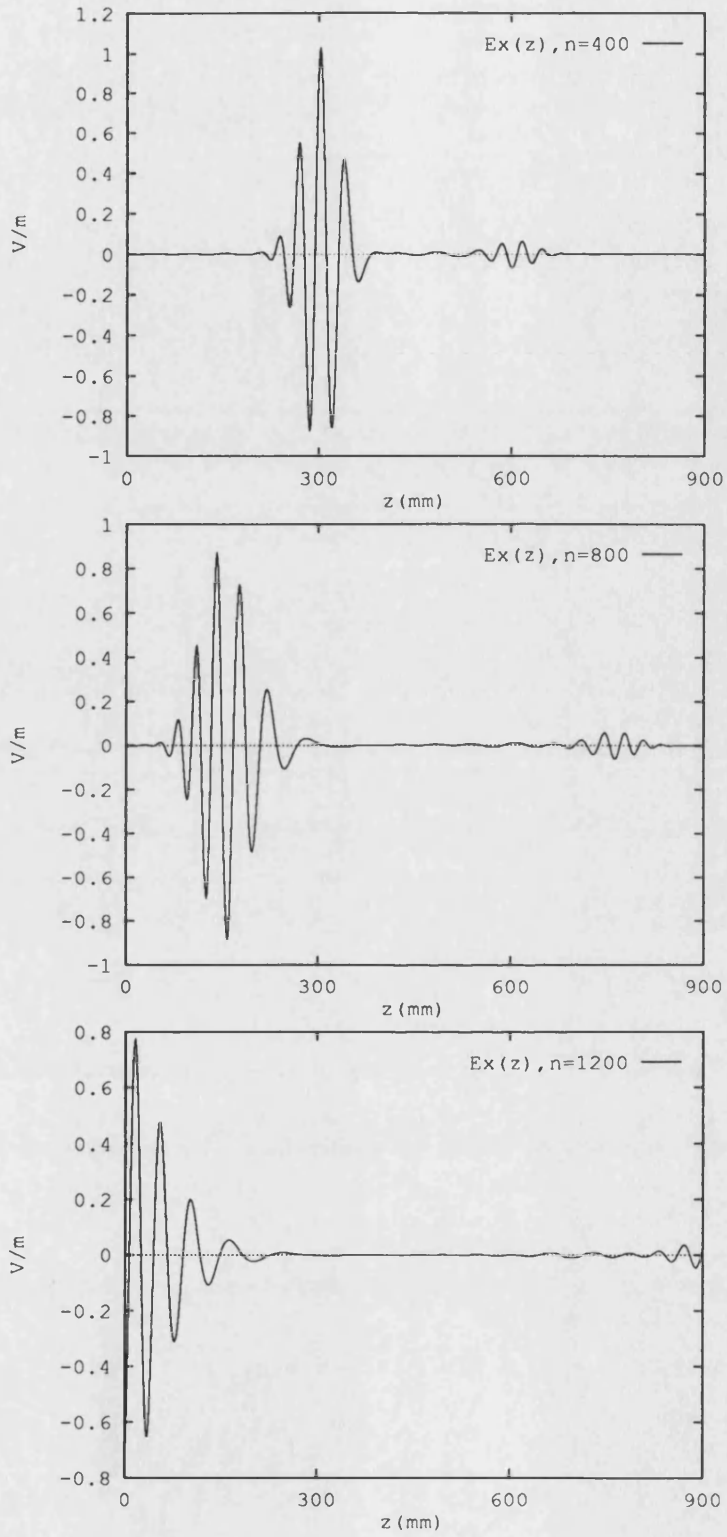

Figure 5.17: $E_x(z)$ at n=400, 800, and 1200 when the direction of propagation is -z for case 4.

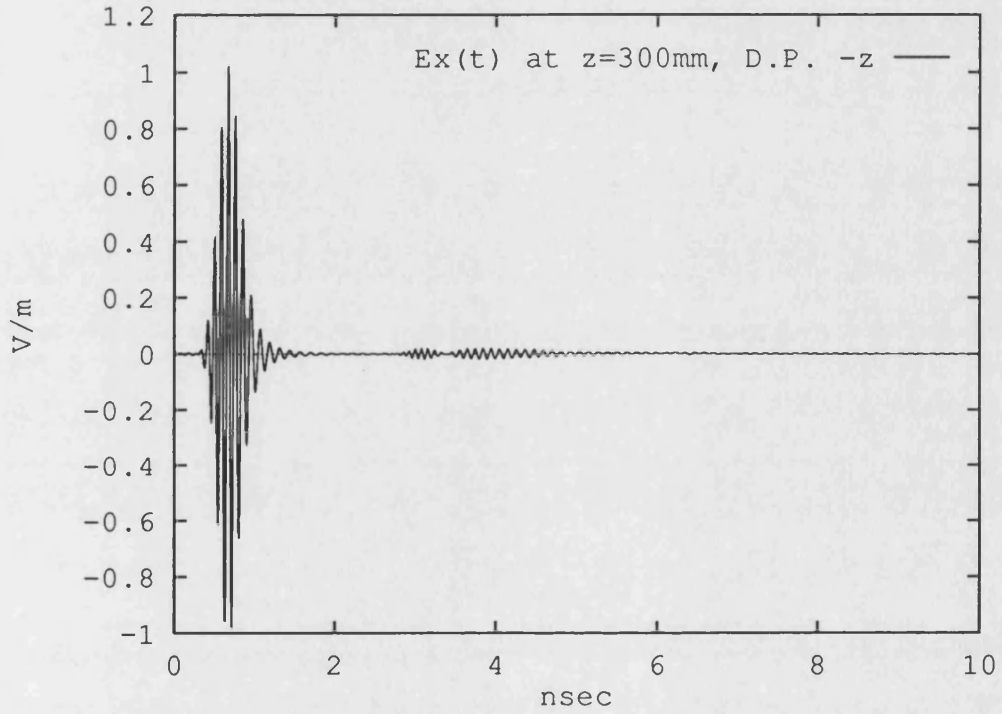

Figure 5.18: $E_x(t)$ at z=300 mm when Direction of Propagation (D.P.) is -z for case 4.

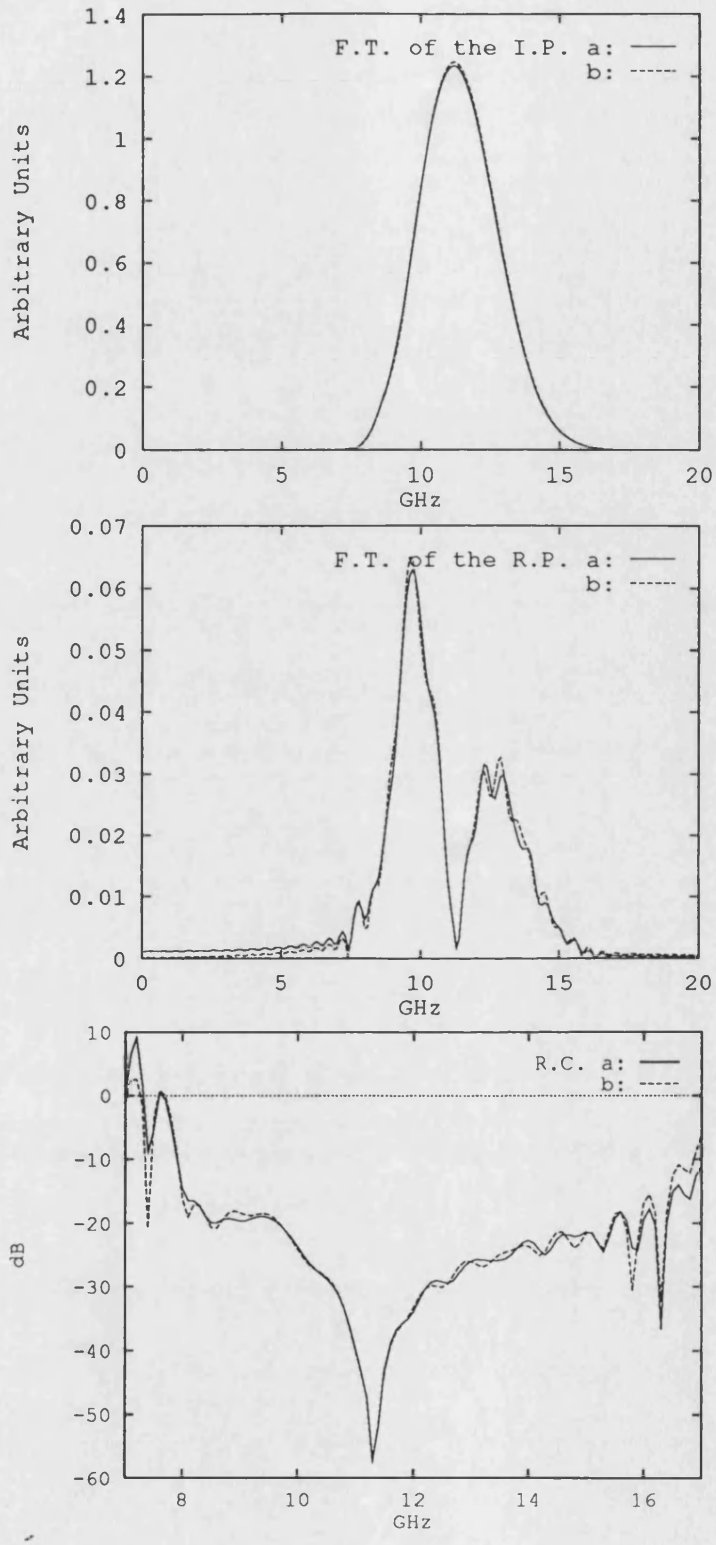

Figure 5.19: Fourier Transform (F.T.) of Incident Pulse (I.P.), Reflected Pulse (R.P.) and Reflection Coefficient (R.C.) for a)case 4 at z=300 mm b)case 1 at z=600 mm.

5.20b shows $E_x(t)$ at z=350 mm and from this the possibility of separating the incident and reflected pulses can be observed.

From Fig. 5.21 reflection coefficient for two cases a: case 5 at z=350 mm and b: case 1 at z=600 mm are comparable.

Case 6

In this case BW_f=2 GHz and Fig. 5.22 shows that by reducing BW_f the left lobe of the $H_y(f)$ (Fig. 5.7) and left tail of $H_y(z)$ (Fig. 5.8) have been removed and incident and reflected pulses are more separable. Consequently their separation in time will be better. BW_f' for $H_y(f)$ is $c_f BW_f$=3.60 GHz and BW_s for $H_y(z)$ is 142.43 mm.

Figure 5.23 shows Fourier transform of the incident pulse at z=600 mm, and the reflection coefficients at z=600 mm for: a)case 6 b)case 1. It shows that the R.C. for the two cases are largely the same.

Figure 5.24 compares transmission coefficients for two cases a)for case 6 at z=700 mm referring to z=600 mm and b) case 1 at z=650 mm referring to z=600 mm. It shows that case 1 has broader bandwidth of frequency if the T.C. is considered between -0.1 and +0.1 dB.

5.7.3 Using PML ABC

In this section the PML ABC is used at both ends of the rectangular waveguide. As described in Chapter 4, for practical implementation, the parameters nl, q, and σ_m (or $R(0)$) must be determined. Up to now there is no exact rule for optimisation of the PML parameters.

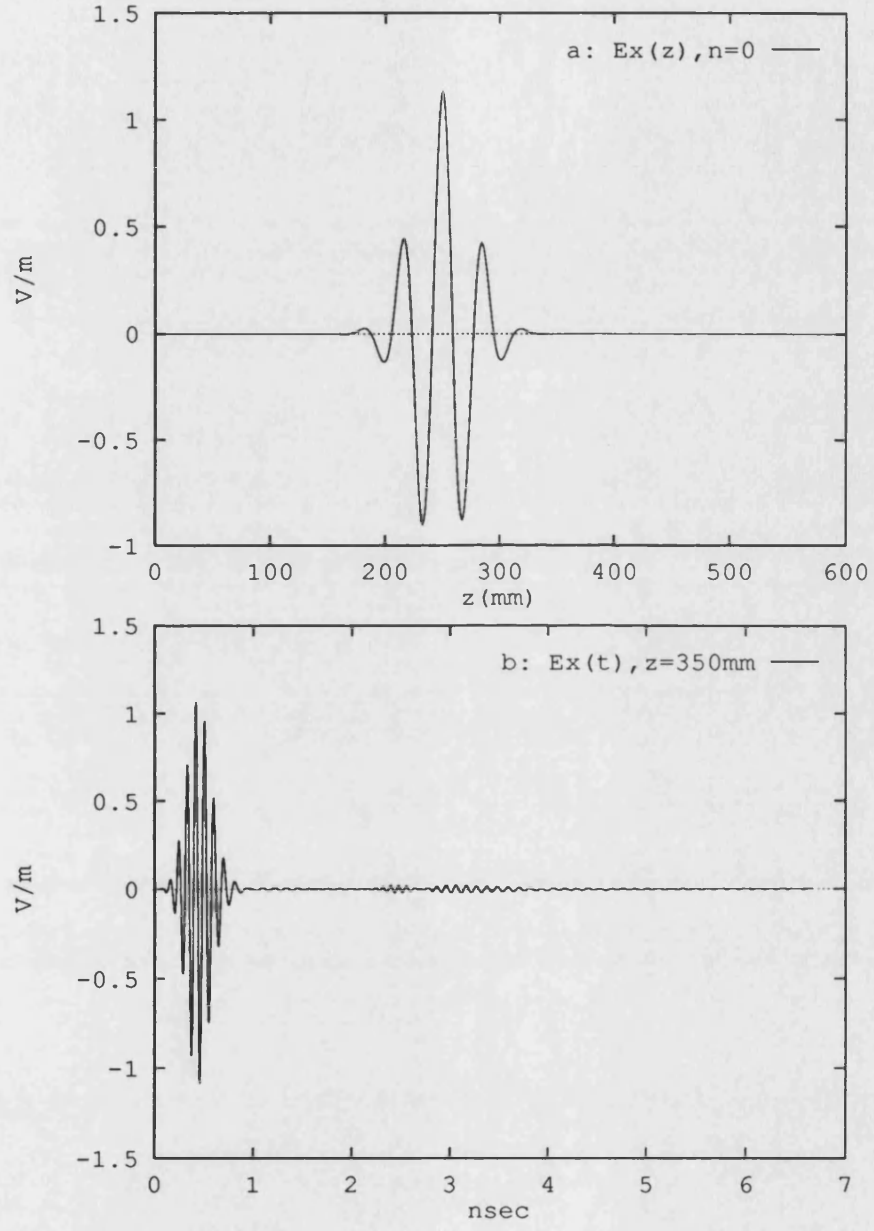

Figure 5.20: a)$E_x(z)$ when n=0 b)$E_x(t)$ at z=350 mm, for case 5.

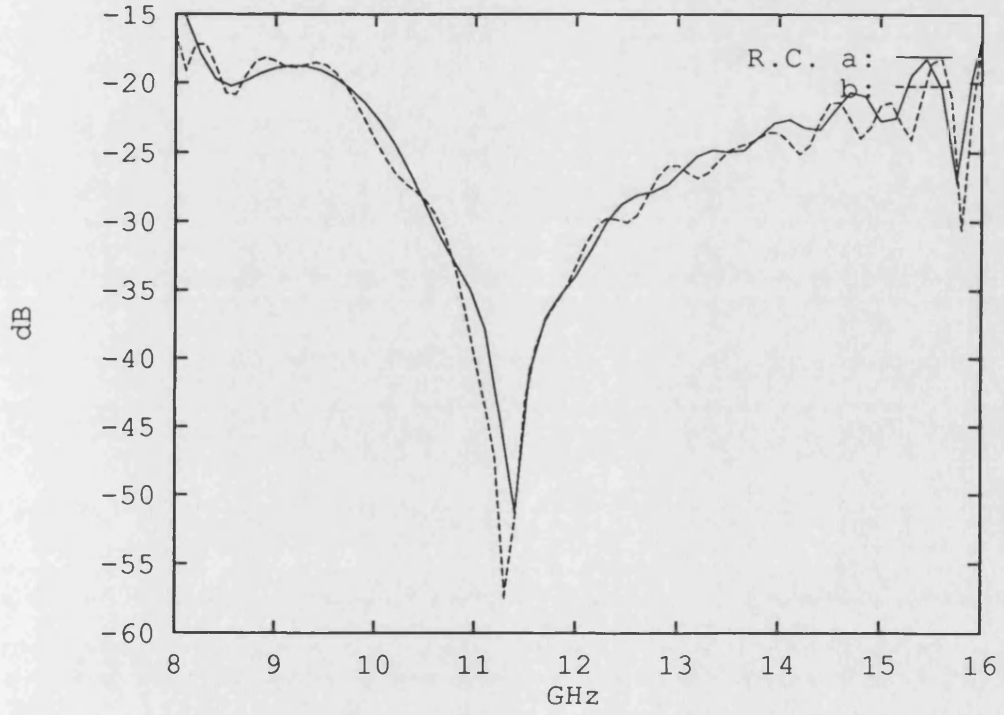

Figure 5.21: Reflection Coefficient (R.C.) a)case 5 at z=350 mm b)case 1 at z=600 mm.

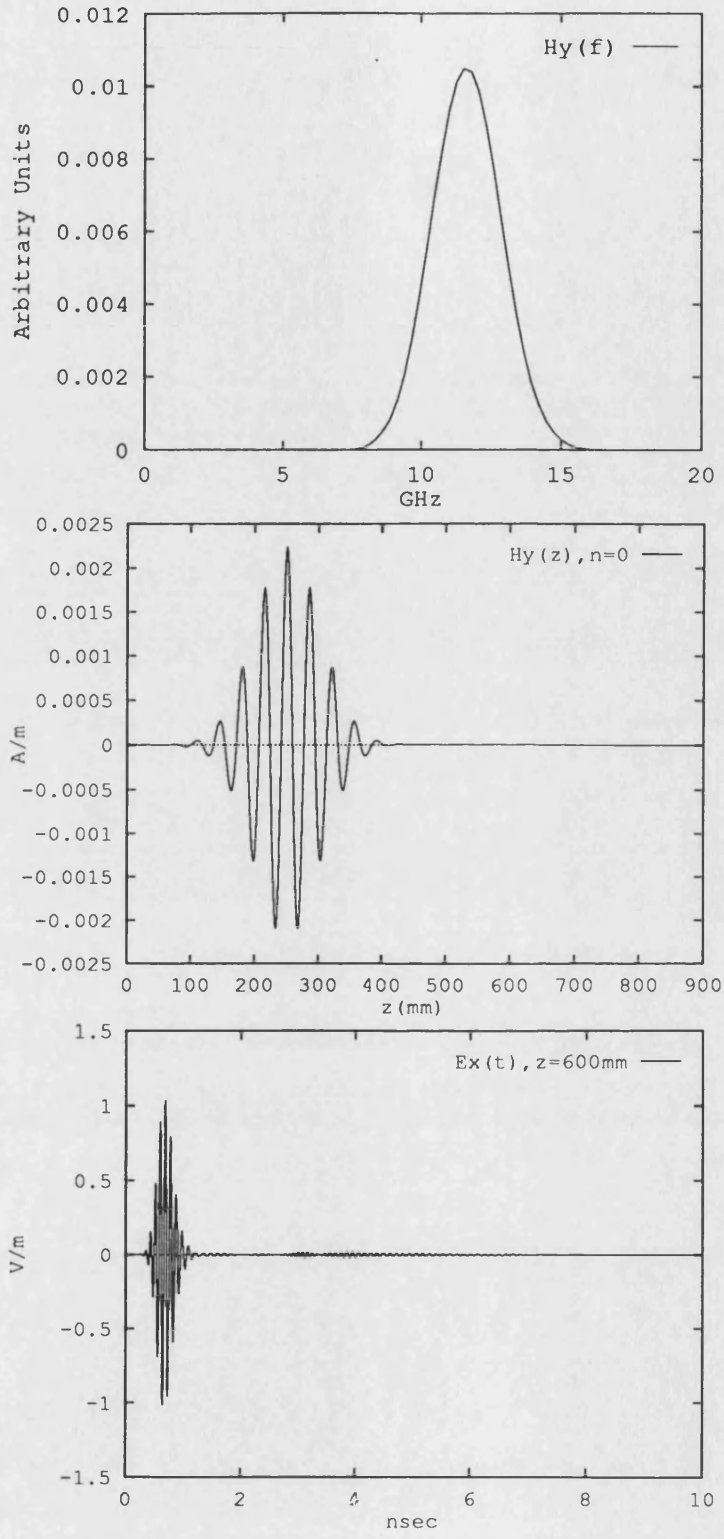

Figure 5.22: $H_y(f)$, $H_y(z)$ when n=0, and $E_x(t)$ at z=600 mm for case 6.

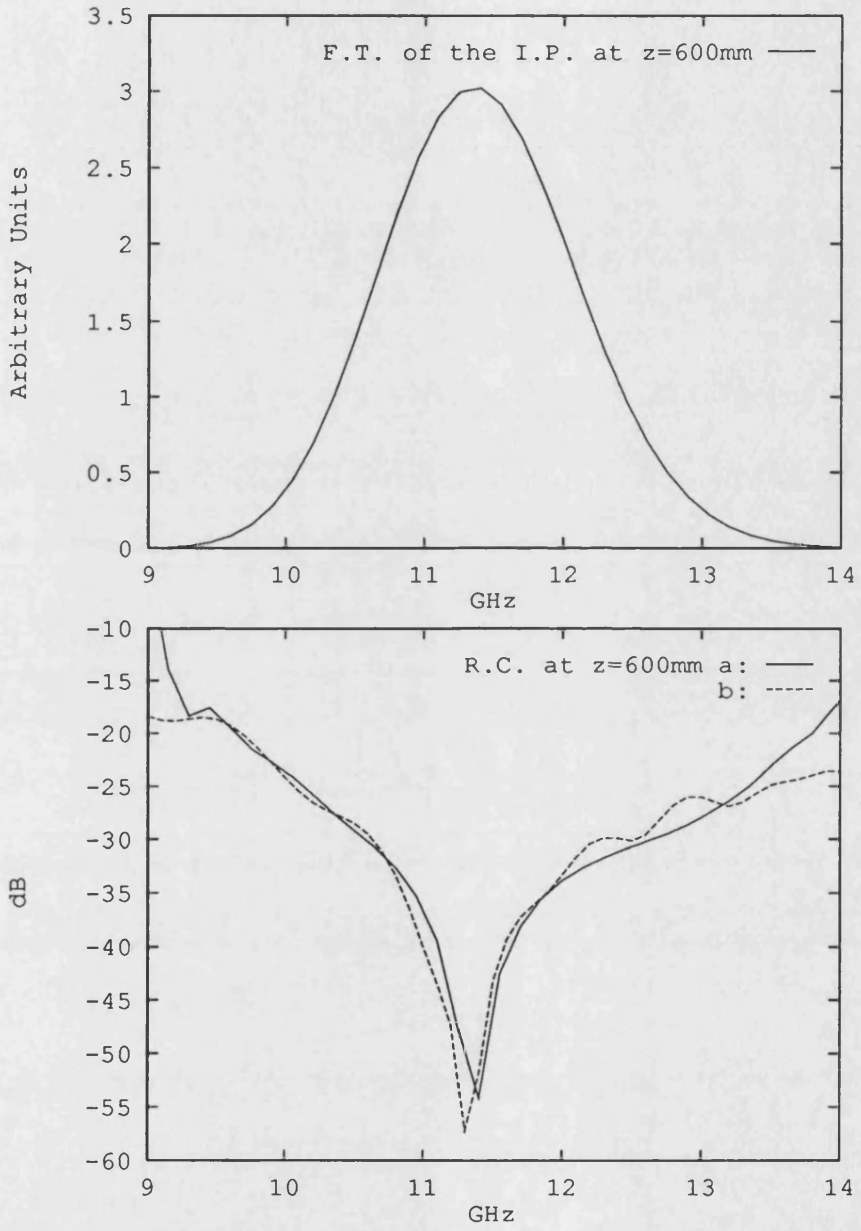

Figure 5.23: Fourier Transform (F.T.) of the Incident Pulse (I.P.) at z=600 mm for case 6, Reflection Coefficient (R.C.) at z=600 mm for a)case 6 b)case 1.

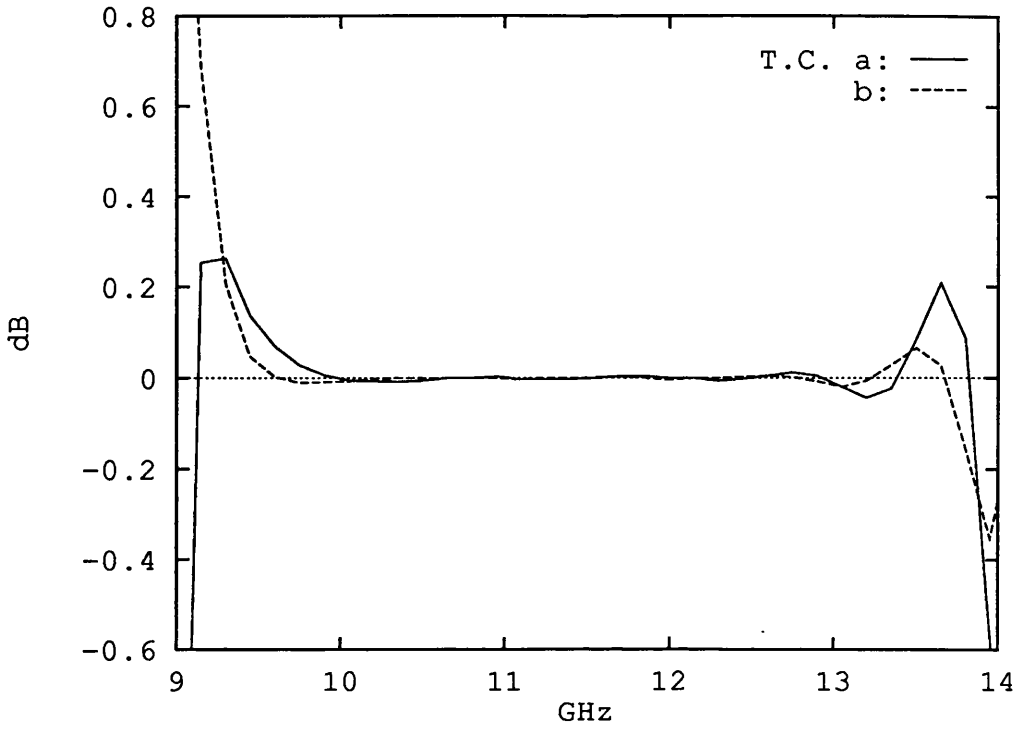

Figure 5.24: Transmission Coefficient (T.C.) for a)case 6 b)case 1

In the implementation k changes from -nl (z=-$nl\delta$) to $n3$+nl (z=L+$nl\delta$) therefore k=0 (z=0) is still the first point of the guide and $k = n3$ ($z = n3\delta = L$) is the end of the guide. For the analysis, case 5 of Table 5.1 is chosen as the input data. First some experiments have been done until appropriate ranges of these parameters have been found. However these experiments show that q=2 is good for starting and fairly good for a minimum of R.C. When nl is increased, R.C. will decrease, but after a while R.C. will saturate.

In this section some of the results of Reflection Coefficient (R.C.) at z=350 mm of the line for different values of these parameters along with R.C. of the 1st order Mur ABC are presented. The procedure is that first nl=10, q=2 are chosen then $R(0)$ varies from 10^{-6} to 10^{-1} and at each time σ_m by Eq. 4.38 and σ_m^* by Eq. 4.19 are calculated. After that, from among them the minimum of the R.C. is recognized for a particular of the $R(0)$ (or σ_m), then while keeping this $R(0)$ and nl=10, q varies for 1.5, 2.5, and 3. In another trial nl is changed to 15 and the

procedure is repeated

Figure 5.25 shows R.C. at z=350 mm of the line for case 5 when nl=10, q=2 and $R(0)$ changes from 10^{-6} to 10^{-1} with 1st order Mur ABC. This figure shows that when $R(0)$ changes, R.C. will change and $R(0)$=10^{-2} causes the minimum of the R.C. It also shows that for the centre frequency and narrow bandwidth of frequency, the 1st order Mur ABC has a lower R.C. than the PML ABC.

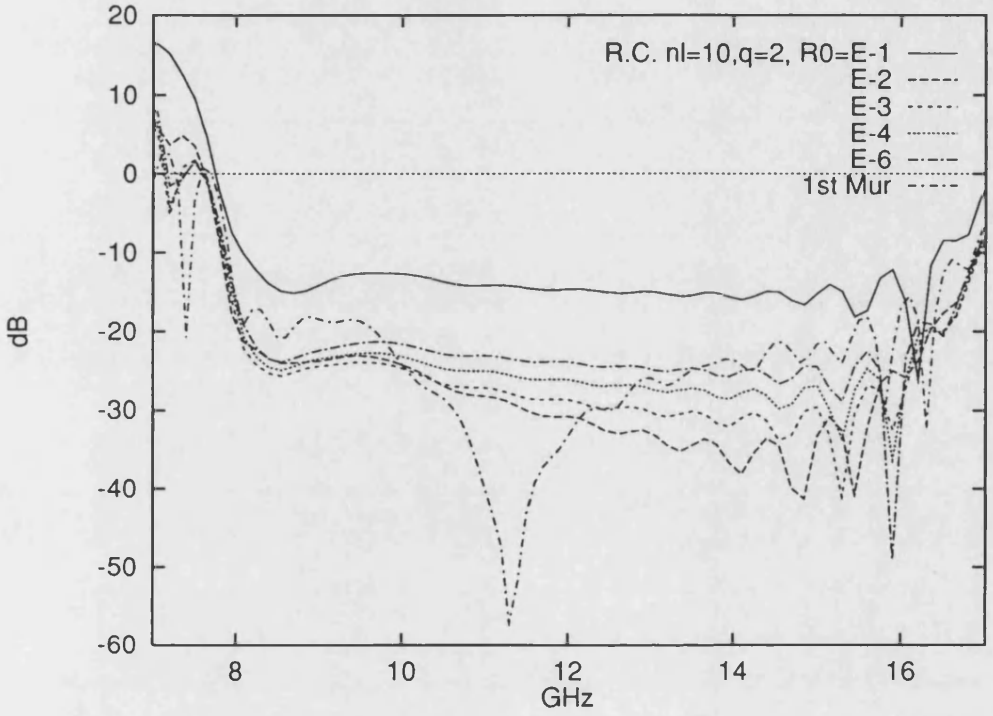

Figure 5.25: Reflection Coefficient (R.C.) at z=350 mm due to implementing ABCs at the end of the rectangular waveguide (z = 550 mm) for case 5 for 1st order Mur and the PML ABC when nl=10, q=2 and $R(0)$ is variable.

Figure 5.26 shows R.C. at z=350 mm of the lines when nl=10, $R(0)$ = 10^{-2} for q=3, 2.5, 2, and 1.5 and also comparison with the 1st order Mur ABC. This figure shows that changing q affects the R.C. For this case q=2.5 has the minimum of the R.C.

Figure 5.27 shows R.C. at z=350 mm of the line when nl=15, q=2 for $R(0)$=10^{-2},

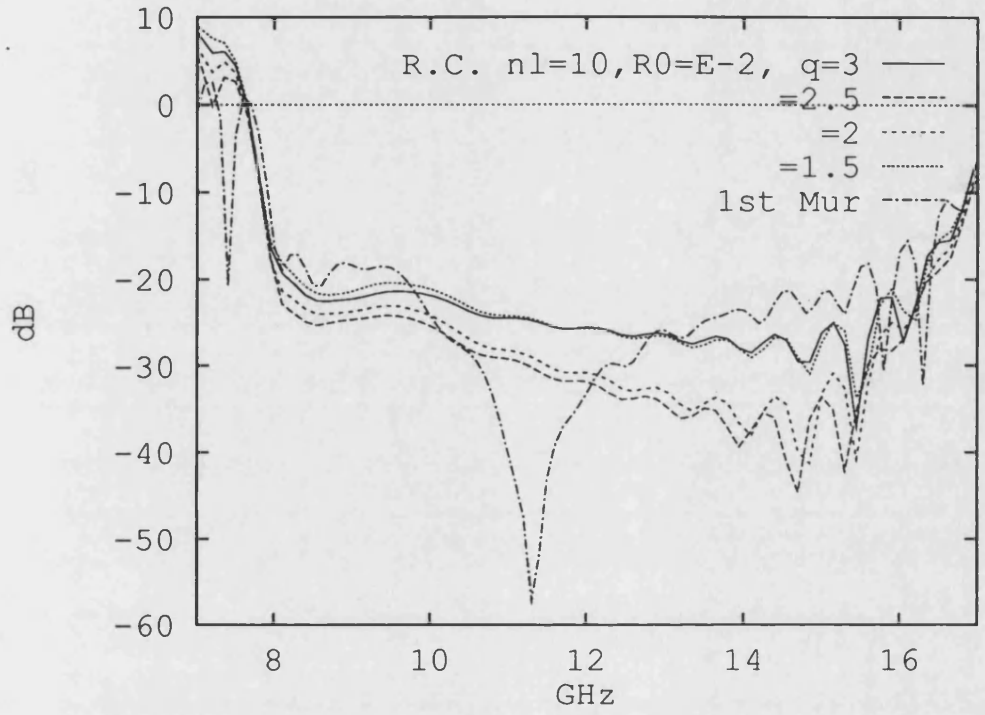

Figure 5.26: Reflection Coefficient (R.C.) at z=350 mm due to implementing ABCs at the end of the rectangular waveguide (z = 550 mm) for case 5 for PML ABC when nl=10, $R(0)$=10^{-2} and q =3, 2.5, 2, and 1.5, with 1st order Mur ABC.

10^{-3}, 10^{-4}, and the 1st order Mur ABC for comparison. It shows that for frequencies above the centre frequency $R(0) = 10^{-3}$ and for frequencies under the centre frequency $R(0) = 10^{-2}$ have lowest R.C.

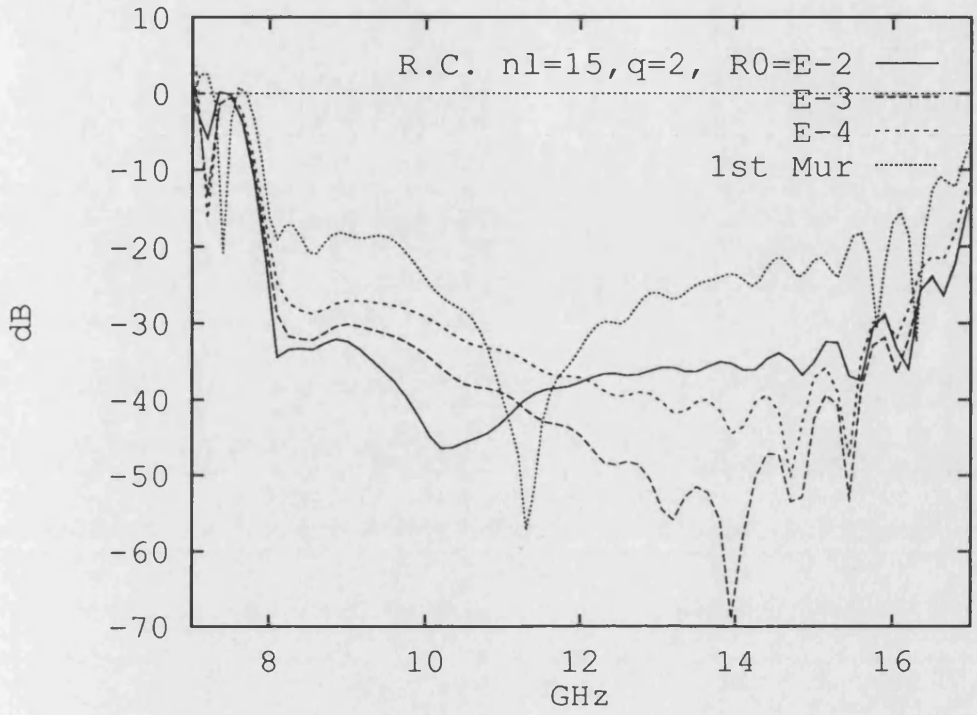

Figure 5.27: Reflection Coefficient (R.C.) at z=350 mm due to implementing ABCs at the end of the rectangular waveguide (z = 550 mm) for PML ABC when nl=15, q=2 for $R(0)$=10^{-2}, 10^{-3}, 10^{-4}, with 1st order Mur ABC.

Figure 5.28 shows R.C. at z=350 mm of the line when nl=15, $R(0)$=10^{-2} and q=2.5, 2, and 1.5 with 1st order Mur ABC. It shows that q=2 has the minimum of R.C.

Finally Fig. 5.29 shows R.C. at z=350 mm when q=2 and $R(0) = 10^{-2}$ for two values of nl=10 and 15 with 1st order Mur ABC. As expected R.C. for nl=15 is less than nl=10.

From this analysis it can be concluded that the PML ABC for nl=10, q=2, and $R(0)$=10^{-2} has a bigger frequency bandwidth of absorption than the 1st order Mur ABC. The 1st order Mur ABC is more effective around the centre

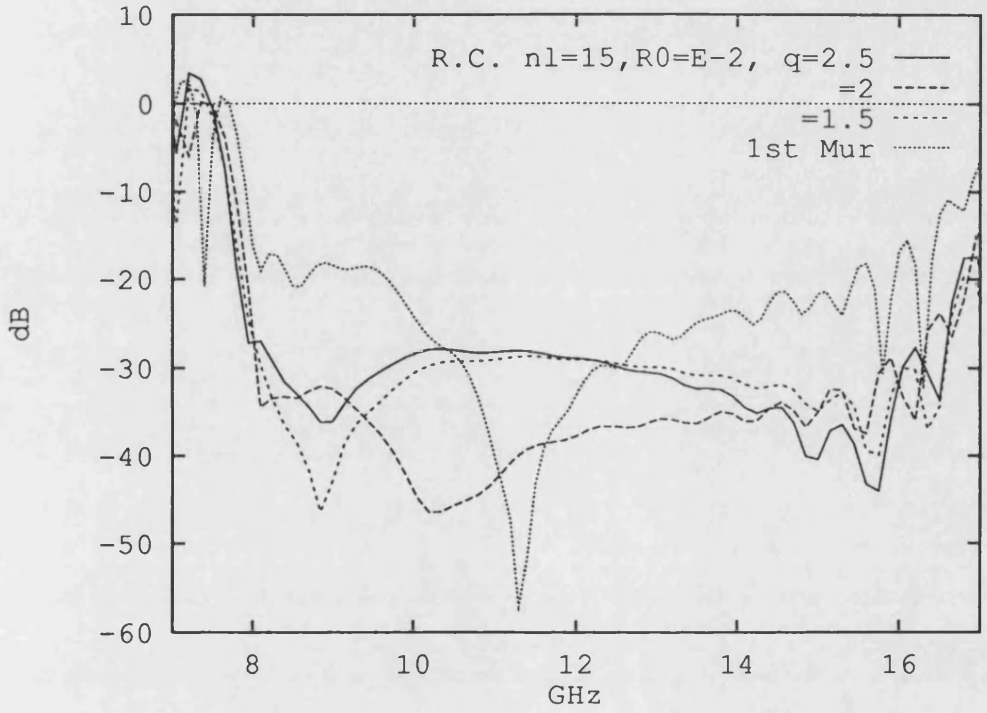

Figure 5.28: Reflection Coefficient (R.C.) at z=350 mm due to implementing ABCs at the end of the rectangular waveguide (z = 550 mm) for PML ABC when nl=15, $R(0)$=10^{-2} and q=2.5, 2, and 1.5 with 1st order Mur ABC.

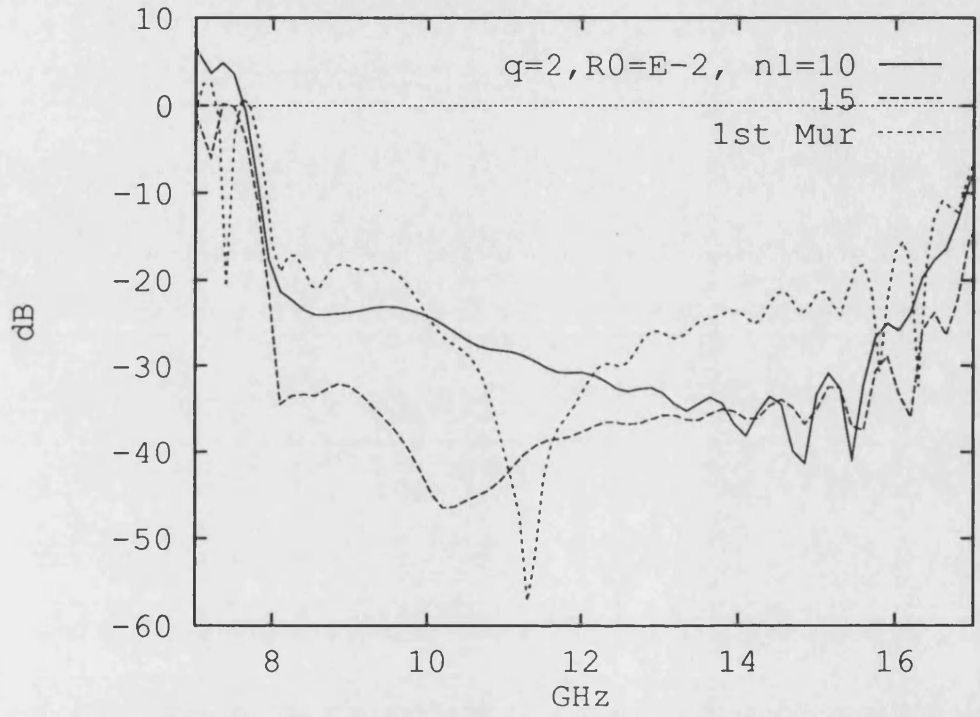

Figure 5.29: Reflection Coefficient (R.C.) at z=350 mm due to implementing ABCs at the end of the rectangular waveguide (z = 550 mm) for PML ABC when q=2, $R(0)$=10^{-2} and nl=10 and 15 with 1st Mur ABC.

frequency. Although for the PML *nl* can be increased in order to decrease the R.C. around the centre frequency, economy considerations for for CPU time and computer memory can prevent such an increase. Regarding these limitations and results of these sections, 1st order Mur ABC is selected for analysing the IDG discontinuities in the next chapter.

In this chapter, by implementing the FDTD technique in a rectangular waveguide many important points are demonstrated. First the code of this method is tested. Second there is an opportunity to implement the 1st order Mur, the PML ABC, and the boundary conditions of the structure. Third, which in the opinion of the author is an important point in this research, is the excitation method. This supplies four field components, by the inverse Fourier transform as a function of distance for the initiation of the FDTD analysis. The work described in this chapter gives great experience to the author to implement the FDTD technique in analyses of IDG discontinuities which is fulfilled in the next chapter.

Comparison with numerical results and analytical formulations shows that the implementation of the FDTD method in rectangular wave guide is correct. For example numerical results show that for any time step in running the analysis, variation of the three main components E_x, H_y, and H_z follows the analytic formulations (Eqs. 5.9, 5.12, and 5.15 respectively) and the other three components are zero.

Chapter 6

Analysis of IDG Discontinuity Caused by a Metal Obstacle

6.1 Outline

In this chapter a discontinuity caused by a metal obstacle normal to the guide is investigated by the FDTD method. This analysis is the fundamental stage in the analyses of IDG discontinuities such as a step in dielectric, step in IDG depth, step in width, etc, which have not been examined before. Also it leads to the analysis of filters and transformers. In this analysis, to limit the volume of computation, 1st order Mur's ABC is used for both ends and the upper side of the guide. The mode of propagation is approximately HE_{01} which is the dominant mode in this guide. This mode is approximately produced by the TE odd mode (TE_{odd}) of the dielectric slab waveguide for the deep slot type of the guide. The method of excitation is based on what was described in Chapter 5 in rectangular waveguide for the TE_{10} mode. It means that the three main components of the TE_{odd} mode for the first time step are produced as a function of distance which is detailed in Section 6.5. In this analysis a metal obstacle is mounted in the

guide on the transverse plane. By the FDTD method reflection and transmission coefficients of this discontinuity are computed while the height of the obstacle is varied and the results are compared with measurements.

6.2 IDG Structure

Figure 6.1 shows the IDG structure and coordinates x, y, and z. Its dimensions are $a = n2\delta$, $b = n1\delta$ (δ is cell size). The length of the line is $L = n3\delta$ and position of the metal obstacle is $zd = kd\delta$ and its height is $hd{=}id\delta$ (Fig. 6.2). The slot is fully filled by dielectric whose relative permittivity is ϵ_r.

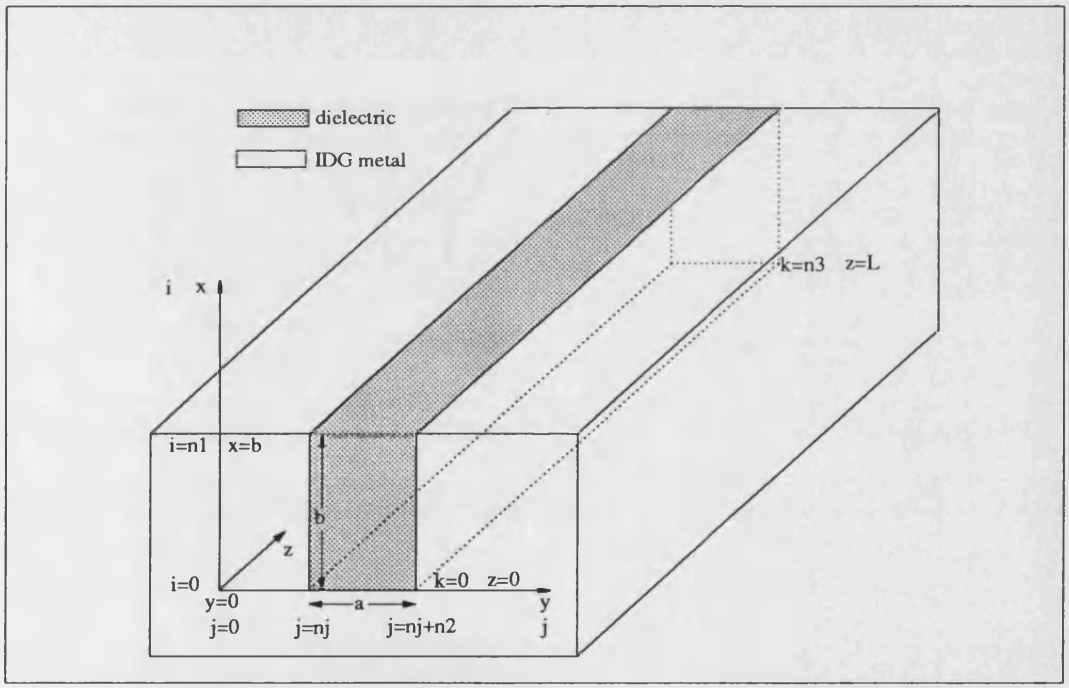

Figure 6.1: IDG structure.

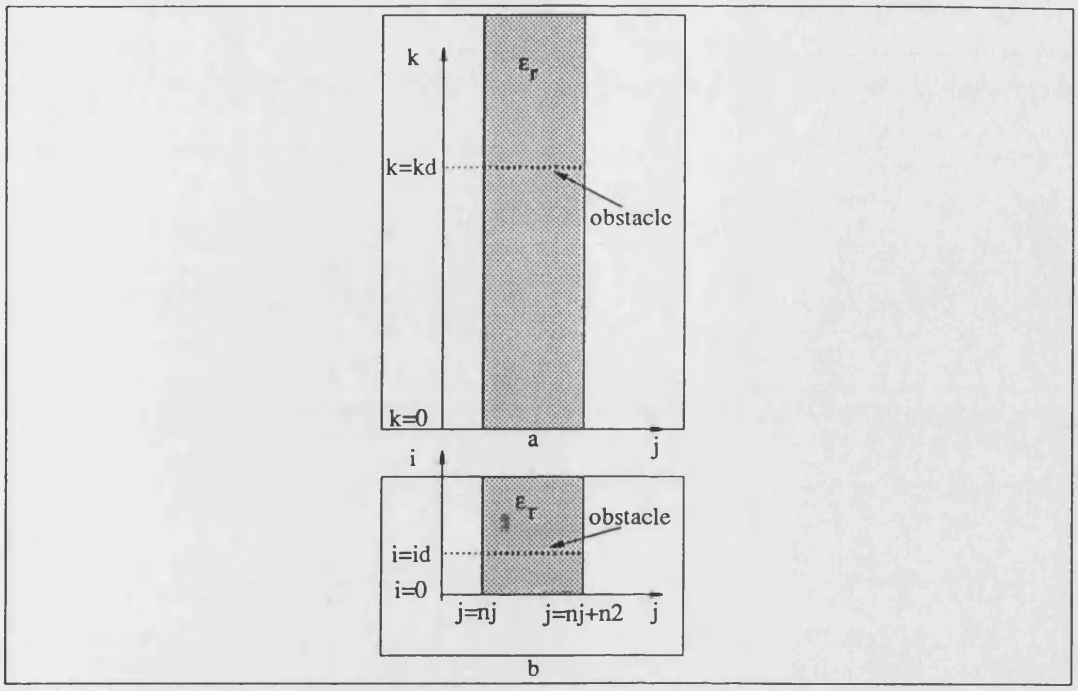

Figure 6.2: Position of the obstacle in the guide a)top view b)front view.

6.3 Dominant Mode in IDG

The dominant mode in IDG is HE_{01} [7]. The cut-off frequency for this mode for the deep slot with dimension a= 1.016 cm and b=1.524 cm with ϵ_r=2.08 is about 5 GHz and the cut-off frequency for the second mode of propagation (HE_{02}) is about 14 GHz. Therefore the centre frequency for the analysis f_o=9.5 GHz and frequency bandwidth BW_f=6 GHz are chosen.

6.4 Approximation of the Dominant Mode

The dominant mode of the IDG is approximated by the TE odd mode of the slab dielectric waveguide (TE_{odd}) which is described in this section.

Figure 6.3 shows a dielectric slab waveguide which is a uniform dielectric sheet

and infinite in the y and z directions. It has uniform thickness $2b$ in the x direction whose refractive index is n_r ($n_r = \sqrt{\epsilon_r}$). This sheet is surrounded by air. Fig. 6.3 also shows view of the IDG in which fields will be approximately the same as half of the slab for the TE_{odd} slab mode.

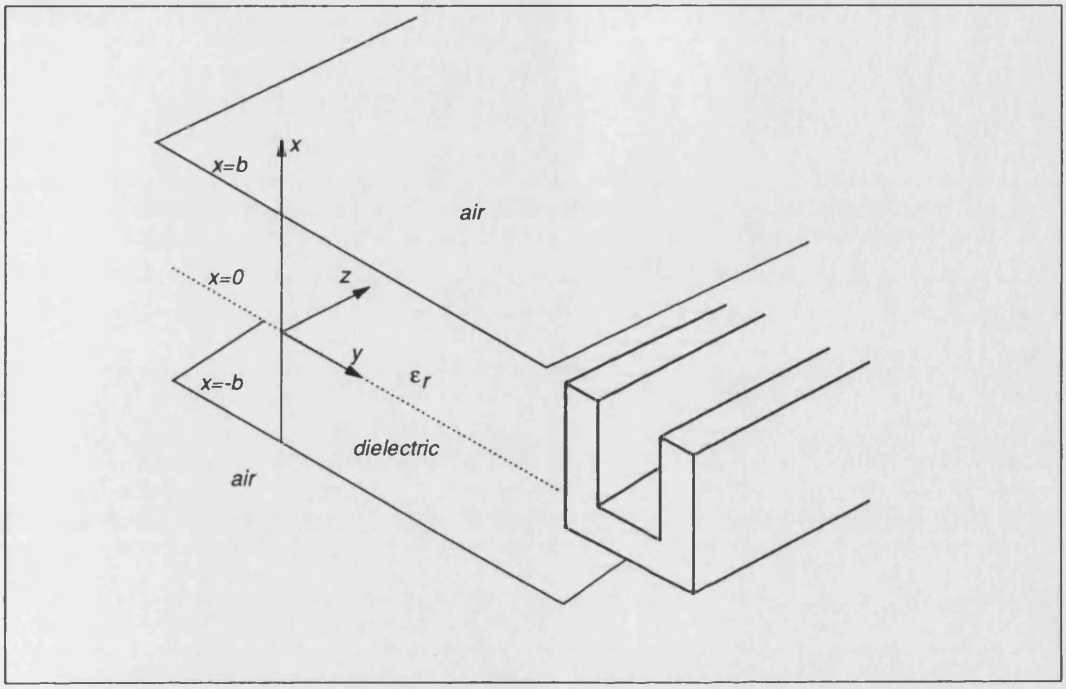

Figure 6.3: The dielectric slab waveguide and the IDG in which TE_{odd} mode of the slab is approximated .

The dielectric slab for the case of total internal reflection has four types of guided modes of propagation which are TE (odd, even) and TM (odd, even) [67]. All these guided modes have an exponentially decay in air with respect to x. E_y in the TE mode (or H_y in TM mode) in the dielectric has variation as a sine function with respect to x for the odd modes and has a cosine function with respect to x for the even modes. Because of the boundary conditions on the metal walls of the IDG which are at i=0, $j = nj$, and $j = n2 + nj$ (Fig. 6.1), TE odd (TE_{odd}) mode with field components E_y, H_x, and H_z of the dielectric slab waveguide is applicable to approximate the dominant mode in IDG. This mode for deep slot IDG is similar to the TE_{01} mode of the rectangular waveguide.

Field Solution:

The ν and ϕ as defined in the Eqs. 6.1 and 6.2 which are obtained from the dispersion relation [67, Eqs. 6.78, 6.79] in the dielectric and air:

$$k^2 - \beta^2 = \nu^2 \tag{6.1}$$

$$k_0^2 - \beta^2 = \phi^2 \tag{6.2}$$

where β is propagation constant in z direction in both air and dielectric and $k_0 = \omega^2\mu_0\epsilon_0$ and $k^2 = \omega^2\mu_0\epsilon = (k_o n_r)^2$. To have a decaying field in the air $\phi^2 \leq 0$ ($\phi^2 = -\xi^2$, $\xi^2 \geq 0$). Also to have field variation with respect to x in the dielectric $\nu^2 \geq 0$, therefore in this situation the field components of the TE_{odd} mode in the IDG are:

$$E_y = Asin(\nu x) \quad b \geq x \geq 0 \quad (in\ dielectric) \tag{6.3}$$

$$E_{y0} = Be^{-\xi(x-b)} \quad x \geq b \quad (in\ air) \tag{6.4}$$

For the reason of brevity the common $e^{(j\omega t - j\beta z)}$ factor is omitted.

Field continuity at the boundary $x = b$ ($E_y = E_{y0}$ at $x = b$) requires that $B = Asin(\nu b)$. By expanding Maxwell's Equation $\nabla \times \vec{E} = -j\omega\mu\vec{H}$ and considering $\frac{\partial}{\partial y}$=0 and $\frac{\partial}{\partial z} = -j\beta$, the two other field components are:

$$H_x = -\frac{A\beta}{\omega\mu_0} sin(\nu x) \quad b \geq x \geq 0 \tag{6.5}$$

$$H_{x0} = -\frac{A\beta}{\omega\mu_0} sin(\nu b)e^{-\xi(x-b)} \quad x \geq b \tag{6.6}$$

$$H_z = -\frac{A\nu}{j\omega\mu_0} cos(\nu x) \quad b \geq x \geq 0 \tag{6.7}$$

$$H_{z0} = \frac{\xi A}{j\omega\mu_0} sin(\nu b)e^{-\xi(x-b)} \quad x \geq b \tag{6.8}$$

Field continuity requires that at $x = b$, $H_z = H_{z0}$ therefore:

$$\nu cos(\nu b) = -\xi sin(\nu b) \tag{6.9}$$

By definition:

$$u = \nu b \tag{6.10}$$

$$w = \xi b \tag{6.11}$$

one of the main equations in this case is:

$$ucot(u) = -w \tag{6.12}$$

by eliminating β from Eqs. 6.1 and 6.2, the second main equation is:

$$u^2 + w^2 = p^2 \tag{6.13}$$

where:

$$p^2 = \omega^2 \mu_0 \epsilon_0 d^2 (n_r^2 - 1) \tag{6.14}$$

By solving the two Eqs. 6.12 and 6.13 numerically (by Newton-Raphson method) the values of ξ, ν, and β are obtained for the centre frequency f_o=9.5 GHz. All these value are needed for the FDTD code as the input data to complete the initiation of the three components E_y, H_x, and H_z for the first time step (n=0). The value of β is also needed for the inverse Fourier transform code for the excitation stage.

6.5 Excitation

When the analysis is started using the FDTD method for the first time step (n=0), based on Eqs. 3.11-3.16 the values of the $E_y^0(i,j,k)$, $E_y^0(i,j,k+1)$, $H_x^{-\frac{1}{2}}(i,j,k)$, and $H_z^{-\frac{1}{2}}(i,j,k)$ (for the TE mode) are needed both in the air

and in the dielectric as the initiation values. These values are produced as a function of distance by the procedure used in Chapter 5.

First $E_y(t)$ is written analytically by $sin(2\pi f_o t)$ modulated by a Gaussian pulse shifted to $t = t_f$ (Fig. 5.3) The factor $sin(\nu x)$ will be considered in the FDTD code therefore if $E_y(t) = E'_y(t)sin(\nu x)$, the relation for $E'_y(t)$ is:

$$E'_y(t) = A_1 e^{-(\frac{t-t_f}{y_p})^2} e^{j2\pi f_o t} \tag{6.15}$$

its discretised form is:

$$E'_y(n\Delta t) = A_1 e^{-(\frac{n\Delta t - t_p \Delta t}{y\Delta t})^2} e^{j2\pi f_o n\Delta t} \tag{6.16}$$

its Fourier transform is:

$$E'_y(f) = A_1\sqrt{\pi} y_p e^{-\pi^2 y_p^2 (f-f_o)^2} e^{-j2\pi t_f (f-f_o)} \tag{6.17}$$

and its magnitude is:

$$\left|E'_y(f)\right| = A_1\sqrt{\pi} y_p e^{-\pi^2 y_p^2 (f-f_o)^2} \tag{6.18}$$

When the frequency is discretised ($f = ndf$):

$$\left|E'_y(ndf)\right| = A_1\sqrt{\pi} y_p e^{-\pi^2 y_p^2 (ndf-f_o)^2} \tag{6.19}$$

$E'_y(ndf)$ is used for deriving the Fourier transform of the components H_x, and H_z regarding Eqs. 6.5 and 6.8.

Referring to Eqs. 3.11-3.16 and Yee's mesh in Fig. 3.1, here there are also two kinds of offset. First an offset in space for H_x which is $\frac{\delta}{2}$ leading in the z direction in respect to E_y which is imposed by multiplication of $H_x(f)$ by $e^{-j\beta\frac{\delta}{2}}$. This factor for $E_y^0(i,j,k+1)$ is $e^{-j\beta\delta}$. The value of β is derived by solving the two Eqs. 6.12 and 6.13 numerically. The second offset is a half time step ($\frac{\Delta t}{2}$) for H_x and H_z which are lagging in comparison with E_y. To impose this kind of offset the procedure is similar to section 5.4.

The inverse Fourier transform produces the four components $E_y^0(i,j,k)$, $E_y^0(i,j,k+1)$, $H_x^{-\frac{1}{2}}(i,j,k)$, and $H_z^{-\frac{1}{2}}(i,j,k)$ as a function of distance. They are the input to the FDTD analysis. After that, for this analysis the components relevant to the air (E_{y0}, H_{x0}, and H_{z0}) are produced by considering the factors $e^{-\xi(x-b)}$, $sin(\nu x)$, and $cos(\nu x)$.

6.6 Absorbing Boundary Condition

Because the IDG is an open structure, in this analysis ABCs are needed for the two ends (k=0 and k=n3) and upper side of the guide. In the case of using the PML ABC, the simulation needs much more computer memory. If the PML ABC is used with nl=15 instead of the 1st order Mur's ABC, for the present analysis, the extra calculation points needed is about 14,000,000 (extra cells is 1,173,000). The necessary number calculation points for the main volume of the structure are 4,620,000 (770,000 cells). Therefore using the PML ABC increases the number of calculation points by more than 400 percent. The necessary computer memory for the field components for the main volume is about 37 Mbytes and for the field components in the PML media is about 113 Mbytes. Computer time for running the analysis in the case of using the PML takes four times more than using 1st order Mur's ABC. These values are for the full analysis of structure and are halved when half the structure is considered. On the other hand, for having a single mode of propagation the required bandwidth of frequency is not large. Therefore, because of these two points and ease of implementation, 1st order Mur's ABC is chosen and the results of analysis shows that this ABC is sufficient.

Figure 6.4 shows the cross section of the upper side ABC. The position of this ABC has to be far enough from centre of the guide so that it does not absorb the main fields of the guide. Its dimensions (nj and ni) have been found experimen-

tally in this research and the result is ni=25 and nj=20.

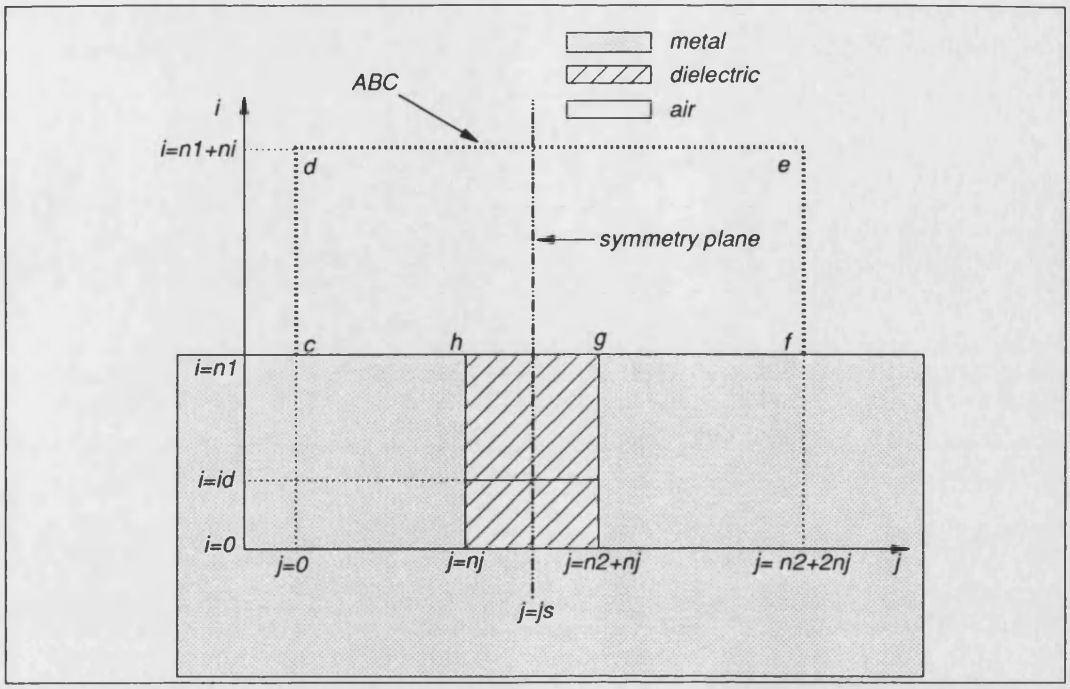

Figure 6.4: Cross section of the upper ABC of the guide and position of the metal obstacle inside the guide.

To implement the 1st order Mur's ABC at boundary cd (j=0) Eq. 4.15 is imposed (like k=0) on E_x and E_z. For boundary de ($i = n1 + ni$) Eq. 4.17 is imposed on E_y and E_z (like k=$n3$). For boundary ef Eq. 4.17 is imposed on E_x and E_z (like k=$n3$).

During the analysis E_x and E_z at j=0 and at $j = n2 + 2nj$ also E_y and E_z at $i = n1 + ni$ are not calculated by the FDTD formulation because they are calculated by the ABC.

6.7 The FDTD Implementation and Boundary Conditions

In this analysis, for simplicity, $\Delta x = \Delta y = \Delta z = \delta$ is imposed. δ is chosen so that it is much smaller than the smallest wavelength in the propagating frequencies. On the other hand it is chosen so that, regarding the dimension of the IDG (a and b), $n2$ even and integer cells along j direction and $n1$ integer cells along i direction will exist. An integer number of cells $n3$ is used for the length of the guide along the k direction, therefore the length of the guide is $L = n3\delta$.

The guide is fully filled by dielectric (ϵ_r), The upper side of the guide is air. At $k = kd$ ($z = kd\delta$) there is a metal obstacle which extends up to $i = id$ in the i direction and its height is $id\delta$. In the present research id is varied from 0 to $n1$.

Tangential electric field (E_n) and normal magnetic field (H_n) on the plane i=0 ($nj \leq j \leq nj + n2$), $j = nj$ ($i \leq n1$), $j = nj + n2$ ($i \leq n1$), and $i = n1$ ($j \leq nj$ and $j \geq nj + n2$) are zero because they are metal walls. E_n and H_n are also zero on the metal obstacle ($0 \leq i \leq id$, $nj \leq j \leq nj + n2$, and k=kd). The FDTD formulation does not calculate these components (E_n and H_n) at the relevant planes. Also the calculation does not proceed in the IDG metal. Because in this region the fields are enforced to be zero.

During the process of the FDTD formulation, the factor α_E must be changed and calculated in the air by $\epsilon = \epsilon_0$, in the dielectric region by $\epsilon = \epsilon_r\epsilon_0$. For any electric field located on the interface of the air and dielectric regions (boundary hg in Fig. 6.4) regarding Yee's mesh in Fig. 3.1 this factor must be calculated by the average of the two permittivities ($\epsilon = (\frac{\epsilon_r+1}{2})\epsilon_0$) [32].

6.8 Running the FDTD Analysis

With the boundary conditions described in the last section and the input data which are mentioned in the next section the FDTD code is run. For saving time and computer memory the analysis can be performed for the half of the structure and j instead of starting zero can be started from $j = js$ (Fig 6.4). In this case referring to the Eqs. 3.11-3.16 the values of the H_x and H_z must be determined. Regarding the TE_{odd} mode it can be concluded that:

$H_x^{n+\frac{1}{2}}(i, js-1, k)$=$H_x^{n+\frac{1}{2}}(i, js, k)$ and

$H_z^{n+\frac{1}{2}}(i, js-1, k)$=$H_z^{n+\frac{1}{2}}(i, js, k)$

6.8.1 Input Data

Table 6.1 shows the input data which are not changed during the analysis. In this table $zd = kd\delta$ is the position of the obstacle in the z direction, tnp is the total number of points picked up from $E_y(f)$, mnt is the maximum of number of time steps for runing the analysis, and t_f is the shifting of the peak of the Gaussian pulse (Fig. 5.3).

The other input data which are variable during the analysis are:

1-$hd = id\delta$ is the height of the obstacle.

2- The monitor point is $M(xm, ym, zm)$, where $xm = im\delta$, $ym = jm\delta$, and $zm = km\delta$. To present the results of this analysis ym is $jm\delta$=25δ=25.4 mm at the symmetry plane ($jm = js = 25$) and there are three monitor points in the transverse plane which are:

$M1(8\delta = 8.128mm,\ 25\delta = 25.4mm)$,

$M2(14\delta = 14.224mm,\ 25\delta = 25.4mm)$, and

$M3(18\delta = 18.288mm,\ 25\delta = 25.4mm)$.

The positions of the monitor points in the z direction are in Table 6.2.

Table 6.1 :*Input data*

f_o (MHz)	BW_f (MHz)	ϵ_r	k_s	δ (mm)	a (cm)	b (cm)	L (cm)	zd (cm)
9.5	6	2.08	0.4	1.016	1.016	1.524	55.88	30.48

tnp	mnt	t_f
3000	4000	100

Table 6.2 : *Position of the monitor points in the z direction.*

position	$zm1$	$zm2$	$zm3$	$zm4$	$zm5$	$zm6$	$zm7$
no. of cells(km)	180	360	400	440	480	520	540
distance(mm)	182.88	365.76	406.4	447.04	487.68	528.32	548.46

6.8.2 Computations Derived From Input Data

Table 6.3 shows the parameters computed from the input data.

Table 6.3 :*Parameters derived from input data.*

ν rad/m	ξ rad/m	β rad/m	k_o rad/m	v m/sec	v_p m/sec	v_g m/sec
152.0	140.3	243.6	199.1	2.0801×10^8	2.4503×10^8	1.7659×10^8

$n1$	$n2$	$n3$	kd
15	10	550	300

and Table 6.4 shows computed parameters relevant to the inverse Fourier transform.

Table 6.4 :*Parameters relevant to the inverse Fourier transform.*

BW'_f (GHz)	BW'_t $(psec)$	BW'_s (cm)	c_f
8.3258	152.928	2.7	1.3876

Parameters of Table 6.4 are computed by Eqs. 5.26 and 5.29. Δt=1.3547 *psec* is computed from Eq. 3.22 where k_s=0.4 and $v = c$ are considered.

6.8.3 Computed Results and Measurements

In this section results of the analysis with the above mentioned input data are presented. The discontinuity is a metal obstacle located normal to the z direction at $z = zd$=304.8 *mm*.

Figure 6.5 shows magnitude of the Fourier transform of E_y and H_x. $H_z(f)$ is similar to $H_x(f)$ multiplied by the constant factor $\frac{\nu}{\beta}$ (Eqs. 6.5 and 6.7).

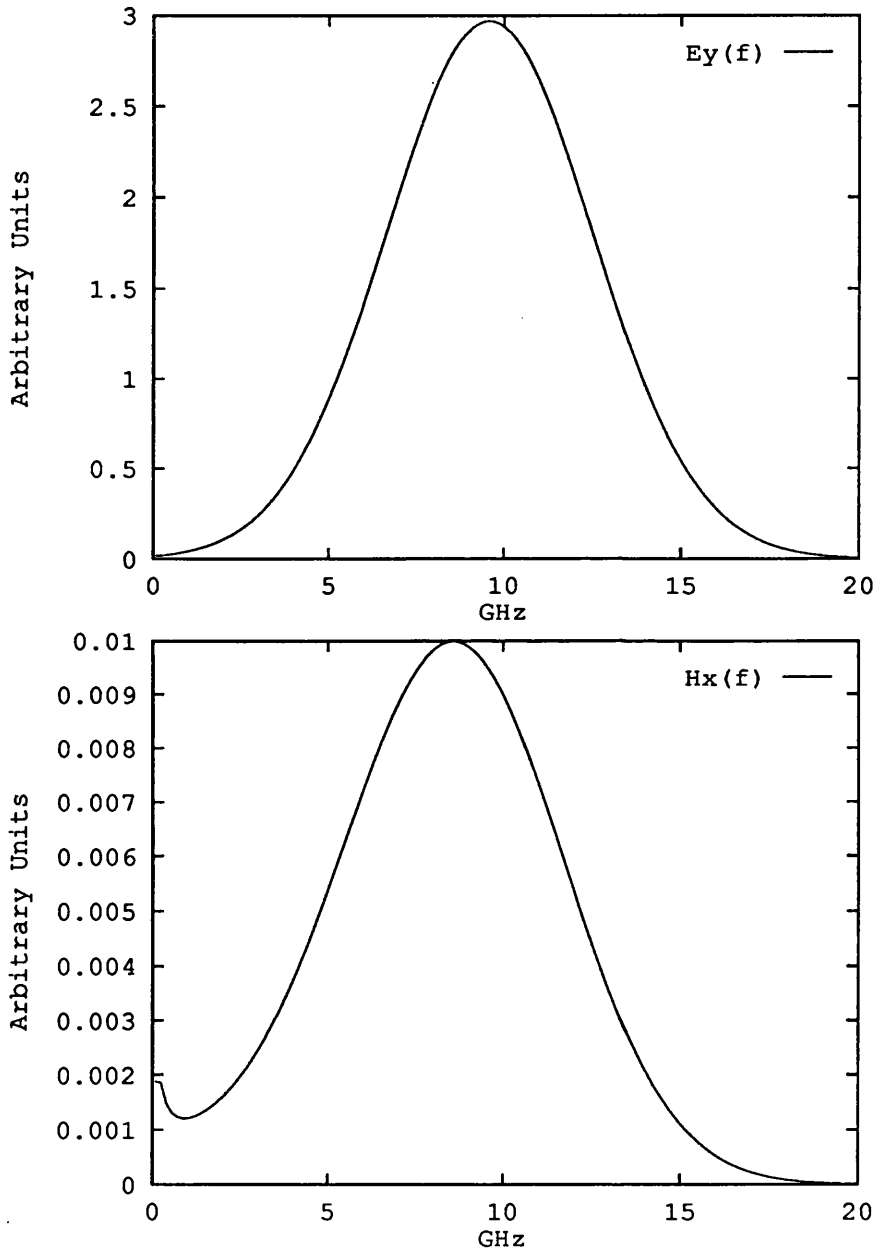

Figure 6.5: Magnitude of the Fourier transform of the E_y and H_x.

Figure 6.6 shows incident and reflected pulses of Ey as a function of time at monitor point $M1$(8.128 mm, 25.4 mm) and $zm1$=182.88 mm for three different heights of the obstacle which is located at z=zd=304.8 mm. It shows that when the height of the obstacle is increased, the amplitude of the reflected pulse will increase. In this case the amplitude of the transmitted pulse will decrease. Figure 6.7 shows this matter where the monitor point in the z direction is $zm4$=440 mm which is after the position of the obstacle (zd).

Figure 6.8 shows $E_y(t)$ as a function of time for three different transverse monitor points $M1$(8.128 mm, 25.4 mm) $M2$(14.224 mm, 25.4 mm), and $M3$(18.288 mm, 25.4 mm) and $zm1$=182.88mm while the height of the obstacle is kept at hd=10.16 mm. The amplitude of the pulses are changed because they are a function of x (Eqs. 6.3 and 6.4).

Figure 6.9 shows the Fourier Transform (F.T.) of the Incident Pulse (I.P.), Reflected Pulse (R.P.), and Reflection Coefficient (R.C.) at monitor point $M1$(8.128 mm, 25.4 mm) and $zm1$=182.88 mm where the height of the obstacle is hd=10.16 mm and its position is zd=304.8 mm. This figure confirms the proper centre frequency f_o=9.5 GHz and frequency bandwidth BW_f=6 GHz.

Figure 6.10 shows F.T. of the Transmitted Pulses (T.P.) and Transmission Coefficient (T.C.) at different monitor points in the z direction zm = $zm2$=365.76 mm to $zm7$=548.46 mm and same monitor point at transverse plane $M1$(8.128 mm, 25.4 mm), while the height of the obstacle is hd=10.16 mm and its position is zd=304.8 mm. This figure shows that there is a good consistency for centre and lower band of propagating frequency and for the upper band there is no good consistency.

This phenomena may be because of the scattering of the waves due to existence of the obstacle for higher frequencies of the propagating frequency band. Excess electric charges on the sharp edge of the metal obstacle may change the regular

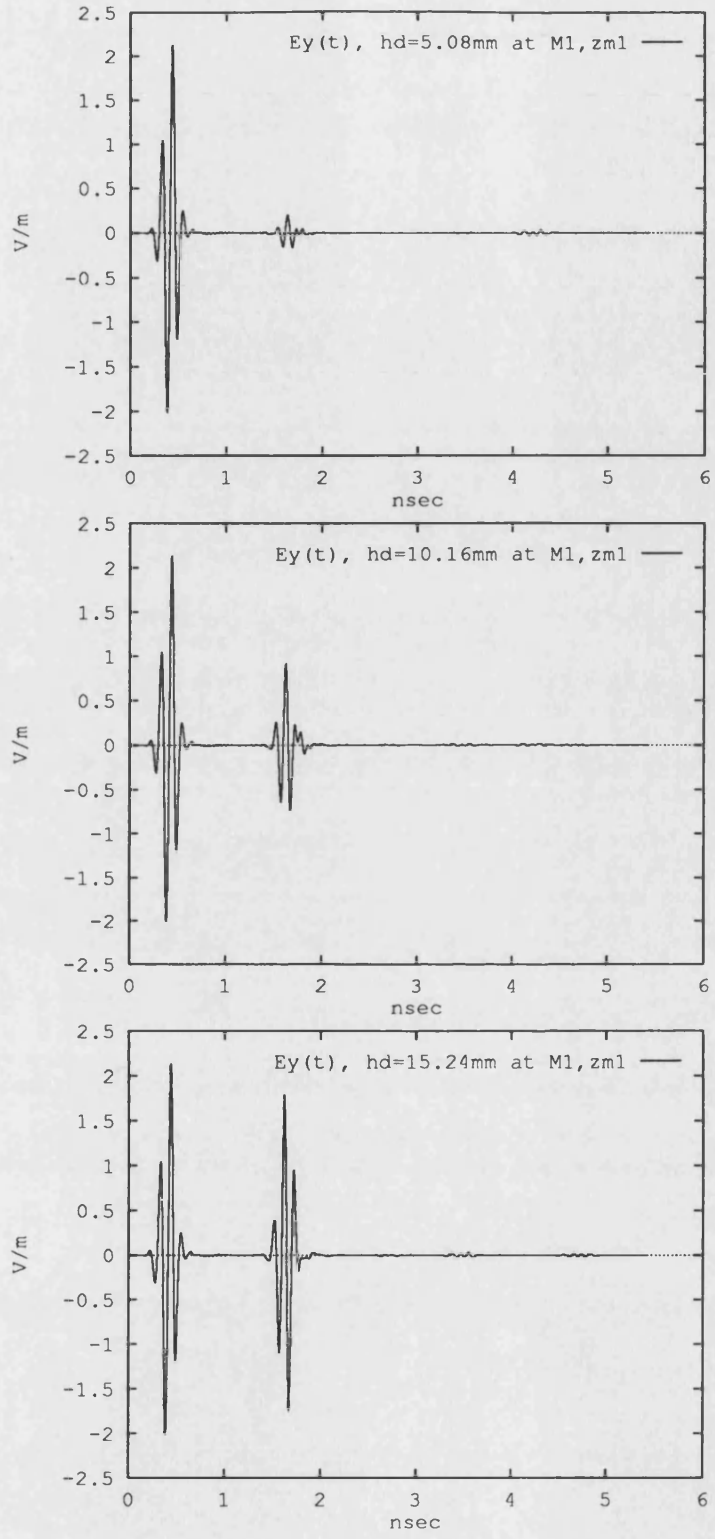

Figure 6.6: E_y as a function of time for three different heights of the obstacle (hd) at same monitor point $M1(8.128\ mm, 25.4\ mm)$ and $zm1$=182.88 mm. Position of the obstacle is at zd=304.8 mm.

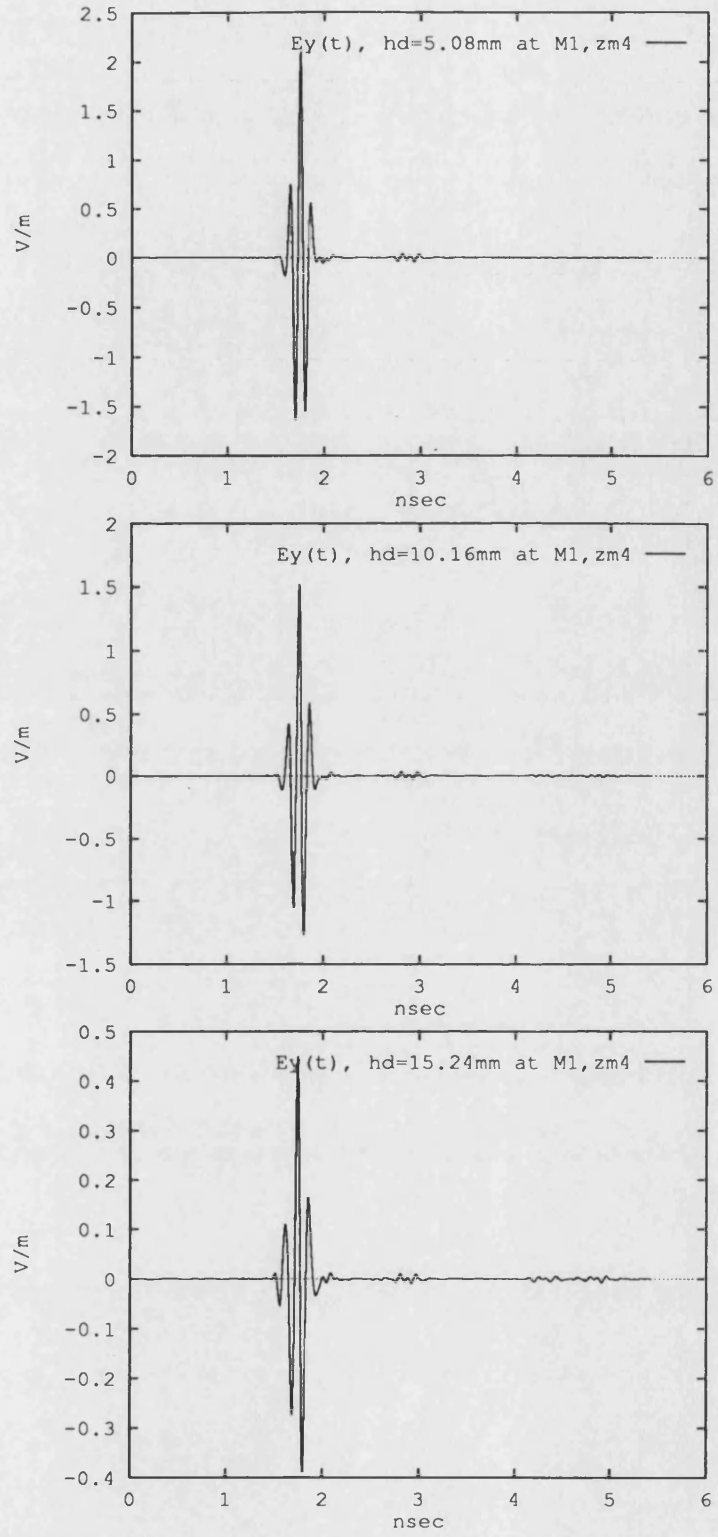

Figure 6.7: E_y as a function of time for three different heights of the obstacle (hd) at same monitor point $M1(8.128\ mm, 25.4\ mm)$ and $zm4$=440 mm. Position of the obstacle is at zd=304.8 mm.

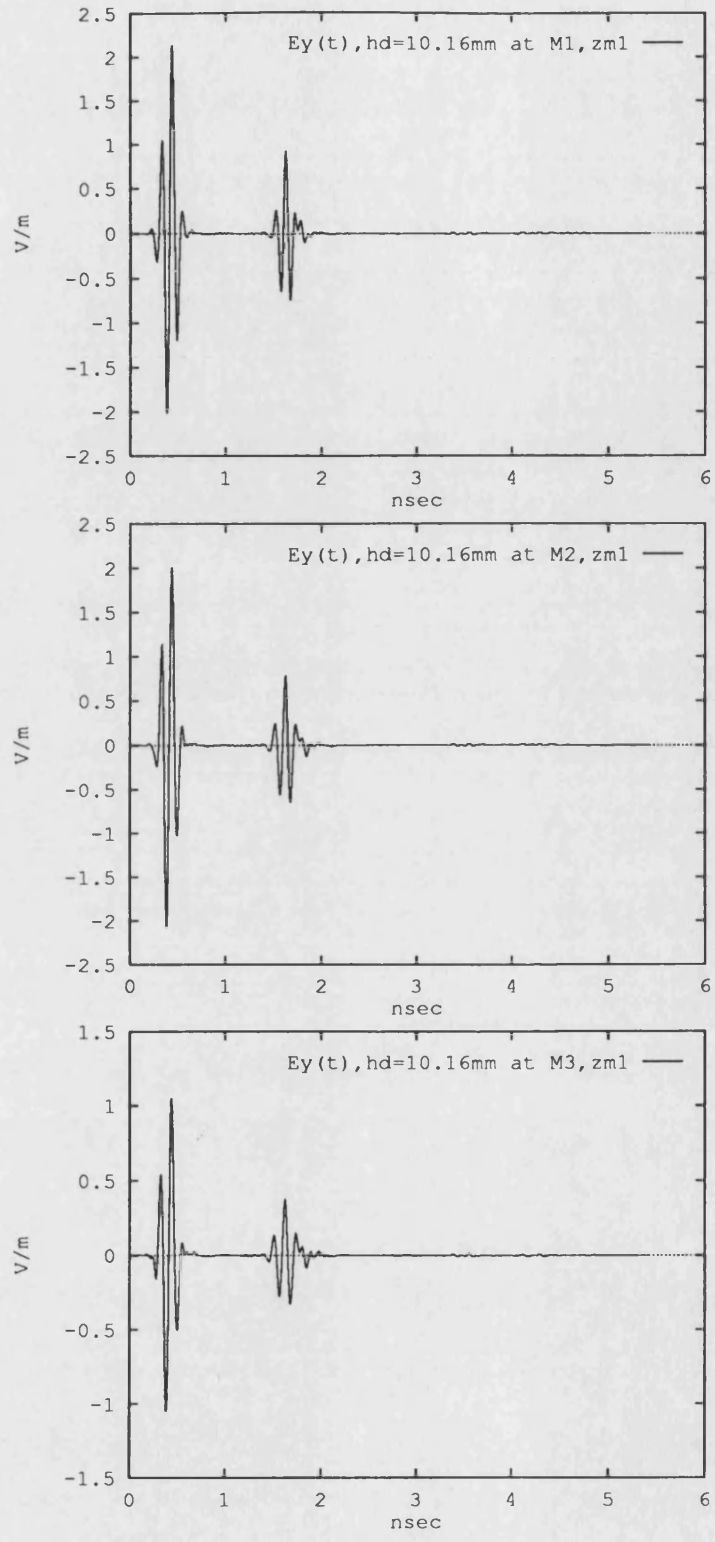

Figure 6.8: E_y as a function of time for three different transverse monitor points $M1$(8.128 mm, 25.4 mm) $M2$(14.224 mm, 25.4 mm), and $M3$(18.288 mm, 25.4 mm) and $zm1$=182.88mm, while the height of the obstacle is kept hd=10.16 mm and its position is zd=304.8 mm.

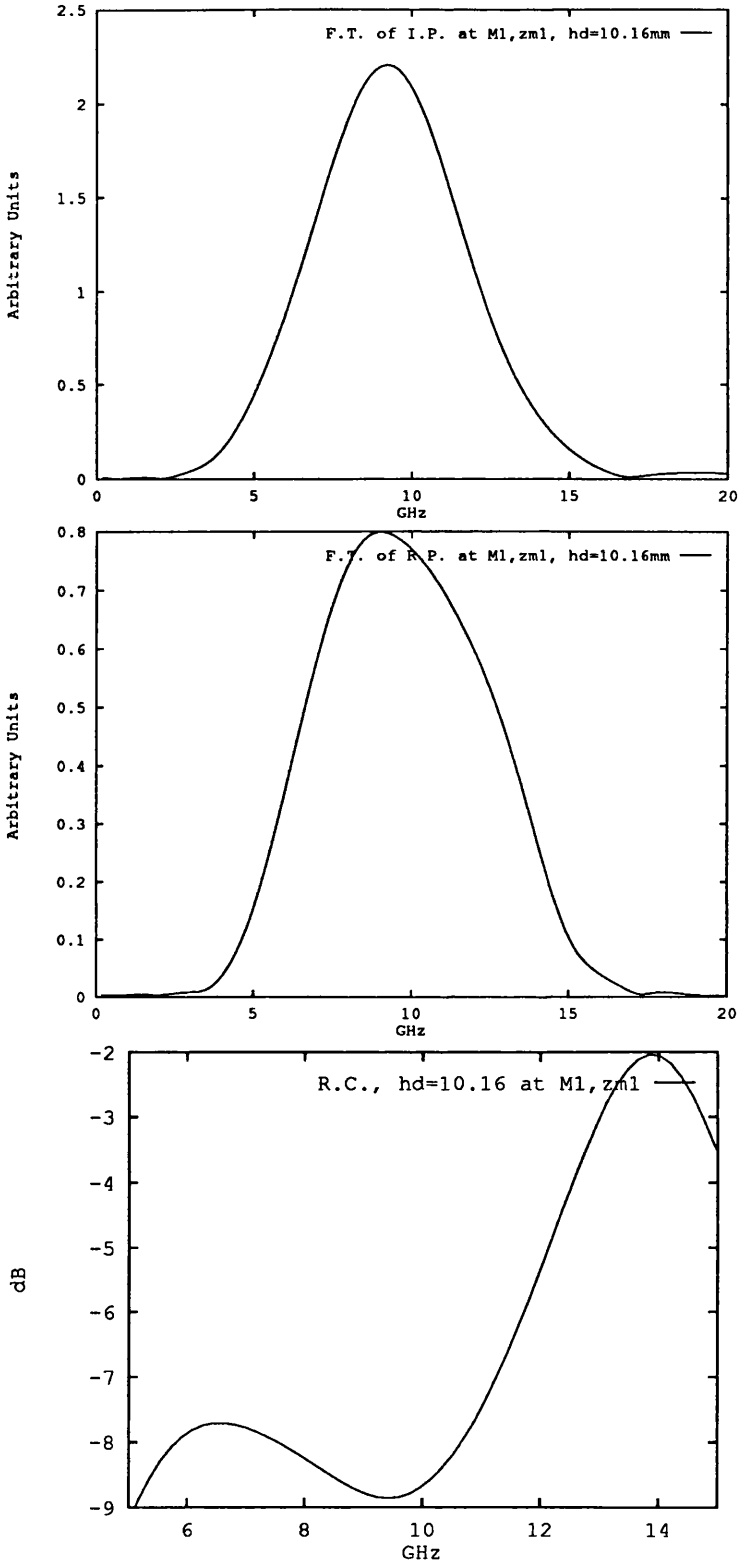

Figure 6.9: Fourier Transform (F.T.) of the Incident Pulse (I.P.), Reflected Pulse (R.P.), and Reflection Coefficient (R.C.) at monitor point $M1$(8.128 mm, 25.4 mm) and $zm1$=182.88 mm where the height of the obstacle is hd=10.16 mm and its position is zd=304.8 mm.

distribution of the fields and caused this phenomena.

Figure 6.11 is similar to Fig. 6.10 but it shows the power loss (P_{loss}). P_{loss} in a two port structure is:

$$P_{loss} = 1 - |S11|^2 - |S21|^2 \tag{6.20}$$

where $S21$ is R.C. and $S12$ is T.C. This figure confirms the consistency of the Fig. 6.10.

Figures 6.12, 6.13, and 6.14 show R.C., T.C., and P_{loss} respectively due to the obstacle with different heights (hd) which is varying from hd= 5.080mm to hd=14.224 mm. The monitor point in the transverse plane for all is $M1$(8.128 mm, 25.4 mm) but in the z direction for R.C. is $zm1$=182.88 mm and for T.C. and P_{loss} is $zm4$=447.04 mm. The position of the obstacle is zd=304.8 mm. As expected when the height of the obstacle is increased the R.C. will increase and T.C. will decrease. Figure 6.14 shows by increasing the height of the obstacle P_{loss} is increases up to about 11.176 mm after that p_{loss} will decrease.

Measurement

To investigate the agreement between computed results (reflection and transmission coefficients) and measurement a circuit mainly consisting of a network analyser and IDG with a metal obstacle has been constructed. The dimensions of the guide and permittivity of the dielectric (a, b, and ϵ_r) are given in Table 6.1. The network analyser is a vector network analyser which measures magnitude and phase of reflection and transmission coefficients of the component under test. Calibration which is establishment of zero level of both magnitude and phase of reference point (position of the obstacle) is carried out with the TRL (Thru-Reflect-Line) technique. In this technique, two short circuits are located at the reference point towards each port and a piece of the spare IDG with known length is used. By this calibration some errors such as radiation from rectangular

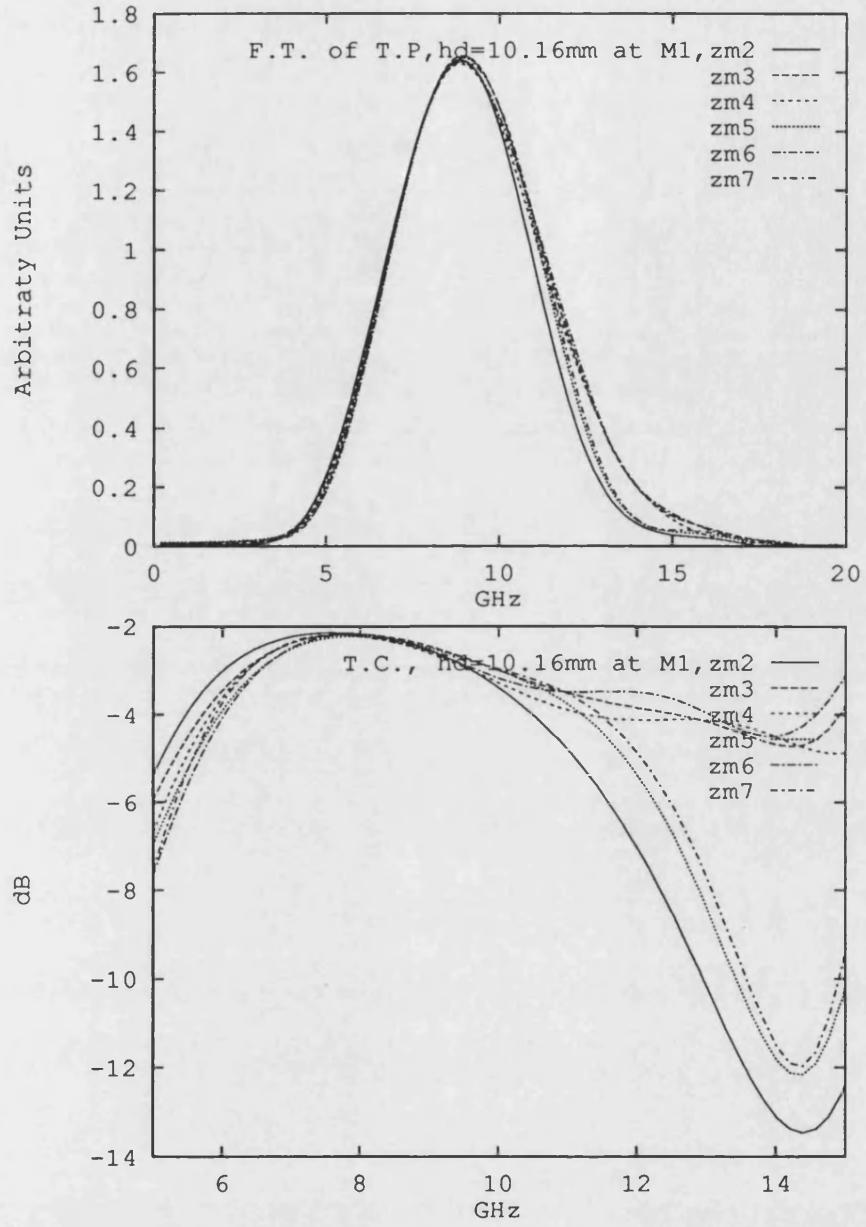

Figure 6.10: F.T. of the Transmitted Pulses (T.P.) and Transmission Coefficient (T.C.) at different monitor point in the z direction $zm = zm2$=365.76 mm to $zm7$=548.46 mm and same monitor point at transverse plane $M1$(8.128 mm, 25.4 mm), while the height of the obstacle is hd=10.16 mm and its position is zd=304.8 mm. In the calculation of T.C. $zm1$ is the reference point.

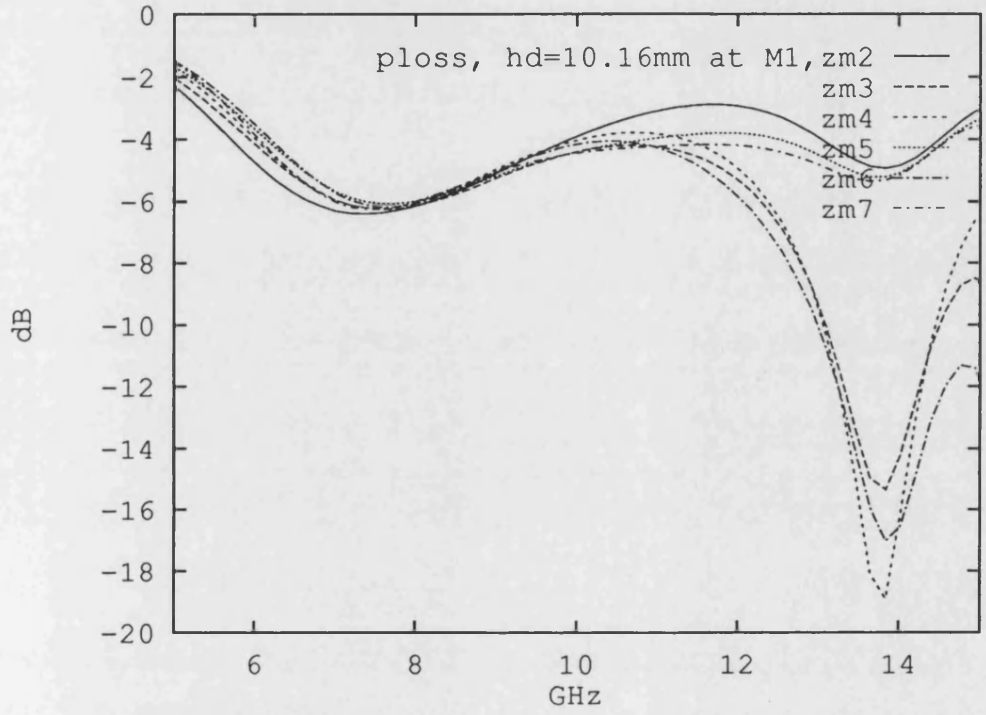

Figure 6.11: P_{loss} at different monitor points in the z direction $zm = zm2$=365.76 mm to $zm7$=548.46 mm and same monitor point at transverse plane $M1$(8.128 mm, 25.4 mm), while the height of the obstacle is hd=10.16 mm and its position is zd=304.8 mm. In the calculation of P_{loss} $zm1$ is the reference point.

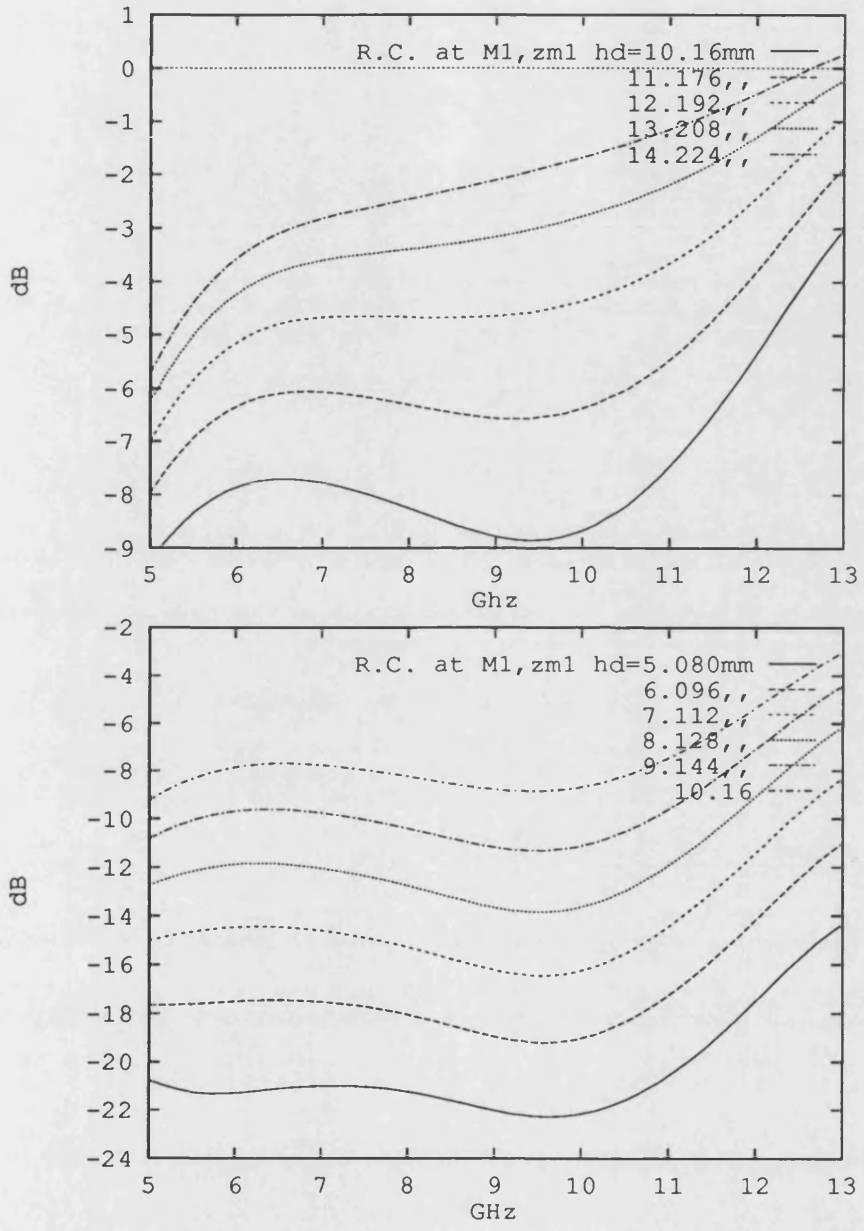

Figure 6.12: Reflection Coefficients (R.C.) of the line because of the obstacle with different heights (hd) where monitor point is $M1(8.128\ mm, 25.4\ mm)$ and $zm1$=182.88 mm . Position of the obstacle is zd=304.8 mm.

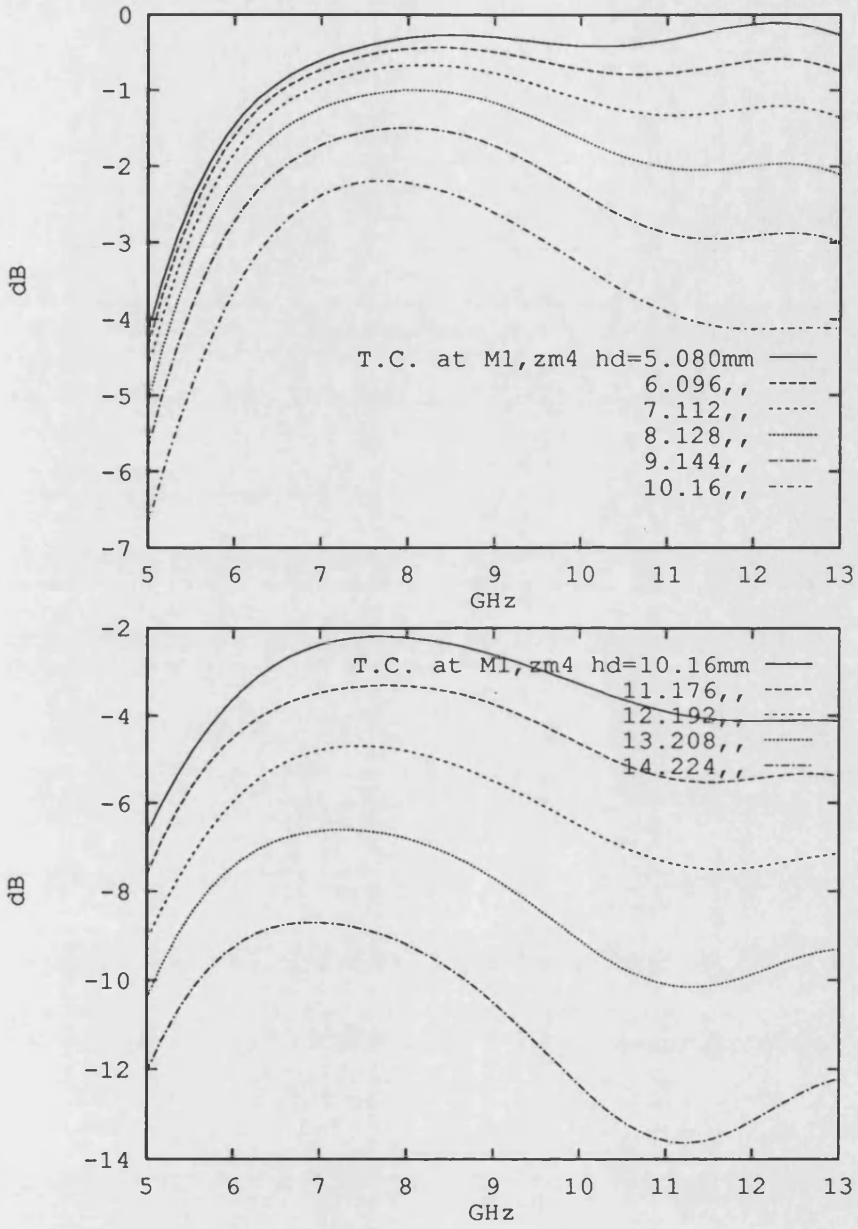

Figure 6.13: Transmission Coefficients (T.C.) of the line because of the obstacle with different heights hd where monitor point is $M1(8.128\ mm,\ 25.4\ mm)$ and $zm4$=447.04 mm . Position of the obstacle is zd=304.8 mm. In the calculation of T.C. $zm1$ is the reference point.

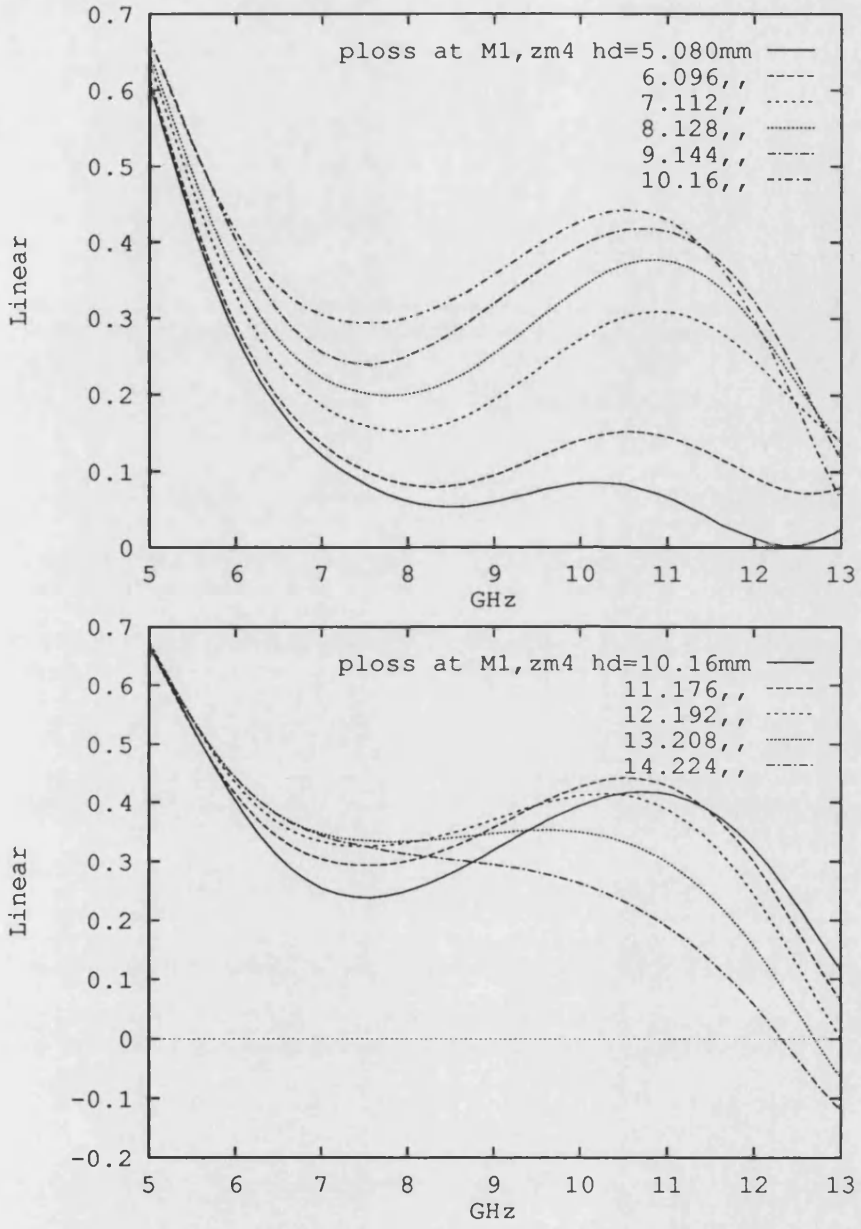

Figure 6.14: P_{loss} of the line because of the obstacle with different heights hd where monitor point is $M1(8.128\ mm, 25.4\ mm)$ and $zm4$=447.04 mm . Position of the obstacle is zd=304.8 mm. In the calculation of P_{loss} $zm1$ is the reference point.

waveguide to IDG transition are considered.

Figure 6.15 shows the circuit layout for this measurement.

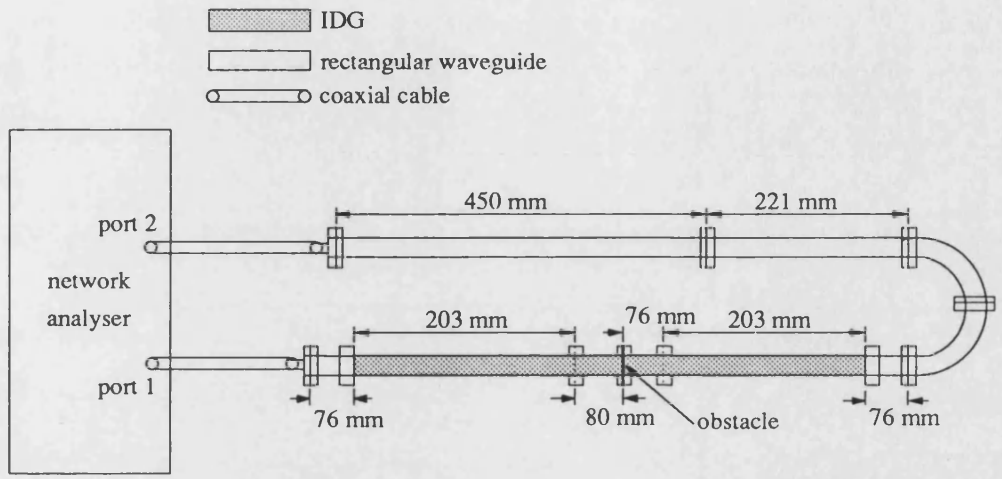

Figure 6.15: Circuit arrangement for measuring R.C. and T.C of the IDG with the metal obstacle normal to the guide.

Figure 6.16, 6.17, and 6.18 show R.C. of the guide with the obstacle. In the computation the heights of the obstacle (hd) are varied. The monitor point in the transverse plane is $M1(8.128\ mm,\ 25.4\ mm)$ and in the z direction is $zm1$=182.88 mm. The position of the obstacle is at zd=304.8 mm. These figures compare computed results with measurements ($S11$, $S22$). The physical heights of the obstacle in the measurements for Fig. 6.16 is 5.080 mm, for Fig. 6.17 is 10.16 mm, and for Fig. 6.18 is 15.24 mm. $S22$ has more residual variation for higher frequencies because the path to port 2 is longer than the path to port 1 (Fig. 6.15). These figures show that there is a good agreement between theory and measurement for the centre and the lower band of the frequency. For the higher band of frequency the difference between theory and measurement grows up because consistency of the calculated R.C. becomes poor with increasing

frequency in this range. In the results of measurements for the first frequency, there is a vertical jump which is because of the input data error from the network analyser to computer.

There is also a tiny difference between theory and measurement. This is because exact physical adjustment of the height of the obstacle is not possible and this is the reason that for a particular physical height, three theoretical heights are considered.

Figure 6.19, 6.20, and 6.21 show T.C. of the line in the presence of the obstacle. In the computation the heights of the obstacle (hd) are varied. The monitor point in the transverse plane is $M1$(8.128 mm, 25.4 mm) and in the z direction is $zm4$=447.04 mm. The position of the obstacle is at zd=304.8 mm. These figures compare computed results with measurements ($S12$). The physical heights of the obstacle in the measurements for Fig. 6.19 is 5.080 mm, for Fig. 6.20 is 10.16 mm, and for Fig. 6.21 is 15.24 mm. The explanation about agreement and difference between theory and measurement is the same as described above for the R.C.

The weakness of the consistency by increasing frequency in the higher band of frequency is also observed for different monitor points in the transverse plane. Figures 6.22 and 6.23 show this weakness for R.C. and T.C. when monitor point is changed in the transverse plane ($M1$, $M2$, and $M3$) while monitor point in the z direction for R.C. is $zm1$ = 182.88 mm and for T.C. is $zm4$=447.04 mm. In these figures theoretical and physical height of the obstacle (hd) is 5.080 mm.

In this chapter, fundamental stage in the analysis of the IDG discontinuities which is the metal obstacle normal to the guide is considered by the FDTD method. The dominant mode of the guide (HE_{01}) is approximated by the TE_{odd} mode of the dielectric slab waveguide. By applying the inverse Fourier transform the necessary field components for the excitation as a function of distance for the FDTD analysis

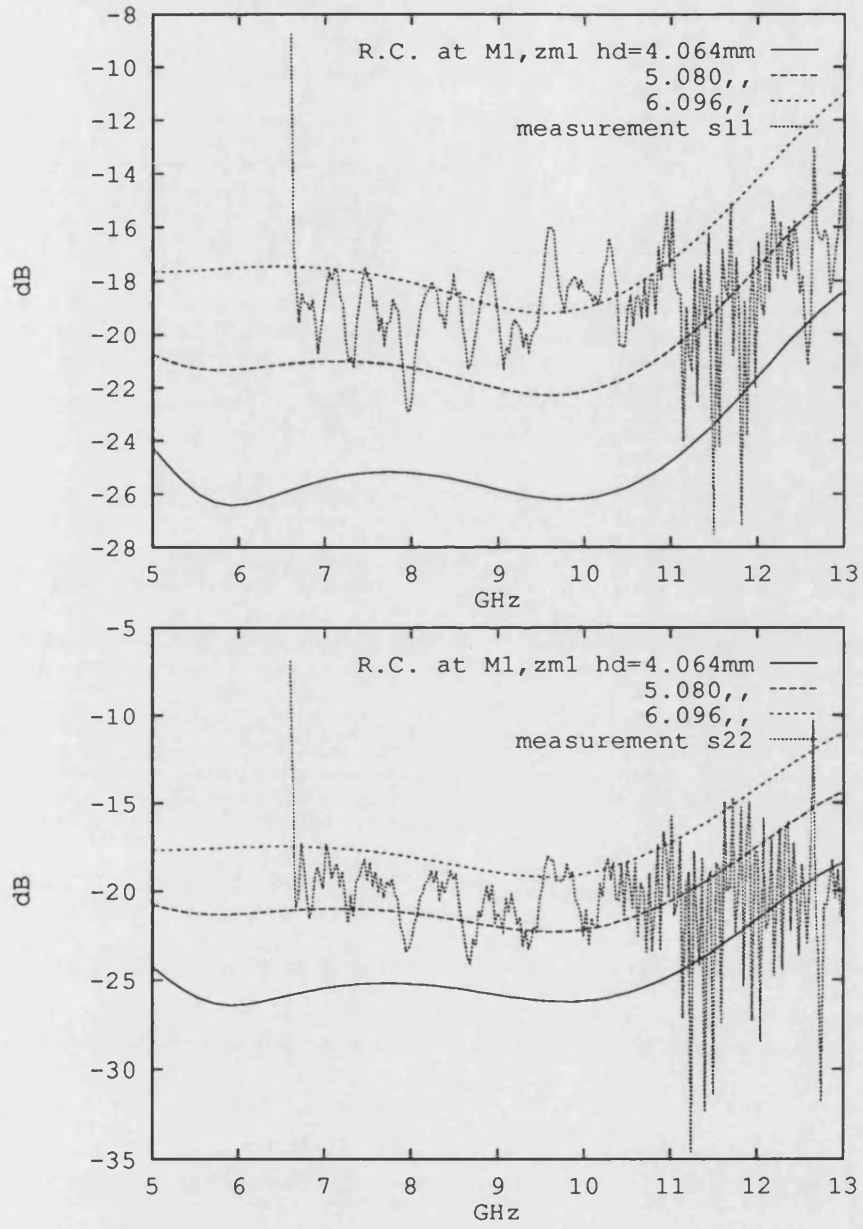

Figure 6.16: Reflection Coefficients (R.C.) of the line due to the obstacle with different computation heights (hd) where the monitor point is $M1(8.128\ mm, 25.4\ mm)$ and $zm1$=182.88 mm. Position of the obstacle is zd=304.8 mm. Physical height of the obstacle in the measurement is 5.080 mm.

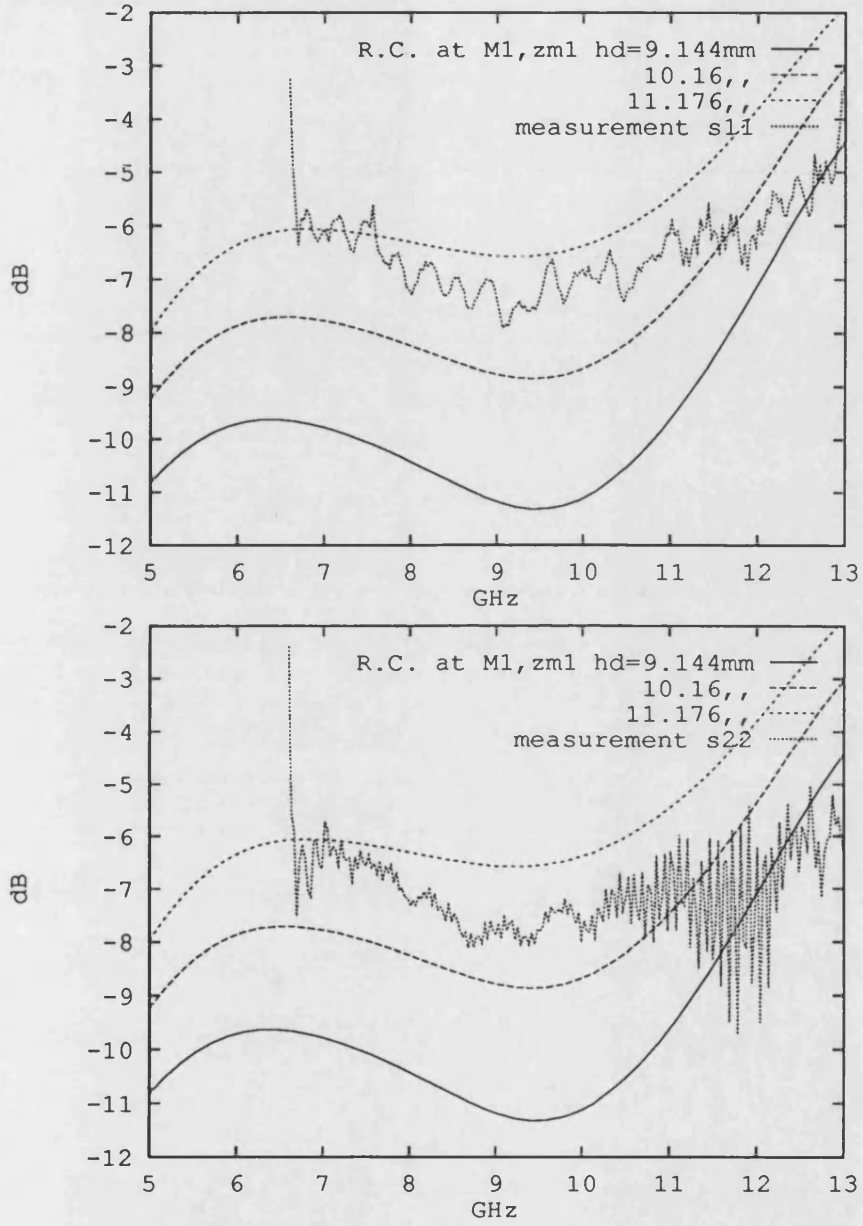

Figure 6.17: Reflection Coefficients (R.C.) of the line due to the obstacle with different computation heights (hd) where the monitor point is $M1(8.128\ mm, 25.4\ mm)$ and $zm1$=182.88 mm. Position of the obstacle is zd=304.8 mm. Physical height of the obstacle in the measurement is 10.16 mm.

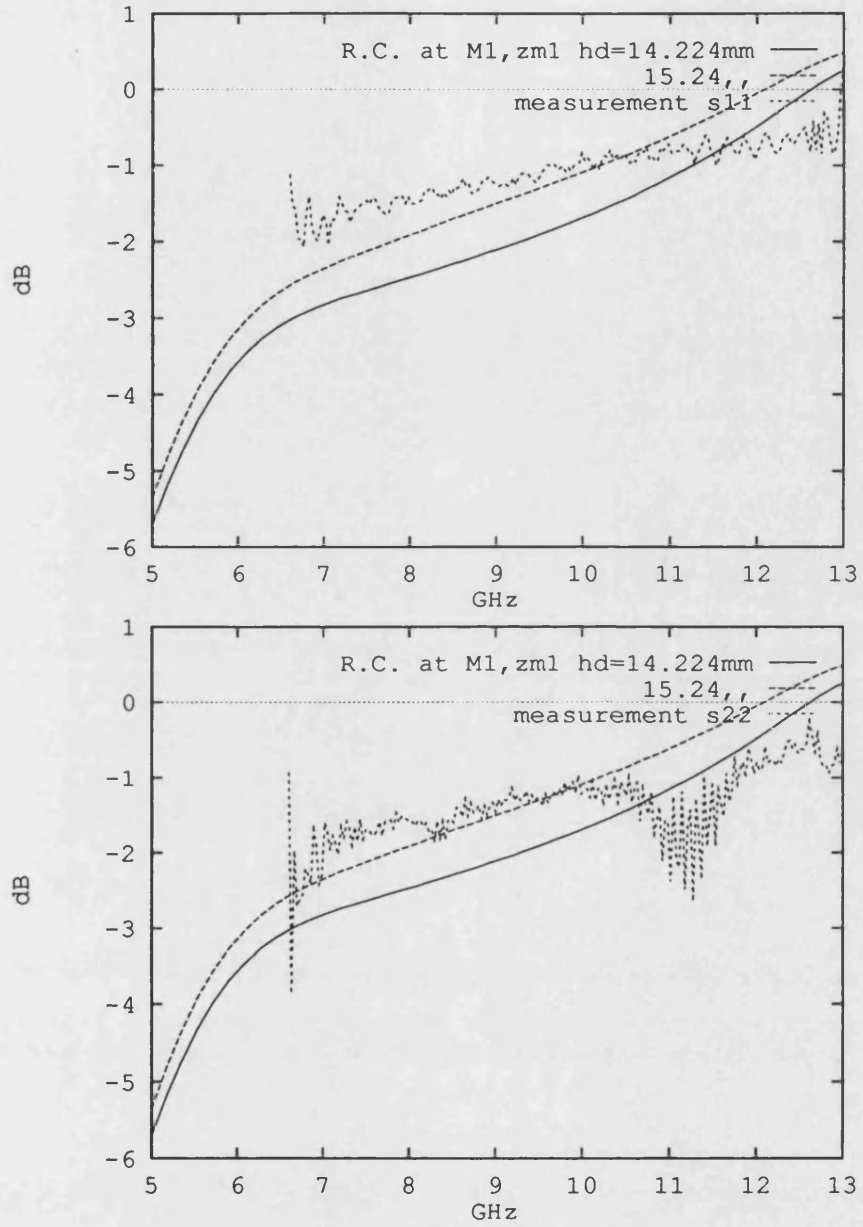

Figure 6.18: Reflection Coefficients (R.C.) of the line due to the obstacle with different computation heights (hd) where the monitor point is $M1(8.128\ mm, 25.4\ mm)$ and $zm1$=182.88 mm. Position of the obstacle is zd=304.8 mm. Physical height of the obstacle in the measurement is 15.24 mm.

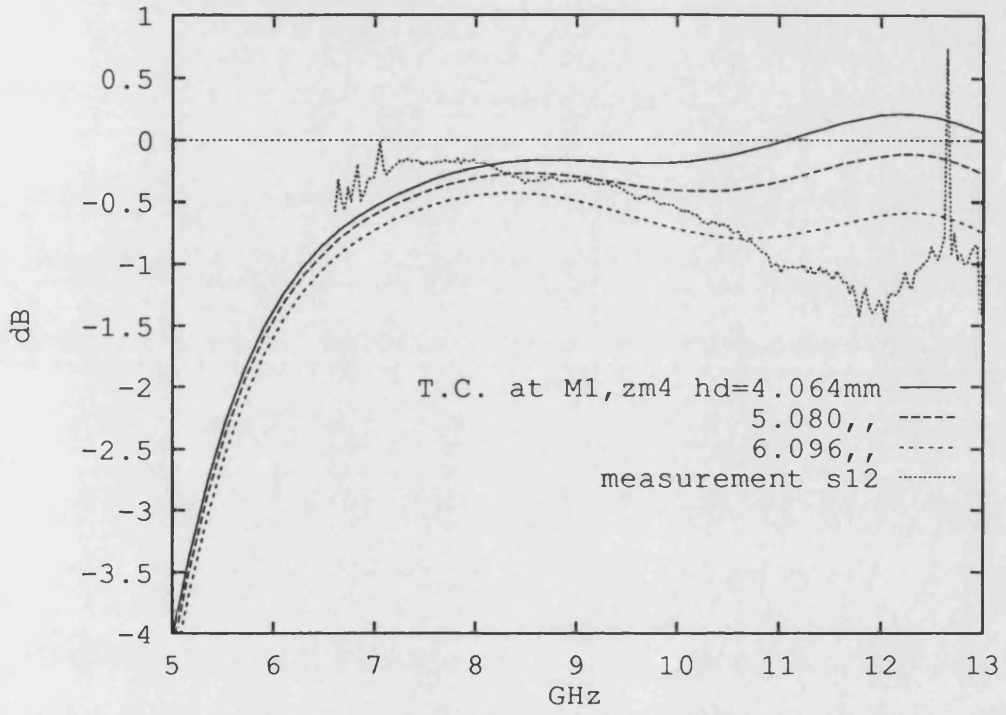

Figure 6.19: Transmission Coefficients (T.C.) of the line due to the obstacle with different computation heights (hd) where the monitor point is $M1$(8.128 mm, 25.4 mm) and $zm4$=447.04 mm. Position of the obstacle is zd=304.8 mm. Physical height of the obstacle in the measurement is 5.08 mm (as measured by a vernier).

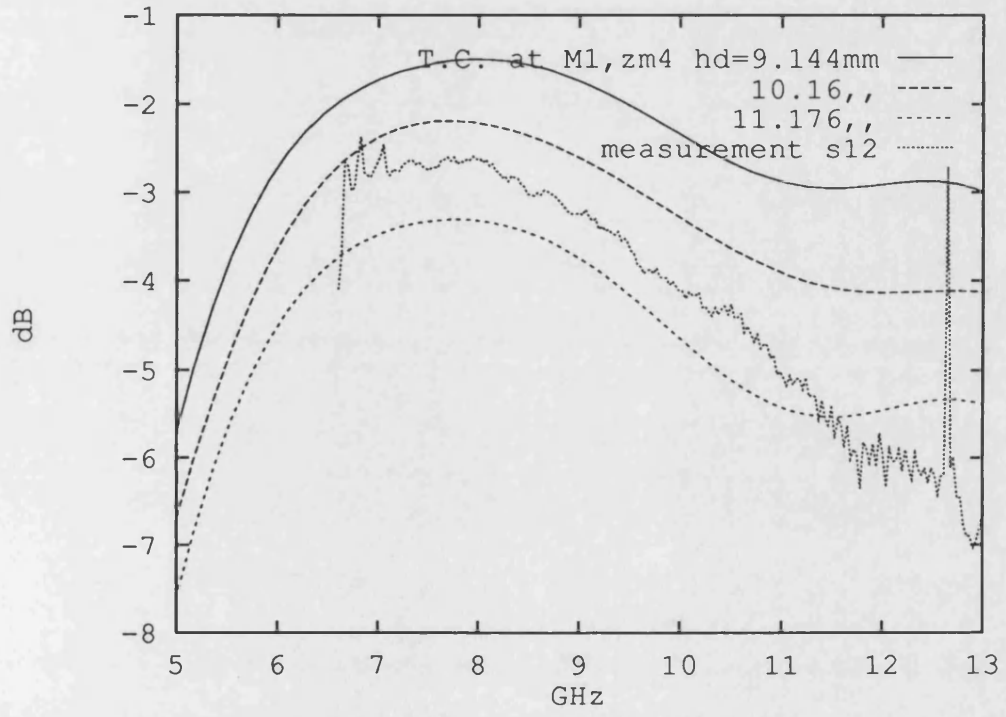

Figure 6.20: Transmission Coefficients (T.C.) of the line due to the obstacle with different computation heights (hd) where the monitor point is $M1$(8.128 mm, 25.4 mm) and $zm4$=447.04 mm. Position of the obstacle is zd=304.8 mm. Physical height of the obstacle in the measurement is 10.16 mm.

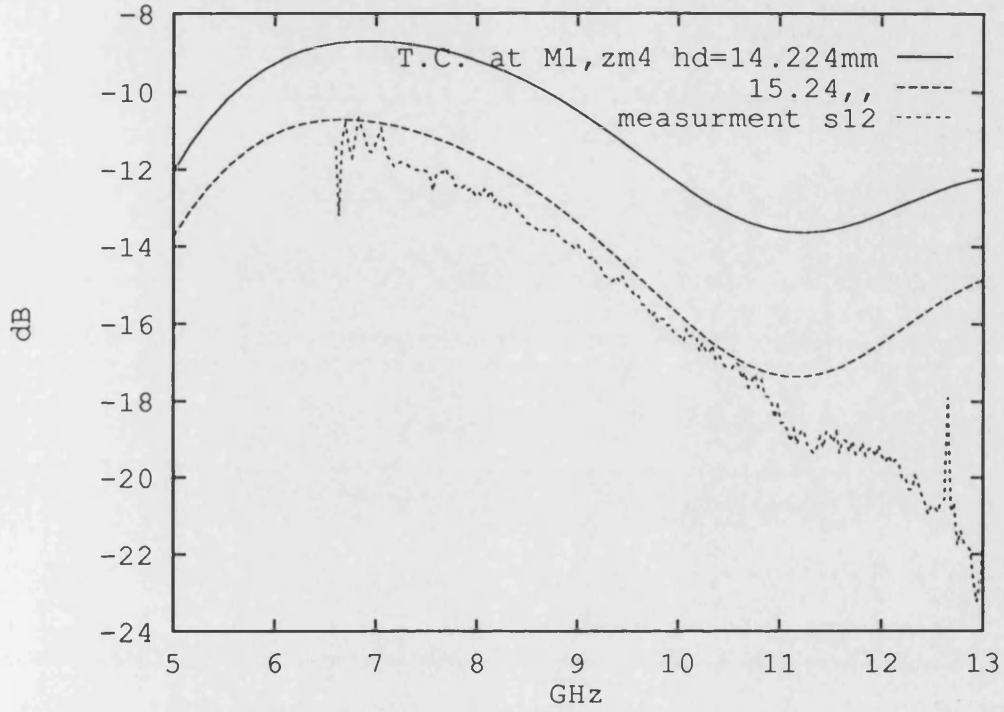

Figure 6.21: Transmission Coefficients (T.C.) of the line due to the obstacle with different computation heights (hd) where the monitor point is $M1$(8.128 mm, 25.4 mm) and $zm4$=447.04 mm. Position of the obstacle is zd=304.8 mm. Physical height of the obstacle in the measurement is 15.24 mm.

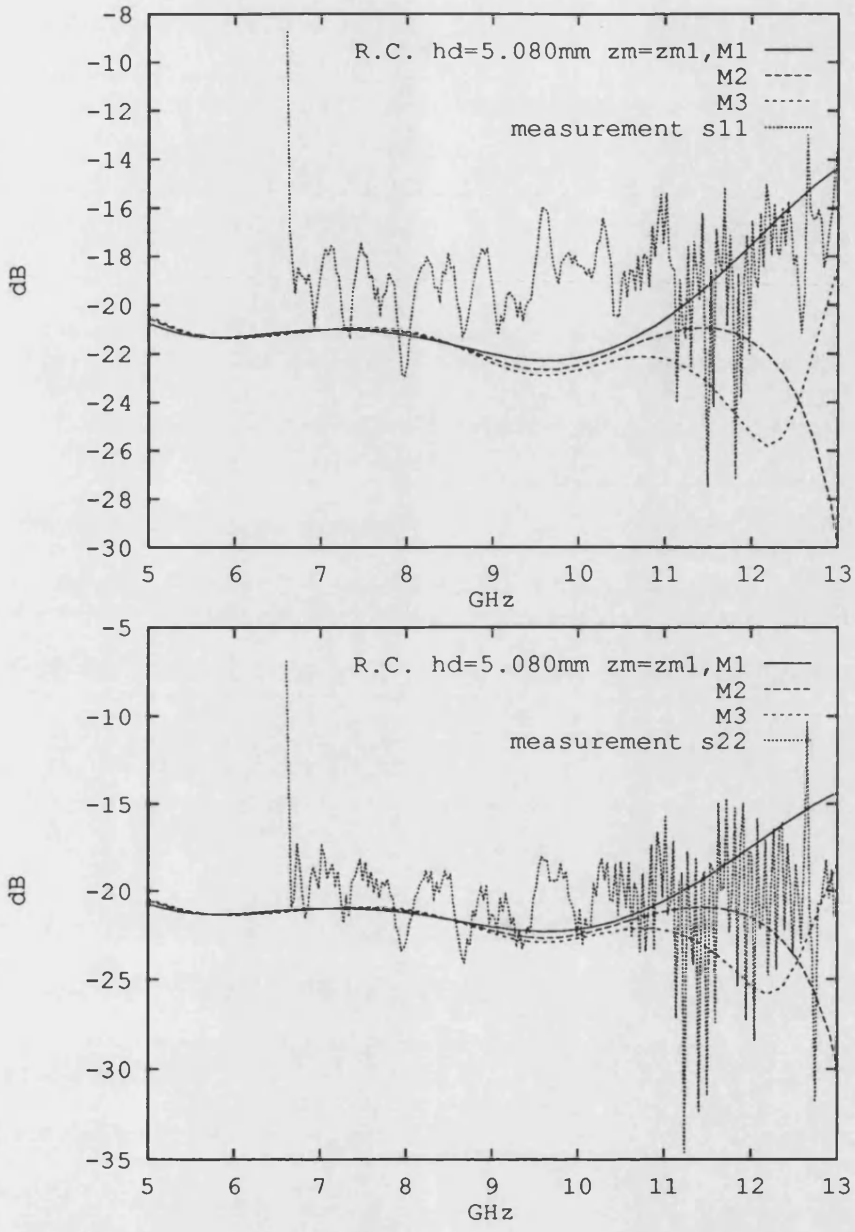

Figure 6.22: Reflection Coefficients (R.C.) of the line due to the obstacle with theoretical and physical heights hd=5.080 mm where the monitor points in the transverse plane are different, $M1$(8.128 mm, 25.4 mm), $M2$(14.224 mm, 25.4 mm), and $M3$(18.228 mm, 25.4 mm). In the z direction the three monitor points are the same ($zm1$=182.88 mm). Position of the obstacle is zd=304.8 mm.

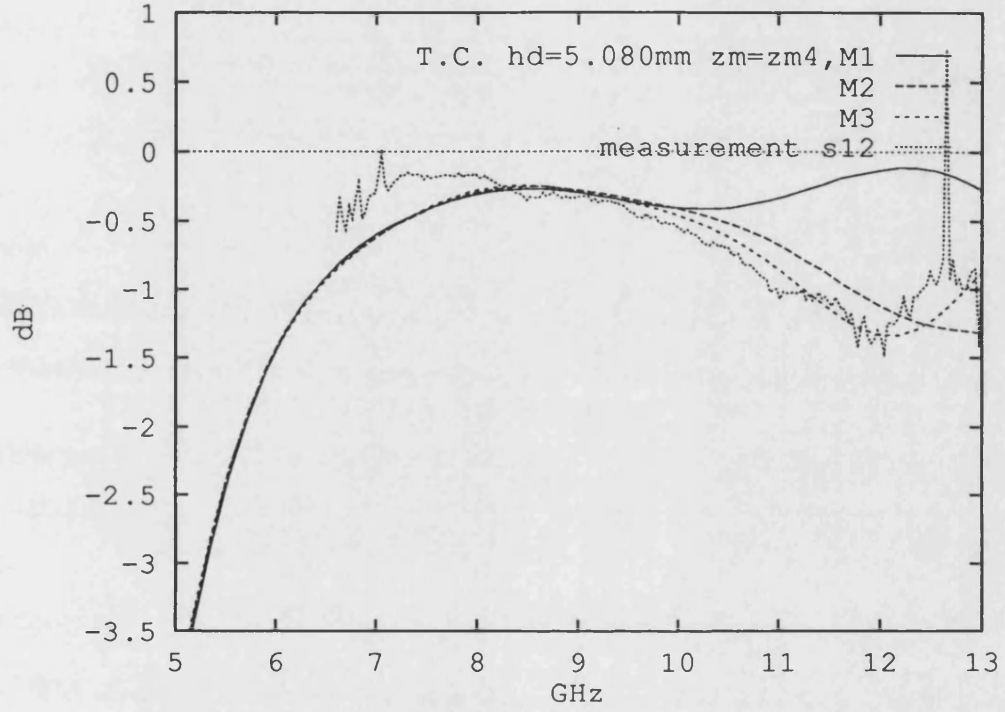

Figure 6.23: Transmission Coefficients (R.C.) of the line due to the obstacle with theoretical and physical heights hd=5.080 mm where the monitor points in the transverse plane are different, $M1$(8.128 mm, 25.4 mm), $M2$(14.224 mm, 25.4 mm), and $M3$(18.228 mm, 25.4 mm). In the z direction the three monitor points are the same ($zm4$=447.04 mm). Position of the obstacle is zd=304.8 mm.

are obtained. To limit the volume of the computation, 1st order Mur's ABC is used. Reflection and Transmission coefficients (R.C. and T.C.) of the guide due to the presence of the obstacle are calculated for different height of the obstacle and different monitor points. These results show that when the height of the obstacle is increased, the R.C. increases, T.C. decreases, but P_{loss} increases up to about two third of the maximum height of the obstacle and after that it will decrease. The results also show that for a particular height of the obstacle, when monitor point is changed in the z direction or in the transverse plane, for lower band and centre frequency there is a good consistency between calculated results. By increasing the frequency, this consistency becomes weak. This inconsistency may be due to the scattering of the wave because of the presence of the metal obstacle. The above result tends to imply that the inclusion of edge effects is desirable in this case.

Also there is a good agreement between calculated results (R.C. and T.C.) and measurement for lower band and centre frequency. A tiny difference between them is because the exact physical adjustment of the obstacle height in guide is impossible. When the frequency is increased, this agreement becomes weak because of the poor reliability of the calculated results in the upper range of frequency.

Chapter 7

Conclusion

7.1 Outline

In this chapter the important points of the six previous chapters are concluded and suggestions for the future work are offered.

7.2 Conclusion of the Work Presented in This Thesis

It is concluded the IDG has a promising future as a transmission line because it overcomes disadvantages of some surface guides like image line and has some advantages that include simpler manufacturing, low radiation from discontinuities and ease of connection to active devices.

A discontinuity which is an abrupt change in geometry of the line causes reflection and changes the characteristics of the line. It usually occurs in practical circuits, because they are contained in additional parts like impedance stubs,

transformers, coupling to resonators and active devices, etc. Up to now, analysis of discontinuities has been pertaining to the conventional guides like microstrip and strip line and nobody has considered the IDG circuit discontinuities. This is the important reason that the author was determined to do this task.

In the present investigation the FDTD method is selected from many methods. Mainly, the advantages of this method are: a full-wave analysis, simple preprocessing, generality and ability to model many other structures.

In using the FDTD method, determination of cell and time step size must satisfy the Courant stability condition. To make the numerical computation domain finite, an Absorbing Boundary Condition (ABC) is needed to simulate the unbounded physical space. Among some ABCs 1st order Mur's ABC as the conventional one and Perfectly Matched Layer (PML) ABC as the newest and potentially perfect one have been investigated.

When the FDTD method is implemented in rectangular waveguide for its dominant mode (TE_{01}), for the purpose of testing the code and investigating the method of excitation, these ABCs are used at both ends of the guide. It is concluded that the 1st order Mur's ABC is the simplest one for implementation, the lowest requirement for computer time and memory, and is sufficient for narrow frequency bandwidth. It is also concluded that the PML ABC has a bigger frequency bandwidth of absorption than the 1st order Mur's ABC but its implementation is complicated and in competition with 1st order Mur's ABC, it needs much more computer memory and time (for the present analysis of IDG discontinuity, if the PML ABC is used instead of 1st order Mur's, computer memory increases more than 400 percent). Therefore 1st order Mur's ABC was selected for the analysis of IDG discontinuities.

For excitation, in the implementation of the FDTD method in the rectangular waveguide, three main field components of the TE_{01} are produced as a function of

distance by the inverse Fourier transform to initiate the line for the first time step of the analysis. It is concluded that to have a desirable frequency bandwidth , the input frequency bandwidth of the inverse Fourier transform must be increased by the factor $c_f = \frac{v_p}{v_g}$. This method of excitation is satisfactorily used in investigation of IDG discontinuities when the TE_{odd} mode of the dielectric slab waveguide is applied in the approximation of the dominant mode (HE_{01}).

In the investigation of the IDG discontinuities, a discontinuity caused by a metal obstacle located normal to the z direction is investigated. This is the fundamental case of other discontinuities in the IDG. By tiny changes in the present analysis which are mentioned in the next section, other discontinuities of this guide can be analysed.

In the IDG, the fundamental mode is successfully approximated by the TE_{odd} mode of the dielectric slab waveguide. Valuable experience of excitation of the TE_{10} mode in the rectangular waveguide gives the great lead to the excitation of the IDG guide. In the analysis, the height of the obstacle and the monitor point for calculation of reflection and transmission coefficients are changed. It is concluded that when the height of the obstacle increases, the reflection coefficient increases and transmission coefficient decreases with respect to frequency. In this increasement of the height of the obstacle, power loss (P_{loss}) increases up to about two third of the maximum height and after that it will decreases. The length of the guide must be enough long so that separation of the incident and reflection pulses in time is possible.

It is concluded that for centre and lower band of frequency there is consistency for the R.C. the and T.C. for any height of obstacle and any monitor point. There is a good agreement between measurements and calculations for this range of frequency. By increasing frequency towards the upper band, the consistency and the agreement becomes weak. This phenomena is because of the scattering of the waves due to presence of the obstacle which is the sharpest appearance

of a metal foil in the transmission of the wave. Other IDG discontinuities may have not (like step in dielectric) or have less this phenomena (like step in metal height).

7.3 Suggestions for Future Work

As mentioned above, the discontinuity caused by the metal obstacle is the fundamental case and leads to other IDG discontinuities. It contains all points such as excitation based on approximation of dominant mode, using ABC, implementation of boundary conditions. Other discontinuities that can be investigated are:

Step in Height, Figure 7.1a shows this discontinuity that is caused by decreasing the dimension b (Fig 7.1) of the IDG which occurs in changing from a deep to a shallow slot or first step in IDG discontinuities caused by impedance transformer (Fig.7.1b).

Repetitive Double Steps in Height, which occurs in IDG filters (Fig. 7.1c). Implementation of these kinds are similar to metal obstacle investigation. At the boundary of the metal and dielectric (eg. AB and BC), tangential electric field and normal magnetic fields are zero and inside the metal regions the FDTD formulations do not need to be calculated.

Step in Dielectric, Figure 7.1d shows this kind of IDG discontinuity which may occur parallel to step in height or may be used in an impedance transformer by repetitive steps in dielectric. In the implementation of this kind of discontinuity, for any electric field that is located at the boundary of the air and dielectric (regarding Yee's mesh, Fig. 3.1), eg. EF and FG, the factor α_E in Equation 3.14-3.16 must be calculated by an average of the permittivities of air and dielectric.

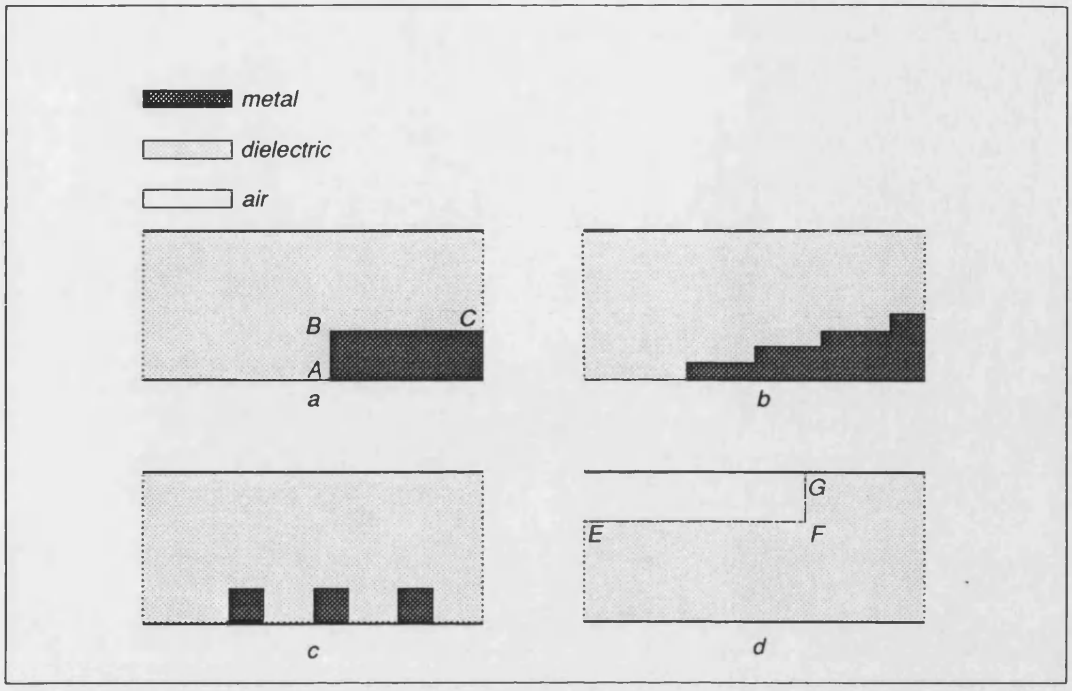

Figure 7.1: Some IDG discontinuities a)step in height b)discontinuities caused by impedance transformer c) repetitive double steps in height d)step in dielectric.

IDG Bend, Figure 7.2 shows this kind of discontinuity which occurs in the circuit layout. The important point in a simulation of this structure is that the second vertical ABC is located in the second arm of the bend far enough from the bend not to absorb the main fields.

IDG Step in Width, this discontinuity occurs in a double step in width which is used in stubs, T junction, branch line coupler etc. Figure 7.3 shows this kind of discontinuity in the IDG. For implementation, it requires two ABCs at each end and upper side of the guide.

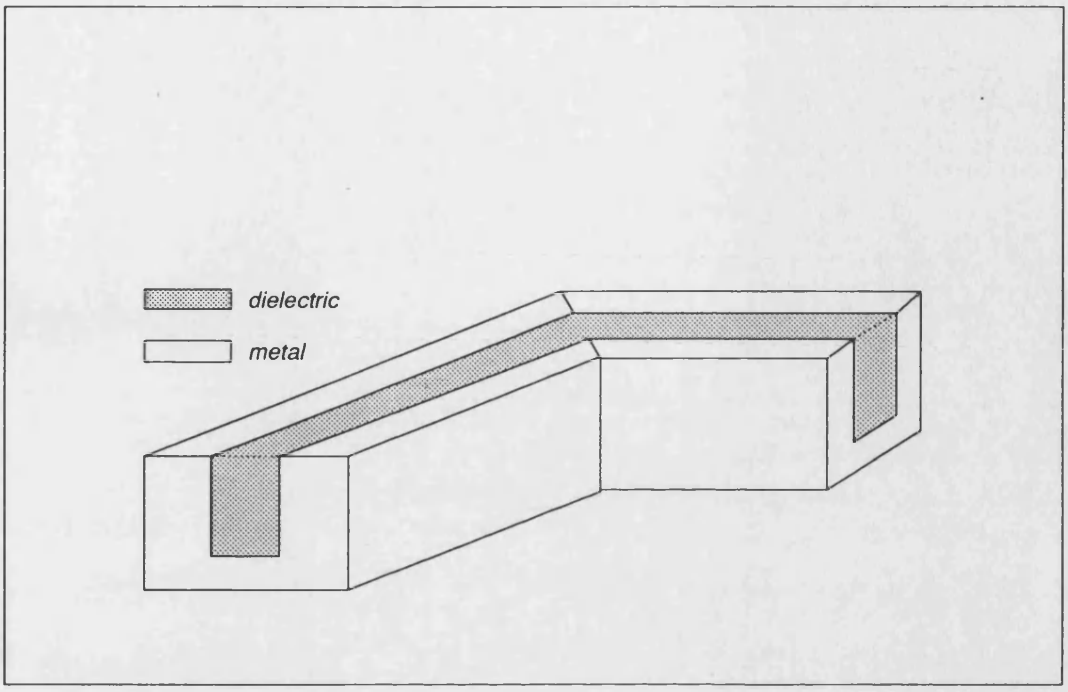

Figure 7.2: IDG bend discontinuity

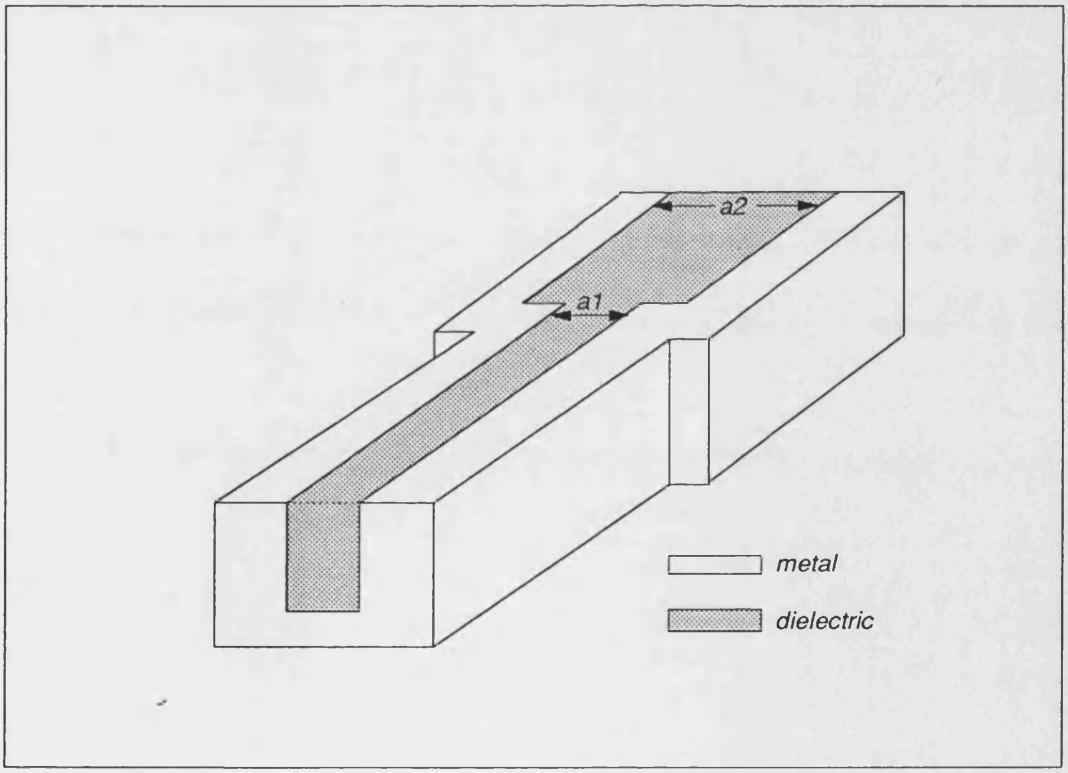

Figure 7.3: IDG step in width discontinuity

References

[1] Collin R.E., "Foundation For Microwave Engineering", Second Edition, McGraw-Hill International Editions, 1992.

[2] Baden-Fuller A.J., "Microwaves, An Introduction to Microwave Theory and Technique", Second Edition, Oxford, Pergaman, 1990.

[3] Edwards T., "Foundations for Microstrip Circuit Design", Second Edition, John Wiley & Sons, 1992.

[4] Itoh T. and Adelseck B., "Trapped Image Guide for Millimeter-Wave circits." *IEEE Trans. Microwave Theory Tech.*, vol. 28, no. 12, pp. 1433-1436, Dec. 1980.

[5] Itoh T., "Inverted Strip Dielectric Waveguide for Millimeter Wave Integrated Circuits." *IEEE Trans. Microwave Theory Tech.*, vol. 24, no. 11, pp. 821-827, Nov. 1976.

[6] Rozzi T. and Ma L., "Scattering by Dipoles in Inset Dielectric Guide and Application to Millimetric Leaky Wave Antennas, " *17th European Microwave Conference Proc.*, pp. 543-548, 1987.

[7] Hedges S. J., PhD Thesis, University of Bath, 1987.

[8] Ma L., PhD Thesis, University of Bath, 1989.

[9] Sewell P.D., PhD Thesis, University of Bath, 1991.

[10] Sewell P. D. and Rozzi T., "The Continuous Spectrum of the Inset Dielectric Guide and Its Application to Waveguide Transitions," *IEEE Trans. Microwave Theory Tech.*, vol. 41, no.2, pp. 282-289, Feb. 1993.

[11] Boscovic D., PhD Thesis, University of Bath, 1991.

[12] Gupta K.C., Garg R., and Bahl I.J., "Microstrip Lines and Slotlines", Artech House, Inc., 1979.

[13] Oliner A.A., "Equivalent Circuits for Discontinuities in Balanced Strip Transmission Line," *IEEE Trans. Microwave Theory Tech.*, vol. MTT-3(3), pp. 134-143, 1995.

[14] Spillard C., Pennock S.R., Shepherd P.R., and Burchett, "An Improved Equivalent Circuit Representation of Stripline Step in Width Discontinuities," *24th European Microwave Conference*, Cannes, pp. 1938-1942, 5-8th Sept, 1994.

[15] Getsinger W.J., " A Solution of The 3-Conductor Mapping Problem With Application to Planar Lines and Couplers," *17th European Microwave Conference*, pp. 1009-1014, 7-11 Sept. 1987.

[16] Cohn S.B., "Characteristic Impedance of Broadside-coupled Strip Transmission Lines," *IEEE Trans. Microwave Theory Tech.*, pp. 633-637, Nov. 1960.

[17] Chen T.S., "Determination of the Capacitance, Inductance, and Characteristic Impedance of Rectangular Lines," *IEEE Trans. Microwave Theory Tech.*, pp. 510-520, Sept. 1960.

[18] Itoh T., editor, "Numerical Techniques for Microwave and Millimeter-wave Passive Structures", John Wiley & Sons, 1989.

[19] Schneider M.V., "Computation of Impedance and Attenuation of TEM-lines by Finite Difference Methods," *IEEE Trans. Microwave Theory Tech.*, vol. MTT-13, no. 6, pp. 793-800 Nov. 1965.

[20] Yee K.S., "Numerical Solution of Initial Boundary-value Problems Involving Maxweel's Equations In Isotropic Media," *IEEE trans. Antenna Propagation.*, vol. AP-14, pp. 302-307, May 1996.

[21] Taflove A. and Umashankar K.R., "Solution of Complex Electromagnetic Penetration and Scattering Problems in Unbounded Regions," in Kalinowski A.J. (ed.) Computational Methods for Infinite Domain Media-structure Interaction. Washington, DC: ASME, vol. 46, pp. 83-113, 1981.

[22] Taflove A., "Application of the Finite Difference Time Domain Method to Sinusoidal Steady State Electromagnetic Penetration Problems," *IEEE Trans. Electromagnetic Compatibility,* vol. EMC-22, no. 3, pp. 191-202, Aug. 1980.

[23] Taflove A. and Brodwin M.E., "Computation of the Electromagnetic Field and Induced Temperature Within a Model of the Microwave-irradiated Human Eye," *IEEE Trans. Microwave Theory Tech.*, vol. MTT-23, no. 11, pp. 888-896, Nov.1975.

[24] Taflove A. and Brodwin M.E., "Numerical Solution of Steady Electromagnetic Scattering Problems Using Time-dependent Maxwell's Equations," *IEEE Trans. Microwave Theory Tech.*, vol. MTT-23, no. 8, pp. 623-630, Aug. 1975.

[25] Taflove A. and Umashankar K.R., "A Hybrid Moment Method / Finite Difference Time Domain Approach to Electromagnetic Coupling and Aperture Penetration into Complex Geometries," *IEEE Trans. Antenna Propagation*, vol. AP-30, no. 4, pp. 617-627, July 1982.

[26] Umashankar K.R. and Taflove A., "A Novel Method to Analyze Electromagnetic Scattering of Complex Objects", *IEEE Trans. Electromagnetic Compatibility*, vol. EMC-24, no. 4, pp. 397-405, Nov. 1982.

[27] Taflove A. and Umashankar K.R.," The Finite Difference Time Method for Numerical Modeling of Electromagnetic wave Interactions", *Electromagnetics*, vol. 10, pp. 105-126, 1990.

[28] Taflove A. and Umashankar K.R., "Radar Cross Section of General Three Dimensional Scatterers," *IEEE Trans. Electromagnetic Compatibility*, vol. EMC-25, pp. 433-440, Nov. 1983.

[29] Choi D.H. and Hoefer W.J.R., "The Finite Difference Time Domain Method and its Application to Eigen Value Problems," *IEEE Trans. Microwave Theory Tech.*, vol. MTT-34, no. 12, pp. 1464-1469, Dec. 1986.

[30] Zhang X., Fang J., Mei K.K., and Liu Y., "Calculation of The Dispersive Characteristics of Microstrips by the Time Domain Finite Difference Method," *IEEE Trans. Microwave Theory Tech.*, vol. 36, no. 2 pp. 263-267, Feb. 1988.

[31] Sheen D.M., Ali S.M., Abouzahra M.D., and Kong J.A., "Application of the Three Dimensional Finite Difference Time Domain Method to the Analysis of Planar Microstrip Circuits," *IEEE Trans. Microwave Theory Tech.*, vol. 38, vo. 7, pp. 849-857, July 1990.

[32] Sadiku Matthew. N.O., "Numerical Techniques in Electromagnetism", CRC Press, 1992.

[33] Mur G., "Absorbing Boundary Conditions For The Finite Difference Approximation of the Time Domain Electromagnetic Field Equations," *IEEE Trans. Electromagnetic Compatibility*, vol. EMC-23, pp. 377-382, Nov. 1981.

[34] Chia T.T., Burkholder R.J., and Lee R., "The Application of FDTD in Hybrid Methods For Cavity Scattering Analysis," *IÉEE Trans. Antennas Propagation*, vol. 43, no. 10, pp. 1082-1090, Oct. 1995.

[35] Demarest K., Plumb R., and Huang Z., "FDTD Modeling of Scatterer in Stratifield Media," *IEEE Trans. Antennas Propagation*, vol. 43, no 10, pp.1164-1168, Oct. 1995.

[36] Tran A.M., Houshmand B., and Itoh T., "Analysis of Electromagnetic Coupling Through a Thick Aperture in Multilayer planar Circuit Using the Expended Spectral Domain Approach and Finite Difference Time Domain Method," *IEEE Trans. Antennas Propagation*, vol. 43, no. 9, pp. 921-926, Sept.1995.

[37] Neale B.M. and Gopinath, "Microstrip Discontinuity Inductances," *IEEE Trans. Microwave Theory Tech.*, vol. MTT-26, no. 10, pp. 827-831, Oct.1978.

[38] Alam Md.S., Hirayama K., Hayashi Y., and Koshiba M., "Finite Element Analysis of Propagating, Evanescent, and Complex Modes in Finlines," *IEE Proc. Microwave Antennas Propagation*, vlo. 141, no. 2, pp. 65-69, April 1994.

[39] Booton R.C.,"Computational Method for Electromagnetics and Microwaves" John Wiley & Sons, Inc., 1992.

[40] Farrar A. and Adams A.T., "Computation of Lumped Microstrip Capacities by Matrix Methods Rectangular Sections and End Effect," *IEEE Trans. Microwave Theory Tech.*, pp. 495-497, May 1971.

[41] Farrar A. and Adams A.T., "Characteristic Impedance of microstrip by the Method of Moments," *IEEE Trans. Microwave Theory Tech.*, pp. 65-66, Jan. 1970.

[42] Shih Y.C. and Gray K.G., "Convergency of Numerical Solutions of Step-type Waveguide Discontinuity Problems by Modal Analysis," *IEEE MTT-S Int. Microwave Symposium Digest*, pp. 233-235, May 1983.

[43] Menzel W. and Wolff I., "A Method for Calculating the Frequency- dependent Properties of Microstrip Discontinuities," *IEEE Trans. Microwave Theory Tech.*, vol. MTT-25, no. 2, pp. 107-112, Feb. 1977.

[44] Chu T.S., Itoh T., and Shin Y.C., "Comparative Study of Mode Matching Formulations for Microstrip Discontinuity Problems," *IEEE Tran. Microwave Theory Tech.*, vol. MTT-33, no. 10, pp. 1018-1023, Oct. 1985.

[45] Huang T.W. and Itoh T., " The Influence of Metallization Thickness the Characteristics of Cascaded Junction Discontinuities of Shielded Coplanar Type Transmission Line," *IEEE Trans. Microwave Theory Tech.*, vol. 41, no. 4, pp. 693-697, April 1993.

[46] Sorrentino R. and Itoh T., "Transverse Resonance Analysis of Finline Step Discontinuities," *IEEE Trans. Microwave Theory Tech.*, vol. MTT-32, pp. 1632-1638, 1984.

[47] Sorrentino R., "Transverse Resonance Technique," in Itoh T., Ed., "Numerical Techniques for Microwave and Millimeter-wave Passive structures", Ch. 11, pp. 637-696, New York: J. Wiley, 1989.

[48] Alessandri F., Baini G., Mongiardo M., and Sorrentino R., "A 3-D Mode Matching Technique for the Efficient analysis of Coplanar MMIC Discontinuities with Finite Metallization Thickness," *IEEE Trans. Microwave Theory Tech.*, vol. 41, No. 9, pp. 1625-1629, Sept. 1993.

[49] Burchett M.H., PhD Thesis, University of Bath, p.14, 1994.

[50] Benedek P. and Silvester P., "Equivalent Capacitances for Microstrip Gaps and Steps," *IEEE Trans. Microwave Theory Tech.*, vol. MTT-20, no. 11, pp. 729-733, Nov. 1972.

[51] Silvester P. and Benedek P., "Microstrip Discontinuity Capacitances for Right-angle Bends, T-junctions, and Crossing," *IEEE Trans. Microwave Theory Tech.*, vol. MTT-21, no. 5, pp. 341-346, May 1973.

[52] Eid E.M.A., El-Mikati H.A., and Razzak M.A., "Boundary Element Analysis of Microstrip and Strip Lines," *Proceeding of the 33rd Midwest Symposium on Circuits & systems*, pp. 40-143, Aug. 12-15th 1990, Calgay, Alberta, Canada.

[53] Brebbia C.A., "The Boundary Element Method for Engineers," Pentech Press, London, 1978.

[54] Kagami S. and Fukai I., "Application of Boundary Element Method to Electromagnetic Field Problems," *IEEE Trans. Microwave Theory Tech.*, vol. MTT-32, pp. 455-461, Apr. 1984.

[55] Chu T.S. and Itoh T., 'Generalised Scattering Matrix Method for Analysis of Cascaded Offset Microstrip Step Discontinuities," *IEEE Trans. Microwave Theory Tech.*, vol. MTT-34, No. 2, pp. 280-284, Feb 1986.

[56] Jansen R., "The Spectral Domain Approach for Microwave Integrated Circuits," *IEEE Microwave Theory Tech.*, vol. MTT-33 no. 10 pp. 1043-1056, Oct. 1985.

[57] Simons N.R.S. and Sebak A., "Application of the Transmission Line Matrix Method to the Analysis of Scattering by 3-Dimensional Objects," *IEE Proc. Microwave Antennas Propag.*, vol. 142, no. 4, pp. 319-325 Aug 1995.

[58] Kunz K.S. and Luebbers R.J., "Finite Difference Time Domain Method for Electromagnetics" CRC Press, 1992.

[59] Johns P.B., "On the Relationship Between TLM and Finite Difference Method for Maxwell's Equations," *IEEE Trans. Microwave Theory Tech.*, vol. MTT-35, no. 1 pp. 60-61, Jan. 1987.

[60] Engquist B. and Majda A., "Absorbing Boundary Condition for the Numerical Simulation of Waves," *Math. Comp.*, vol.31, pp. 629-651, July 1977.

[61] Fang J. and Mei K.K, "A Super Absorbing Boundary Algorithm for Solving Electromagnetic Problems by the Time Domain Finite Difference Method," *IEEE AP-S Symp. Dig.*, pp. 427-475.

[62] Bi Z., Wu K., Wu C., and Litva J., "A dispersive Boundary Condition for Microstrip Component Analysis Using the FDTD," *IEEE Trans. Microwave Theory Tech.*, vol. 40, no. 4, 1992.

[63] Berenger J.P., "A Perfectly Matched Layer for the Absorption of Electromagnetic Waves," *Jurnal of Computational Physics 114*, pp. 185-200, 1994.

[64] Katz D.S., Thiele E.T., and Taflove A., "Validation and Extension to Three Dimensions of the Berenger PML Absorbing Boundary Condition for FDTD Meshes," *IEEE Microwave and Guided Wave Letters*, Vol. 4, no. 8, pp. 268-270, Aug. 1994.

[65] Brigham E.O., "The Fast Fourier Transform", Prentice-Hall, Inc. Englewood Cliffs, New Jersey, 1974.

[66] Ramo S. and Whinnery J.R., "Fields and Wave in Modern Radio", Second Edition, John Wiley & Sons, 1964.

[67] Pennock S.R. and Shepherd P.R., "Microwave Engineering with Wireless Applications", MacMillan 1998.